PROBABILISTIC ASSESSMENT OF PUMICE CRUSHABILITY AND LIQUEFACTION STRENGTH USING HIERARCHICAL BAYESIAN APPROACH

イ ワヤン アリヤナ バソカ

https://hdl.handle.net/2324/7329481

出版情報：Kyushu University, 2024, 博士（工学）, 課程博士
バージョン：
権利関係：

PROBABILISTIC ASSESSMENT OF PUMICE CRUSHABILITY AND LIQUEFACTION STRENGTH USING HIERARCHICAL BAYESIAN APPROACH

I WAYAN ARIYANA BASOKA

SEPTEMBER 2024

PROBABILISTIC ASSESSMENT OF PUMICE CRUSHABILITY AND LIQUEFACTION STRENGTH USING HIERARCHICAL BAYESIAN APPROACH

九州大学
KYUSHU UNIVERSITY

A DISSERTATION SUBMITTED
IN PARTIAL FULFILLMENT OF THE REQUIREMENTS
FOR THE DEGREE OF
DOCTOR OF ENGINEERING

BY
I WAYAN ARIYANA BASOKA

TO THE
DEPARTMENT OF CIVIL ENGINEERING
GRADUATE SCHOOL OF ENGINEERING
KYUSHU UNIVERSITY
FUKUOKA, JAPAN
2024

GEO-DISASTER PREVENTION LABORATORY

DEPARTMENT OF CIVIL ENGINEERING

GRADUATE SCHOOL OF ENGINEERING

KYUSHU UNIVERSITY

FUKUOKA, JAPAN

CERTIFICATE

The undersigned hereby certify that they have read and recommended to the Graduate School of Engineering for the acceptance of this dissertation entitled, "**PROBABILISTIC ASSESSMENT OF PUMICE CRUSHABILITY AND LIQUEFACTION STRENGTH USING HIERARCHICAL BAYESIAN APPROACH**" in partial fulfillment of the requirements for the degree of **DOCTOR OF ENGINEERING**.

Date: June 2024

Supervisor:

____

Prof. Kiyonobu KASAMA

Examining Committee:

____

Prof. Yasuhiro MITANI

____

Associate Prof. Takashi SASAOKA

ACKNOWLEDGMENT

First and foremost, I would like to thank God "Ida Sang Hyang Widhi Wasa" for giving me the strength, knowledge, and perseverance to complete this dissertation. Without His blessings, this achievement would not have been possible. I would like to express my deepest gratitude to all those who have contributed to the completion of this dissertation. I would like to thank the JICA-MEXT scholarship in the Innovative Asia program for their financial support and resources that made this study possible.

I am especially grateful to my supervisor, Prof. Kiyonobu KASAMA, whose expertise, guidance, and unwavering support have been invaluable throughout this journey. His insightful feedback and encouragement have been instrumental in shaping this dissertation. I would also like to extend my heartfelt thanks to the members of the examining committee, Prof. Yasuhiro MITANI, Assoc. Prof. Takashi SASAOKA, for their time, valuable feedback, and constructive criticism, which greatly improved the quality of this dissertation.

Special thanks go to Assoc. Prof. Zentaro FURUKAWA, for collaboration and intellectual contributions to improve my research, I am grateful to Mr. Yuichi YAHIRO for assistance with the technical support for my experimental works, and thanks to the Department of Civil Engineering and Graduate School of Engineering staff for their support in all administrative works. My thanks were also addressed to Prof. Ahmad RIFA'I and Prof. Noriyuki YASUFUKU for their kindness in guiding me and for their precious advice during my research.

On a personal note, I am deeply thankful to my family and friends for their constant support, patience, and encouragement. To my wife, Ngurah Utami Wedanti, thank you for being a strong woman and taking care of our daughter while I was away continuing my studies. To my daughter, Ni Putu Gauri Rawindra Putri, thank you for being a good and healthy child while your father was away to complete this study.

Lastly, I would like to acknowledge everyone who contributed to this research in any capacity, even if not mentioned by name. Your support has been crucial to the completion of this dissertation.

Thank you all.

I Wayan Ariyana Basoka, Fukuoka 2024

PUBLICATIONS

1. The Physical and Mechanical Properties of Single Pumice Sand Particle. International Journal of GEOMATE, pp. 73-80, Vol.26 No. 115 (2024): March 2024, DOI: https://doi.org/10.21660/2024.115.g13171

   (2024年3月）

   Author: I Wayan Ariyana Basoka, Kiyonobu Kasama, Zentaro Furukawa, Noriyuki Yasufuku, Ahmad Rifa'i

2. Microscopy and Mechanical Behavior of Pumice Single Particle. Proceedings of 13th International Conference on Geotechnique, Construction Material & Environment (GEOMATE 2023), pp. 120- 126. ISBN 978-4-909106100, Tsu, Mie, Japan, 14-16 November 2023

   (2023年11月）

   Author: I Wayan Ariyana Basoka, Kiyonobu Kasama, Zentaro Furukawa, Noriyuki Yasufuku, Ahmad Rifa'i

3. Bayesian Hierarchical Model on Crushability of Pumice Particle Strength. Proceedings of 5th International Conference on Geotechnics for Suitable Infrastructure Development (GEOTEC HANOI 2023), Hanoi, Vietnam, 14-15 December 2023. DOI: 10.1007/978-981-99-9722-0_127

   (2023年12月）

   Author: I Wayan Ariyana Basoka, Kiyonobu Kasama, Zentaro Furukawa, Ahmad Rifa'i

4. Pumice Sand Behavior on Undrained Cyclic Loading. Proceedings of 7th International Conference on Earthquake Geotechnical Engineering (ICEGE 2024), paper ID: OS-45-01, Osaka, Japan, 7-10 May 2024. DOI: 10.3208/jgssp.v10.OS-45-01

   (2024年5月）

   Author: I Wayan Ariyana Basoka, Kiyonobu Kasama, Zentaro Furukawa, Noriyuki Yasufuku, Ahmad Rifa'i

ABSTRACT

Pumice is one of the pyroclastic rocks that contain fragments produced by volcanic explosions and extruded as discrete particles from volcanic vents. Explosive eruptions produce various pyroclastic deposits. Pumice is a light-colored or pale gray to brown porous volcanic glass foam that often floats on water. Pumice particles are easy to break upon by the impact on their structure since the bubbles captured in pumice are covered with translucent weak glass. In volcanic regions such as Japan and Indonesia, there are pumice deposits in soil layers. The pumice layer is pulverized during an earthquake, triggering landslides or liquefaction. Several landslides in Indonesia, Japan, New Zealand, and America were caused by the existence of a pumice layer that failed during the earthquake.

Furthermore, the general interpretation of the test result of geomaterials including pumice still relies on frequentist or statistical sampling theory derived from "conventional statistics". On the other hand, Bayesian reasoning as opposed to "conventional statistics" is useful for scientific data analysis and evaluating data-driven observations to improve their analytical skills. More informed and accurate evaluation and discussion of the test results can be discussed from the Bayesian approach viewpoint. Geotechnical researchers can make better predictions and evaluations based on data and judgments by understanding the Bayesian approach.

From these backgrounds, this study has several objectives: The first objective is to determine the geological, chemical, and microstructural properties of pumice. The second objective is to investigate the crushability of a single pumice particle depending on the particle size and the one-dimensional consolidation property for evaluating the soil matrix behavior of pumice particle aggregation. The final objective is to assess the susceptibility of pumice to liquefaction by examining its response to different levels of confining pressure and variations in density. Afterward, the hierarchical Bayesian model as a Bayesian approach was introduced to interpret and pumice behavior. In order to accomplish these objectives, this dissertation comprises seven chapters, outlined as follows.

Chapter 1 provides an overview of the context and history of this research. The

volcano distribution and earthquake events map in this chapter shows the importance of examining the geotechnical characteristics of the pumice in this special area. Furthermore, it emphasizes the importance of conducting tests on pumice due to its unique pore characteristics and various failure events. Additionally, there is a brief explanation of the benefits of the Bayesian approach as an alternative approach for engineering purposes. From this discussion, it is evident that there needs to be more studies on pumice in the Kyushu region, and the impact of density and confining pressure has not been extensively investigated. Furthermore, most studies still rely on standard statistical methods.

Chapter 2 offers a brief literature review that discusses basic concepts related to chemical, microstructural, single-particle strength tests, liquefaction, and the Bayesian approach based on previous researchers.

Chapter 3 focuses on an analysis of the geologic, chemical, and microstructure properties of pumice. It explains the geology condition of the sampling area, and chemical composition as observed through X-ray fluorescence (XRF), Energy Dispersive Spectroscopy (EDS), and X-ray diffractometry (XRD) tests. The problematic nature of the pumice is attributed to the presence of pores in the pumice, as observed through Scanning Electron Microscopy (SEM). The results indicate that silica (SiO_2) is the primary mineral component of pumice, and pumice has a porous microstructure, making it prone to easy crushing.

Chapter 4 summarized the single-particle strength of pumice based on the test results of the loading test for an individual pumice particle. It is seen that the single-particle strength of pumice decreases as the diameter of pumice particles increases. Additionally, the Weibull parameters for the distribution of the single-particle strength of pumice are comparatively lower than those of general sand material, indicating that pumice particles are more susceptible to crushing. The hierarchical Bayesian approach has a significant improvement for determining Weibull parameters of probabilistic distribution of single-particle strength of pumice particularly when there is a limited amount of available data.

Chapter 5 examines the consolidation property of the soil matrix consisting of pumice particles using a one-dimensional consolidation test with a constant strain rate. The consolidation yield stress of the pumice matrix was discussed from the viewpoint of pumice particle crushing comparing those of other general geomaterials such as clay and quartz sand. It can be characterized that the pumice has a large void ratio that is equal to that of clay. Moreover, the consolidation yield stress obtained from a one-dimensional consolidation test shows a strong correlation with relative density.

Chapter 6 assesses the static and dynamic shear strength properties of pumice for a given relative density and confining pressure based on the results of the undrained triaxial compression test and cyclic triaxial compression test. It can be characterized that there is a strong dependency of confining pressure on the liquefaction strength of pumice. Namely, the liquefaction strength of pumice decreases with increasing confining pressure indicating that the in-site liquefaction strength should be evaluated using the in-site confining pressure. Moreover, a hierarchical Bayesian model can successfully analyze the liquefaction strength of pumice depending on confining pressure and relative even when there is limited data of test results.

Chapter 7 provides a summary, conclusion, main findings of this study, and recommendations for future studies.

TABLE OF CONTENT

LIST OF FIGURES

LIST OF TABLES

CHAPTER I
INTRODUCTION

1.1 Background of Study

Based on data from the Global Volcanism Program (2023), the five countries with the most significant number of volcanoes are the United States with 165 volcanoes, Japan with 122 volcanoes, Russia with 117 volcanoes, Indonesia with 117 volcanoes, and Chile with 91 volcanoes. Table 1.1 compares the number of volcanoes and the area of the country for these five countries having volcanoes.

Table 1.1 Ratio volcanoes/area for each country

No	**Country**	**Volcanoes**	**Area (km^2)**	**Volcanoes : area (volcanoes/ km^2)**
1	Japan	122	377,975	$1 : 3.098 \times 10^3$
2	Chile	91	756,096	$1 : 8.308 \times 10^3$
3	Indonesia	117	1,904,569	$1 : 16.278 \times 10^3$
4	United States	165	9,833,520	$1 : 59.597 \times 10^3$
5	Russia	117	17,098,246	$1 : 146.138 \times 10^3$

Table 1.1 shows that Japan has the most significant volcanoes/area ratio compared to other countries. It is very common that several tectonic and volcanic earthquakes occur on the border between tectonic plates, as in the Global Volcanism Program (2023). From these conditions, it can be seen that the earthquake risk is very high in Japan. The relatively high volcanic activity in Japan causes a wide distribution of volcanic soil due to the volcanic eruption. One of the volcanic soils that often causes geotechnical problems such as earthquake-induced slope failure and landslides is pumice. Pumice is one of the pyroclastic rocks that contain fragments produced by explosions and extruded as discrete particles from volcanic vents. Explosive eruptions produce various pyroclastic deposits (McPhie et al., 1993) and (Fisher, 1961). Pumice is a light-colored or pale gray to brown

porous volcanic glass foam that often floats on water. The walls of the bubbles in pumice are made of translucent glass; pumice fragments may break upon impact due to their structure (Fisher & Schmincke, 1984).

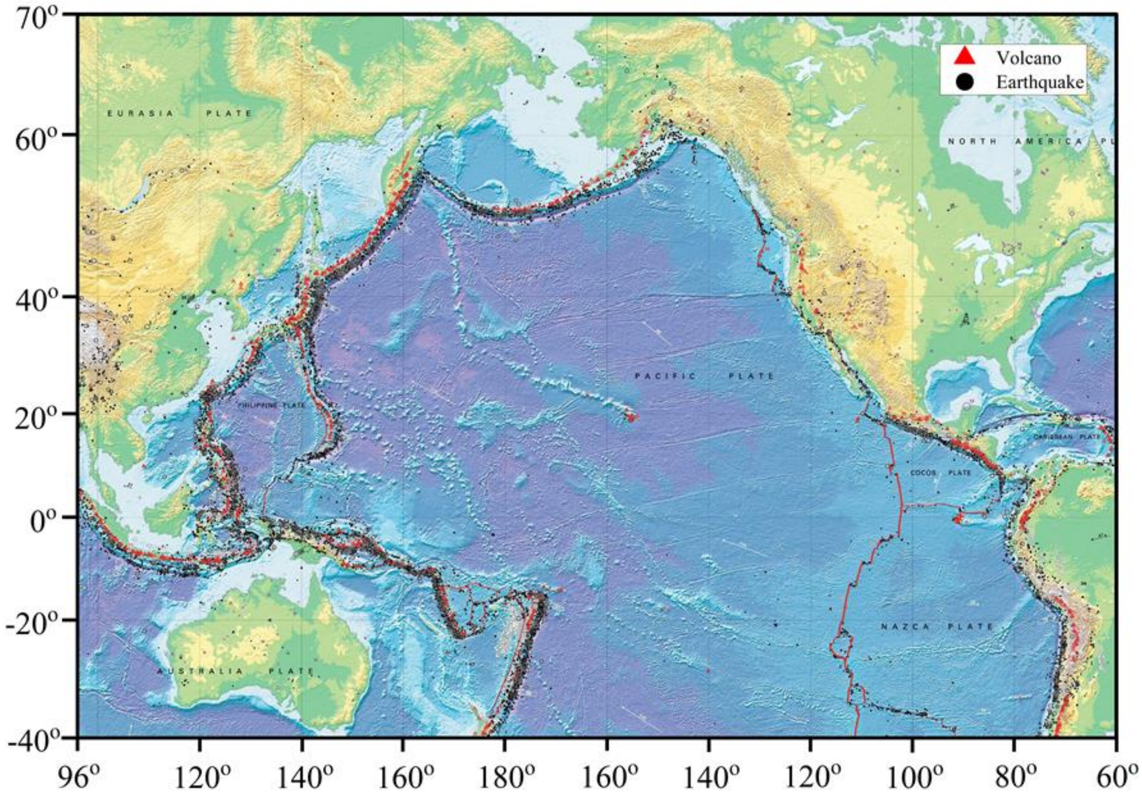

Figure 1.1 Distribution of volcanoes and earthquake events in the Ring of Fire area (modified from Simkin et al. (2006))

In volcanic regions such as Japan and Indonesia, the pumice deposit is easy to find. Pumice (crushable material) is pulverized during an earthquake, triggering landslides or liquefaction. Several landslides in some areas of Indonesia, Japan, New Zealand, and America were caused by the pumice layer that failed during the earthquake (Chiaro et al., 2022; Crosta et al., 2005; Faris & Fawu, 2014; Hosobuchi et al., 2021; Kasama et al., 2021; Siebe et al., 2017; Umar et al., 2018). One of the earthquake events which is one of the backgrounds for this research is a seismic event measuring 6.5 magnitude scale took place on April 14, 2016, at a focal depth of around 10 km in Kumamoto, Japan. Following that, on April 16, 2016, a subsequent earthquake with a magnitude of 7.3 took place at a depth of 10 kilometers. The epicenter of the second earthquake was situated in close proximity to the epicenter of the initial earthquake. The seismic activity was induced by the existence of two active faults, namely the Futagawa and Hinagu faults. The 2016 Kumamoto Earthquakes refer to the two consecutive seismic events in 2016. At that time, Japan had only documented four earthquakes with a seismic intensity of 7. Kumamoto prefecture suffered significant devastation from both the potent foreshock and the subsequent main shock that took place 28 hours later. Mukunoki et al. (2016) reported that the second earthquake resulted in landslides, rock falls, widespread liquefaction, and ground fissures. Multiple landslides occurred on the slopes of Mt. "Aso", impacting both the walls of its caldera and its central volcanic cones. The area surrounding the base of the Aso caldera is mainly composed of pyroclastic flow deposits and eroded gravel.

In Kumamoto area one of the biggest landslide at that time is Takanodai landslide, depicted in Figure 1.3(a). This bird-view image was taken in 2015 prior to the occurrence of the landslide at the location of the Takanodai landslide. From the image, there are several houses located at the end of slope toe, while the Aso Volcanological Laboratory is located near the top. Figure 1.3(b) show the bird view image of a landslide that impacted the houses located near the toe of the slope, the slope of this landslide is approximately 15 degrees. Figure 1.3(c) depicts the bird view image of the slope condition after treatment. According to this image, a notable slope failure occurred on the gently sloping grassy western side of a smaller volcano connected to Mt. Aso. The failed soil mass became dislodged and experienced expansion, resulting in the burial of houses at Takanodai. A consensus among geotechnical researchers studying landslides in the Takanodai area concluded that the cause of this particular landslide was a slip plane consisting of a pumice layer (Chiaro et al., 2022; Hazarika et al., 2019; Kasama et al., 2021; Sumartini et al., 2018; Umar et al., 2018). The geological data collected by Kasama et al. (2021) in Figure 1.2 reveals the presence of a thin layer of pumice located between 9.30 and 9.40 meters below the ground surface. This pumice layer is identified as the primary factor to causes earthquake-induced landslides on gently inclined slopes. In order to clarify the failure mechanism of the Takanodai landslide, it is still necessary to investigate the geotechnical properties of pumice especially their behavior under dynamic loads. Kasama et al. (2021) discovered the physical characteristics of the pumice fall deposit of Takanodai, Minami-Aso, Kumamoto Prefecture, Japan. Consequently, the reduction in shear strength of pumice fall deposits under earthquake loading is regarded as one of the causes of long-runout landslides at Takanodai. In addition, Kasama evaluated the single-particle strength of the pumice. The single-particle strength of pumice fall deposit is one order less than that of carbonate sand, well-known crushable sand, and two orders less than that of typical silica sand like Toyura sand. Apart from that, research on pumice in other locations by Orense RP & Pender MJ (2013) studied pumice liquefaction using material from Waikato, New Zealand, which also states that pumice is crushable. Hence, empirical liquefaction evaluation methods for coarse-grained sands may not be applicable to pumice. Undrained cyclic triaxial tests were performed, and the study found that relative density has a smaller effect on the liquefaction resistance of pumice compared to hard-grained sand. It is also reported that a larger number of cyclic loading is needed to reach the liquefaction state of pumice for low confining pressure. Faris & Fawu (2014) examined pumice debris that causes landslides in West Sumatra, Indonesia. The study examined the effects of effective confining pressure and starting shear stress on the pore pressure increase from the cyclic triaxial testing. Afterward, a study by Asadi et al. (2022) showed that natural pumice has a larger cyclic yield strain rather than general quartz sands due to low G_{max} and higher cyclic resistance ratio (CRR), even with varying σ_c and relative density (D_r) values. The cyclic box shear experiments by Kasama et al. (2021) using a pumice fall deposit for the pumice sample collected from Takanodai, Japan, show that shear stress and vertical stress decrease for constant volume conditions. The stress path for pumice fall deposits under constant-volume loading has cyclic mobility similar to that of liquefied soil. Several researchers review the characteristics of crushable materials by testing single-particle strength tests (Bengtsson, 2021; He et al., 2022; Kwag et al., 1999; Nakata et al., 2001; Yoshimoto et al., 2012). Subsequently, Shen et al. (2016) in his study mentioned particle shape affects the strength of the manufactured sand particle.

Furthermore, the majority of those studies still rely on conventional frequentist or statistical sampling theory when discussing the findings of the conducted tests. Baecher (2017) argued that the conventional frequentist approach to statistical thinking is only applicable in specific scenarios, such as large-scale scientific experiments like medical trials or sociological surveys like the US Census. It is designed for problems where data has been obtained through a meticulously planned and randomized series of experiments.

It is specifically designed to address aleatory uncertainty, which refers to uncertainty related to natural variations. This is typically not comparable to the difficulties that the average person, and particularly not to those that geotechnical engineers face. The majority of geotechnical uncertainties are epistemic, meaning they arise from limited knowledge and uncertainties within the mind rather than variations in the natural environment (Baecher, 2017; Contreras et al., 2018; Phoon et al., 2022).

Baecher (2017) also states that the majority of geotechnical professionals behave Bayesianly. As mentioned in Baecher (2017), the conventional frequentist theory does not meet discipline requirements and should be used cautiously. In addition to behavioral observation, Bayesian thinking can be influential. It helps draw strong conclusions from limited or inconclusive data. It lets us draw quantitative conclusions from qualitative data. It allows logical deductions about prospective likelihood events. It quantitatively supports observation. It integrates diverse data into consistent probability statements. Understanding the simple mathematical principles behind Bayesian reasoning helps people use data and observations to improve their analytical skills. More informed and accurate decisions can result from Bayesian reasoning. By understanding Bayesian reasoning, people can make better predictions based on data and judgments. In this study, we will implement the Bayesian theory to explore pumice behavior.

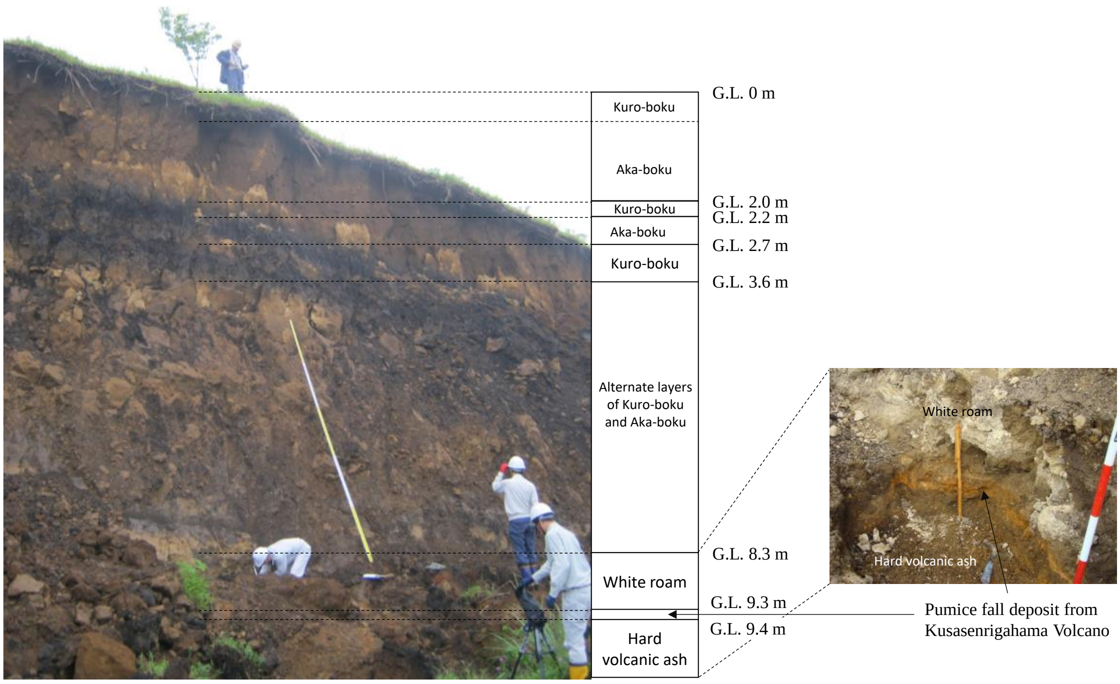

Figure 1.2 Geological condition at Takanodai landslide 2016 (Kasama et al., 2021)

Figure 1.3 Takanodai landslide before and after

1.2 Objectives and Scopes

This study aims to characterize the geotechnical properties of pumice under static and cyclic loading through several parameters such as single-particle strength, shear strength, and liquefaction strength in terms of confining pressure and density. This study also examined the microstructural properties of the pumice, in addition to its chemical characteristics. Moreover, one of the originalities in this study is to introduce the hierarchical Bayesian approach to interpret and characterize pumice behavior accurately from the probabilistic and statistical points of view. Moreover, the specific objective is mentioned as follows:

1. To identify the geological, chemical, and microstructural characteristics of pumice.
2. To explore the relationship between pore characteristics and the mechanical behavior of pumice particles.
3. To compare the particle characteristics and soil matrix characteristics of pumice using a one-dimensional consolidation test.
4. To analyze the liquefaction resistance of pumice under various confining pressures and density variations.
5. To evaluate the effectiveness of the hierarchical Bayesian approach in explaining pumice mechanical behavior.

1.3 Original Contribution

This study aims to evaluate the behavior of pumice, which is generally found in volcanic areas. The new findings obtained in this test, which are considered to be the originality of this study, are as follows:

1. Offering a comprehensive description of pumice, encompassing detailed geological, chemical, and microstructural characteristics. This research has the potential to enhance our comprehension of pumice as a substance and its possible uses in several sectors such as civil engineering.
2. Investigating the mechanisms of pore characteristics impact the mechanical properties of pumice particles. This correlation has the potential to enhance the accuracy of pumice performance forecasts in real-world scenarios and provide valuable insights for developing materials that take advantage of pumice characteristics.
3. Creating a framework for comparing the distinct features and commonalities of

pumice particles and soil matrix properties during compression circumstances. This could improve the comprehension of pumice behavior within soil matrices, specifically in the context of geotechnical engineering applications.

4. Investigating the liquefaction resistance of pumice under varying confining pressures and density conditions. This has the potential to have a substantial effect on the design and safety concerns in areas prone to earthquakes where there are soils rich in pumice. This can help to enhance tactics for reducing the risks associated with earthquakes.
5. Demonstrating the effectiveness of the hierarchical Bayesian approach in modeling and forecasting the mechanical behavior of pumice. This could present a novel analytical technique in the realm of geotechnical engineering, providing a robust statistical tool for future study and practical uses.

1.4 Framework

This study comprises seven chapters organized within a framework to accomplish the research objective, as depicted in Figure 1.4. The structure of each chapter is delineated as follows:

Chapter 1 provides an overview of the context and history of this research. The volcano distribution and earthquake events map in this chapter shows the importance of examining the dynamic characteristics of the material in this special area. Furthermore, it emphasizes the importance of conducting tests on pumice due to its unique pore characteristics and various failure events. Additionally, there is a brief explanation of the benefits of the Bayesian approach as an alternative approach for engineering purposes.

Chapter 2 offers a brief literature review that discusses basic concepts related to chemical, microstructural, single-particle strength tests, liquefaction, and the Bayesian approach based on previous researchers.

Chapter 3 focuses on an analysis of the geologic, chemical, and microstructure properties of pumice. It explains the geology condition of the sampling area, and chemical composition as observed through X-ray fluorescence (XRF), Energy Dispersive Spectroscopy (EDS), and X-ray diffractometry (XRD) tests. The problematic nature of this material is attributed to the presence of pores in the pumice, as observed through Scanning Electron Microscopy (SEM).

Chapter 4 provides a discussion of the mechanical characteristics of pumice particles.

Understanding the properties of pumice particles is crucial due to the distinctive nature and characteristics of pumice. Therefore, it is essential to examine its behavior by conducting single-particle strength testing on pumice particles. This chapter also applies the hierarchical Bayesian approach to assess its effectiveness.

Chapter 5 examines the crushability characteristics of the soil matrix using a one-dimensional consolidation constant rate strain loading test. This test aims to examine the relationship between the yield stress of the pumice matrix and its susceptibility to crushing. Additionally, this test allows us to figure out the disparities in crushability characteristics between pumice and other common materials like clay or sand. Furthermore, this analysis examines the compressible connection between individual pumice particles and the soil matrix of pumice.

Chapter 6 explores the assessment of the shear strength properties of pumice. Undrained triaxial tests were conducted, involving both static and cyclic loading. In this chapter, we look at the liquefaction potential in the cyclic undrained triaxial test. Several conditions with different tests on the density and confining pressure changes are applied here. The results are then compared with those of other materials. In addition, a hierarchical Bayesian approach was employed to assess the liquefaction potential of the pumice.

Chapter 7 provides a summary, conclusion, main findings of this study, and recommendations for future studies.

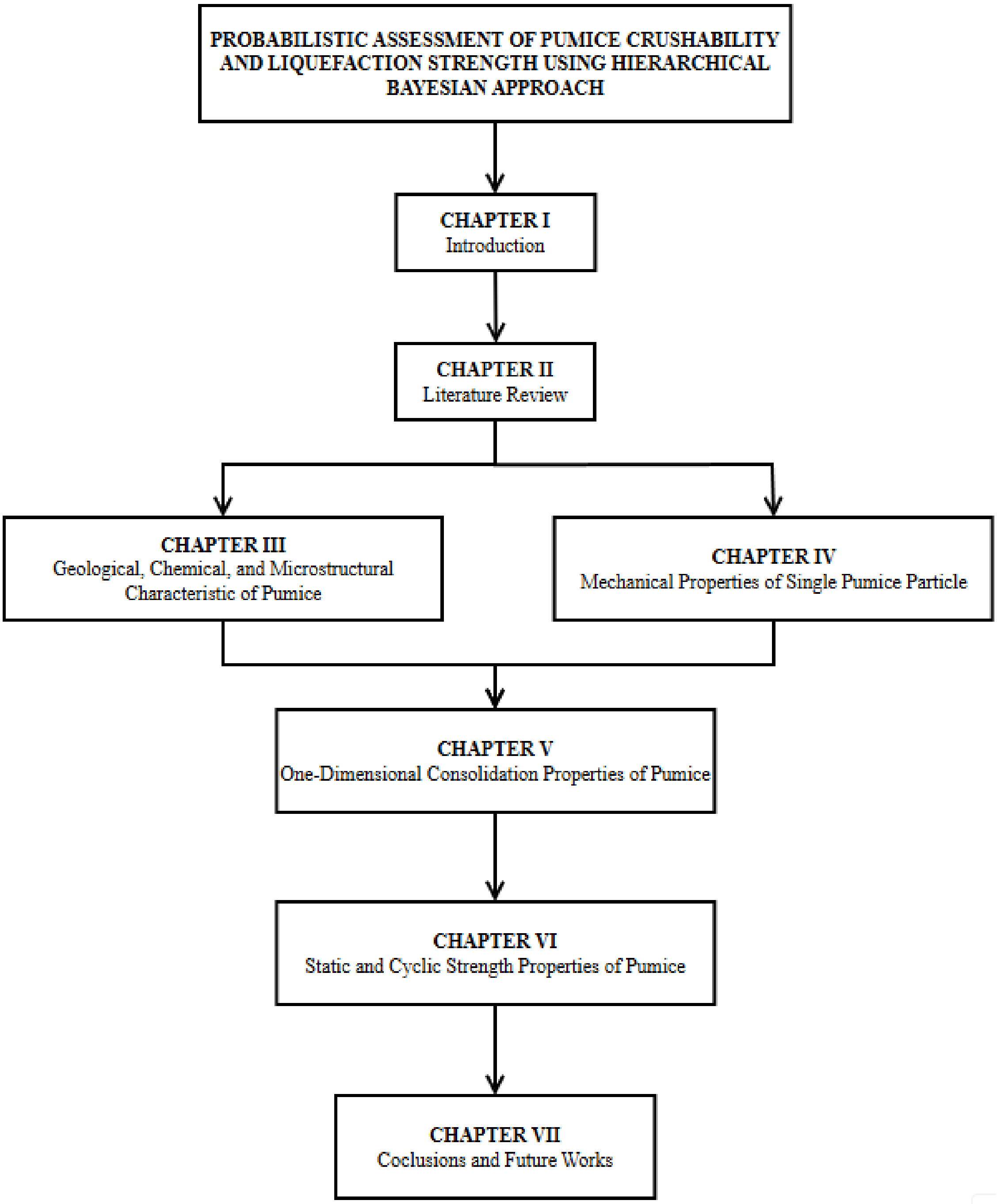

Figure 1.4 Research framework

References

Asadi, M. B., Orense, R. P., Asadi, M. S., & Pender, M. J. (2022). A unified approach to link small-strain shear modulus and liquefaction resistance of pumiceous sand. Soils and Foundations, 62(1). https://doi.org/10.1016/j.sandf.2021.101098

Baecher, G. B. (2017). Bayesian thinking in geotechnics. Geo Risk, 1–18. https://doi.org/10.1061/9780784480694.001

Bengtsson, M. (2021). Empirical Energy and Size Distribution Model for Predicting Single Particle Breakage in Compression Crushing. Mineral Engineering, 171, 1–9.

Chiaro, G., Kiyota, T., Umar, M., & Cappellaro, C. (2022). Earthquake-Induced Flow-Type Slope Failure in Weathered Volcanic Deposits—A Case Study: The 16 April 2016 Takanodai Landslide, Japan. Geosciences, 12(11), 1–22. https://doi.org/10.3390/ geosciences12110394

Contreras, L. F., Brown, E. T., & Ruest, M. (2018). Bayesian data analysis to quantify the uncertainty of intact rock strength. Journal of Rock Mechanics and Geotechnical Engineering, 10(1), 11–31. https://doi.org/10.1016/j.jrmge.2017.07.008

Crosta, G. B., Imposimato, S., Roddeman, D., Chiesa, S., & Moia, F. (2005). Small fast-moving flow-like landslides in volcanic deposits: The 2001 Las Colinas Landslide (El Salvador). Engineering Geology, 79(3–4), 185–214. https://doi.org/10.1016/ j.enggeo.2005.01.014

Faris, F., & Fawu, W. (2014). Investigation of the initiation mechanism of an earthquake-induced landslide during rainfall: a case study of the Tandikat landslide, West Sumatra, Indonesia. Geoenvironmental Disasters, 1(4).

Fisher, R. V. (1961). Proposed classification of volcaniclastic sediments and rocks. Bulletin of the Geological Society of America, 72(9), 1409–1414. https://doi.org/10.1130/0016-7606(1961)72[1409:PCOVSA]2.0.CO;2

Fisher, R. V., & Schmincke, H. U. (1984). Pyroclastic Rocks. Springer-Verlag Berlin Heidelberg. https://doi.org/10.1007/978-3-642-74864-6 e-ISBN-13

Global Volcanism Program. (2023, December 15). [Database] Volcanoes of the World (v. 5.1.5; 15 Dec 2023). Distributed by Smithsonian Institution, Compiled by Venzke, E.

Hazarika, H., Sumartini, W. O., Kokusho, T., Kochi, Y., Ishibashi, S., Yamamoto, S., & Matsumoto, D. (2019). Investigation on mechanism of landslides during the 2016

Kumamoto earthquake, Japan. Earthquake Geotechnical Engineering for Protection and Development of Environment and Construction, 821–832.

He, Y., Cai, G., Gao, L., & He, H. (2022). Effect of Particle Size and Constraint Conditions on Single Particle Strength of Carbonate Sand. Sensors, 22(3). https://doi.org/10.3390/s22030765

Hosobuchi, M. N., Chigira, M., Lim, C., & Komoo, I. (2021). Geological history controlling the debris avalanches of pyroclastic fall deposits induced by the 2009 Padang earthquake, Indonesia: The sequential influences of pumice fall, weathering, and slope undercut. Engineering Geology, 287. https://doi.org/10.1016/j.enggeo.2021.106104

Kasama, K., Furukawa, Z., & Yasufuku, N. (2021). Cyclic shear property and seismic runout analysis for pumice fall deposit. Soil Dynamics and Earthquake Engineering, 143, 1–11. https://doi.org/10.1016/j.soildyn.2021.106588

Kwag, J. M., Ochiai, H., & Yasufuku, N. (1999). Yielding Stress Characteristics of Carbonate Sand in Relation to Individual Particle Fragmentation Strength. In Al-Shafei (Ed.), Engineering for Calcareous Sediments (pp. 79–86).

McPhie, J., Doyle, M., & Allen, R. (1993). Volcanic textures: A guide to the interpretation of textures in volcanic rocks. CODES Key Centre, University of Tasmania.

Nakata, Y., Kato, Y., Hyodo, M., Hyde, A. F. L., & Murata, H. (2001). One-Dimensional Compression Behaviour of Uniformly Graded Sand Related to Single Particle Crushing Strength. Soils and Foundations, 41(2), 39–51.

Orense RP, & Pender MJ. (2013). Liquefaction characteristics of crushable pumice sand. Proceedings of the 18th International Conference on Soil Mechanics and Geotechnical Engineering, 1559–1562.

Phoon, K. K., Cao, Z. J., Ji, J., Leung, Y. F., Najjar, S., Shuku, T., Tang, C., Yin, Z. Y., Ikumasa, Y., & Ching, J. (2022). Geotechnical uncertainty, modeling, and decision making. Soils and Foundations, 62(5). https://doi.org/10.1016/j.sandf.2022.101189

Shen, W., Yang, Z., Cao, L., Cao, L., Liu, Y., Yang, H., Lu, Z., & Bai, J. (2016). Characterization of manufactured sand: Particle shape, surface texture and behavior in concrete. Construction and Building Materials, 114, 595–601. https://doi.org/10.1016/j.conbuildmat.2016.03.201

Siebe, C., Salinas, S., Arana-Salinas, L., Macías, J. L., Gardner, J., & Bonasia, R. (2017). The ~23,500 y 14C BP White Pumice Plinian eruption and associated debris avalanche and Tochimilco lava flow of Popocatépetl volcano, México. Journal of Volcanology and Geothermal Research, 333–334, 66–95. https://doi.org/10.1016/j.jvolgeores .2017.01.011

Simkin, T., Tilling, R. I., Vogt, P. R., Kirby, S. H., Kimberly, P., & Stewart, D. B. (2006). This dynamic planet: World map of volcanoes, earthquakes, impact craters, and plate tectonics: U.S. Geological Survey Geologic Investigations Series Map I-2800, 1 two-sided sheet, scale 1:30,000,000.

Sumartini, W. O., Hazarika, H., Kokusho, T., Ishibashi, S., Matsumoto, D., & Chaudhary, B. (2018). Deformation and Failure Characteristics of Volcanic Soil at Landslides Site due to the 2016 Kumamoto Earthquake. International Association of Lowland Technology, 19(4), 237–244.

Umar, M., Chiaro, G., Kiyota, T., & Miyamoto, H. (2018). Monotonic and Cyclic Undrained Behavior of Kumamoto-Aso Pumice by Triaxial And Torsional Shear Test. 16th European Conference on Earthquake Engineering.

Yoshimoto, N., Hyodo, M., Nakata, Y., Orense, R. P., Hongo, T., & Ohnaka, A. (2012). Evaluation of shear strength and mechanical properties of granulated coal ash based on single particle strength. Soils and Foundations, 52(2), 321–334. https://doi.org/10.1016/j.sandf.2012.02.009

Zhang, X., Baudet, B. A., & Yao, T. (2020). The influence of particle shape and mineralogy on the particle strength, breakage and compressibility. International Journal of Geo-Engineering, 11(1). https://doi.org/10.1186/s40703-020-0108-4

Zhao, B., Wang, J., Coop, M. R., Viggiani, G., & Jiang, M. (2015). An investigation of single sand particle fracture using X-ray microtomography. *Géotechnique*, *65*(8), 625–641.

This page intentionally left blank

CHAPTER II
LITERATURE REVIEW

2.1 Introduction

As the previous chapter stated, pumice frequently poses several issues. To thoroughly assess the characteristics and issues associated with pumice, it is crucial to examine its chemical composition and microstructural properties, which will serve as the foundation for further analysis. Subsequently, examine its responses to both static and cyclic stresses to determine its overall behavior. Lastly, the hierarchical Bayesian approach was employed to acquire comprehensive outcomes. In this chapter, we will discuss the basic theories that support those analyses.

2.2 Pumice

Scoria, cinders, and pumice are three common names that are influenced by the amount of vesicularity. They are used irrespective of size, however typically fall within the volcanic gravel or larger size category. Pumice is a lightweight, porous glass foam that is typically white, pale gray, or brown. It has a high silica and mafic content and can float on water due to its vesicular nature and the bubble walls in soil particles are made of translucent glass. Scoria and cinders, which are essentially synonymous terms, are juvenile fragments of mafic composition that are highly inflated less than pumice, they are easily submerged in water.

Silicic pumice typically exhibits high porosity (up to 90%) and a density of less than 1.0 g/cm^3, along with low permeability. There are two types of silicic pumice: fibrous fragments with tubular, subparallel vesicles and fragments with spherical to subspherical vesicles. Fibrous types have vesicle length/diameter ratios greater than 20. Vesicles undergo distortion and stretching during vesiculation, extrusion, and flowage processes, with smaller vesicles typically maintaining a spherical shape. Pumice with spherical vesicles indicates high vapor pressure during eruptions, while fibrous pumice is characteristic of eruptions with lower pressures (Fisher & Schmincke, 1984). In general, pumice has pores which can be seen in Figure 2.1.

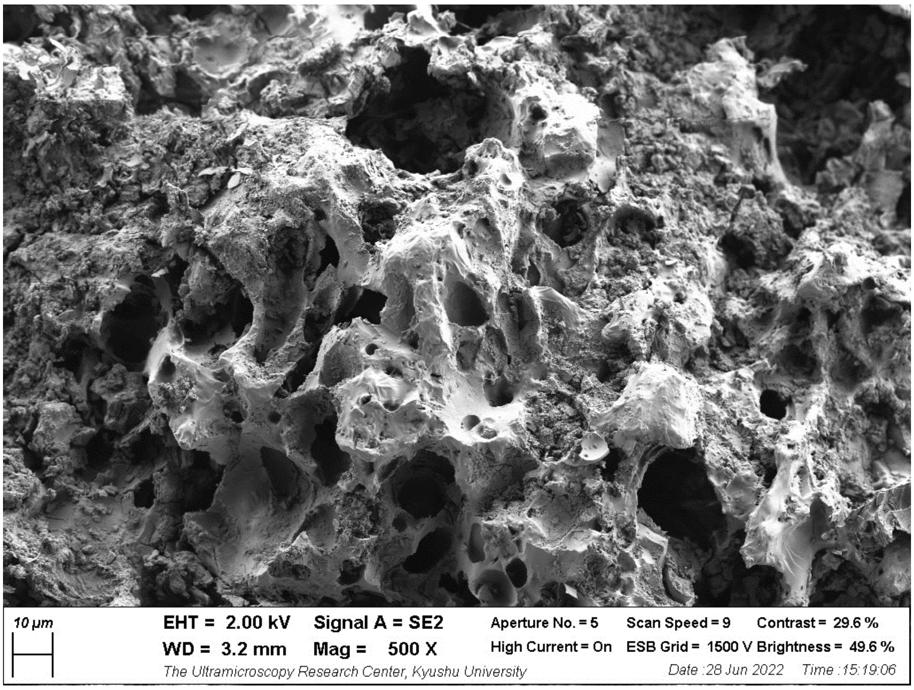

Figure 2.1 Pumice under the SEM test (Basoka et al., 2024).

2.3 Single-Particle Strength

The strength of individual particles plays a crucial role in assessing the stability and load-bearing capacity of soils and rockfill materials in geotechnical engineering. Comprehending the strength of individual particles is crucial for evaluating particle fragmentation and the overall durability of constructed structures. To understand the behavior of pumice particles comprehensively, it is important to take into account both the fundamental characteristics of pumice and the consequences due to the existence of the pumice layer. Several researchers conducted individual particle strength tests to analyze the properties and behavior of the particles within a soil material. The main purpose of the single-particle strength test is to evaluate the strength property of individual particles for compression or breakage under a specific force, several researchers have already discovered the single-particle strength of highly crushable soil particles based on single-particle strength test (Basoka et al., 2023a, 2023b, 2023c; Bengtsson, 2021; He et al., 2022; Kasama et al., 2021; Kwag et al., 1999; Liburkin et al., 2015; Liu et al., 2021; Nakata et al., 2001; Tavares, 2022; Yoshimoto et al., 2012; Zhang et al., 2020; Zhao et al., 2015).

In their study, Kwag et al. (1999) looked for the characteristics of single-particle carbonate sand strength. In their research, several carbonate sands were tested, and the single-particle strength was described by Eq. 2.1.

$$\sigma_1 = \frac{F_1}{A} \qquad \text{Eq. 2.1}$$

where σ_1 is the first failure stress, A is the area of the soil sample, and F_1 is the first peak of the single-particle crushability test result, as can be seen in Figure 2.2. In their study, Kwag et al. (1999) also conducted isotropic compression tests on the crushability behavior of various materials. Eq. 2.2 expresses the relationship between yield stress (p_c), relative density (D_r), and crushability index (K), as discovered in this study.

$$p_c = \exp(A_k D_r + K) \qquad \text{Eq. 2.2}$$

where A_k is the parameter of density for yield stress. The constant A_k determines the gradient of the linear lines representing the relationship between the magnitudes of $D_r - logp_c$. The values of K, on the other hand, are determined by the value of lnp_c when D_r is equal to 0%. According to Kwag et al. (1999), the constant A_k has a value of approximately 2.27 regardless of the material type. This allows for the calculation of the K value using Eq. 2.3.

$$K = \ln p_c - 2.27 D_r \qquad \text{Eq. 2.3}$$

Nakata et al. (2001) conducted experiments to determine the strength of single particles, these tests were performed on multiple soils. The study involved conducting single particle tests and one-dimensional compression tests. Nakata et al. (2001) also observed the effect of the roundness coefficient and roundness coefficient representing particle shape on the crushability of soil particles. It can be calculated using Eq. 2.4.

$$roundness\ coefficient = \frac{(particle\ perimeter)^2}{4\pi A} \qquad \text{Eq. 2.4}$$

where A is the area of the particle. In addition, Nakata et al. (2001) described the relationship between the single-particle strength test and the one-dimensional compression test, which is expressed in Eq. 2.5.

$$F_{sp} = \sigma \left(\sqrt[3]{\frac{(1+e)\pi}{6}} \right)^2 \bar{d}^2 \quad \text{Eq. 2.5}$$

where F_{sp} is the force on a single-particle strength embedded in a soil matrix, σ is the normal stress, which in this study refers to yield stress (p_c), $\bar{d}$ is the mean particle diameter, and e is the void ratio.

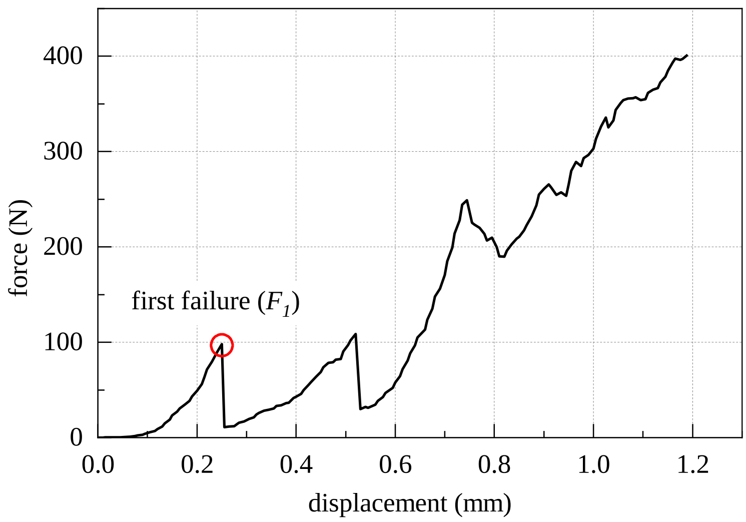

Figure 2.2 Typical test result of a single-particle strength test.

Basoka et al. (2023) conducted a single-particle strength test for pumice in terms of examining the effect of the roundness coefficient and aspect ratio. Figure 2.3(b) illustrates the roundness coefficient, while Figure 2.3(a) illustrates the aspect ratio, which can be calculated using Eq. 2.6.

$$aspect\ ratio = \frac{major\ axis}{minor\ axis} \quad \text{Eq. 2.6}$$

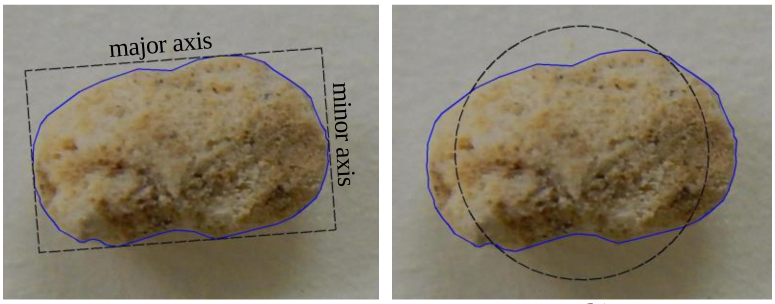

(a) (b)

Figure 2.3 (a) aspect ratio (b) roundness

2.4 Liquefaction

During seismic activity, the pore water pressure in saturated sand rises rapidly, causing the effective stress to decrease to zero. This results in the soil changing from a solid state to a viscous fluid mass called the liquefaction phenomenon. Under these conditions, sand can liquefy, which causes related phenomena like sand boiling, ground cracking, and lateral spread. Liquefaction is a significant factor contributing to the instability of buildings and structures during earthquakes. It is also a crucial aspect of seismic research and design, particularly foundations. Almost every strong earthquake causes remarkable and destructive widespread ground deformation due to liquefaction, which damages soils and foundations (Huang & Yu, 2013).

A significant attention from geotechnical and structural engineers was the occurrence of liquefaction in the Niigata area of Japan on June 16, 1964. There is a lot of damage even though the earthquake magnitude was below 7.5 according to a report by Kawasumi (1968). The seismic intensity of the international scale on solid ground in the city of Niigata was only 8. The wooden houses in the old town, which were constructed in the 16th century, have remained largely intact. Only 3% of these wooden houses have been completely demolished throughout the entire city. In contrast, more than 25% of the modern concrete buildings in the new city, which were built on unstable foundations, have experienced severe structural damage. It is important to emphasize that, despite the destruction of 1960 houses throughout the entire area, the earthquake resulted in only 28 fatalities. This number is significantly lower than those for typical Japanese earthquakes with similar magnitudes. Ishihara & Koga (1981) acquired undisturbed sand samples from two locations in the Niigata city area. These samples were then subjected to laboratory testing under cyclic triaxial loading conditions. The test data were utilized in the liquefaction analysis to compare the ground behaviors at these two sites observed during the 1964 earthquake. The cyclic stress ratio (*CSR*) and the number of cycles needed are some of the parameters to quantify soil strengths under cyclic loading conditions. The cyclic stress ratio is the ratio of the amplitude of the cyclic axial stress to twice the initial effective confining pressure. The specimen is considered to reach failure condition or liquefaction either when the excess pore water pressure is equal to the initial effective confining pressure or when the double amplitude of axial strains reaches 5%. It is noted that 5% of double amplitude axial strains are considered to be the occurrence of liquefaction according to the Japanese Geotechnical Society Standard (JGS 0541-2020) about the methods for cyclic undrained triaxial tests on soils. The calculation of cyclic stress ratio was calculated as Eq. 2.7.

$$CSR = \frac{P}{2A_c\sigma_0{}'} \qquad \text{Eq. 2.7}$$

where P is cyclic axial load, A_c is the sample area after the consolidation, and $\sigma_0{}'$ is the initial effective confining pressure.

It is conventionally known that the cyclic triaxial test is commonly employed to quantify the liquefaction strength. Namely, *CSR* and excess pore pressure obtained from the cyclic triaxial compression test are used to evaluate the liquefaction potential. Orense RP & Pender MJ (2013) conducted a study on the liquefaction of pumice sampled from Waikato, New Zealand. The study also confirmed that pumice is crushable geomaterial. Therefore, conventional methods used for coarse-grained sand may not be suitable for pumice. The study used cyclic triaxial tests under undrained conditions and found that relative density has less effect on the liquefaction resilience of pumice compared to hard-grained sand. Additionally, in the cyclic triaxial test lower confining pressure with the same density required a higher number of cyclic to reach the liquefaction state compared to higher confining pressure.

Kasama et al., (2021) did cyclic box shear experiments on a pumice fall deposit from Takanodai, Japan. The results show that both shear stress and vertical stress against cyclic vertical displacement for constant volume conditions decrease. The stress path of pumice fall deposits subjected to cyclic vertical displacement under constant volume conditions exhibits cyclic mobility that is comparable to that of liquefied soil. Faris and

Fawu, (2014) investigated the geotechnical property of pumice debris responsible for triggering landslides in West Sumatra, Indonesia. The study investigates the effect of the confining pressure and initial shear stress affect to pore water pressure build-up during the triaxial test. Asadi et al., (2022) demonstrated that natural pumice exhibits a greater cyclic yield strain compared to typical quartz sands, and this is attributed to their lower G_{max} and higher resistance to liquefaction often called cyclic resistance ratio (*CRR*), regardless of variations in D_r values. Seed and Idriss (1971) suggested using 10 cycles for earthquakes with a moment magnitude (Mw) of 7, 20 cycles for Mw 7.5, and 30 cycles for Mw 8. Ishihara (1993) utilized 20 cycles to examine an earthquake of magnitude 7.5, as measured on the moment magnitude scale. Rahman and Sitharam (2020) also employed 20 cycles to assess liquefaction strength. Researchers have proposed different cycle numbers, such as 10 cycles for Mw 7 earthquakes, 20 cycles for Mw 7.5, and 30 cycles for Mw 8, in order to capture the liquefaction behavior effectively. Therefore, selecting the appropriate number of cycles is essential for reliable liquefaction assessments.

2.5 Bayesian Inference

Data inference can be classified into two estimations. One of the estimations is a point estimation, which is a pinpoint estimation of an unknown parameter showing high likelihood. At the same time, the other is interval estimation, a range estimation for unknown parameters generally blanked between lower and upper values. In the frequentist approach, parameters and hypotheses are considered unknown but constant (non-probabilistic) values. As a result, it is not possible to make probabilistic statements about these unknowns. On the other one, the Bayesian approach is entirely prescriptive, although there are substantial practical challenges to address, such as determining the likelihood and specifying the prior, to follow that prescription. Additionally, when frequentist approach runs into problems, Bayesian approach often needs very specific prior information to keep posterior distributions from acting strangely (Wakefield, 2013).

In the Bayesian framework of data inference, any unknown quantities present in a probability model for the observed data are regarded as random variables. Conversely, the frequentist perspective regards parameters as unchanging constants. More precisely, in the Bayesian approach, the fixed but unknown parameters and hypotheses that we want to infer are considered random variables. Furthermore, the unknown parameters and valuables may encompass both incomplete data and the actual covariate value in a scenario involving errors-in-variables (Wakefield, 2013).

Let $\theta = \left[\theta_1, \ldots, \theta_p\right]^T$ denote all of the unknowns of the model, which we continue to refer to as parameters, and $y = [y_1, \ldots, y_n]^T$ the vector of observed data. Also, let $\mathcal{I}$ represent all relevant information that is currently available to the individual who is carrying out the analysis, in addition to y. In the following description, we assume for simplicity that each element of θ is continuous.

$$p(\theta|y, \mathcal{I}) = \frac{p(y|\theta, \mathcal{I})\pi(\theta|\mathcal{I})}{p(y|\mathcal{I})} \qquad \text{Eq. 2.8}$$

The two essential components are the likelihood function $p(y|\theta, \mathcal{I})$ and the prior distribution $\pi(\theta|\mathcal{I})$. The latter represents the probability beliefs for θ held before observing the data y. Both rely on the present data $\mathcal{I}$ possess. Individuals will possess varying information regarding $\mathcal{I}$, resulting in potential differences in their prior distributions (and potentially their likelihood functions) on a general level. The denominator in Eq. 2.8, denoted as $p(y|\mathcal{I})$, serves as a normalizing constant. Its purpose is to guarantee that the integral of the right-hand side of the equation equals one across the entire parameter space. Although of vital significance, for the sake of simplicity in notation, we will now disregard the dependence on $\mathcal{I}$, resulting in Eq. 2.9 and normalizing constant in Eq. 2.10.

$$p(\theta|y) = \frac{p(y|\theta)\pi(\theta)}{p(y)} \qquad \text{Eq. 2.9}$$

where the normalizing constant is

$$p(y) = \int_\theta p(y|\theta)\pi(\theta)d\theta \qquad \text{Eq. 2.10}$$

The marginal probability refers to the probability of the observed data given the model, which includes both the likelihood and the prior. Disregarding this constant yields in Eq. 2.11.

$$p(\theta|y) \propto p(y|\theta) \times \pi(\theta) \qquad \text{Eq. 2.11}$$

or, in simpler terms,

$$Posterior \propto Likelihood \times Prior$$

It makes sense to use the posterior distribution for inference because it probabilistically combines information about the parameters in the data with the prior; this is very appealing. Initially, the Bayesian approach of inference may appear deceptively simple, but in practice, there are several significant factors that need to be taken into account. The first, unquestionably crucial, matter is pre-determination. Next, after determining the prior and likelihood components, we must summarize the typically multivariate posterior distribution. This summarization process involves integrating over the parameter space, which can be of considerable dimension. Ultimately, a Bayesian analysis must consider how potential errors in the model specification affect the process of drawing conclusions.

The key differentiating factor between the field of statistics and the application of statistical techniques in a specific discipline is the systematic approach to concluding the presence of uncertainty. Two primary methodologies for inference, known as Bayesian and frequentist, exist, each yielding inferential procedures that are optimal according to distinct criteria (Wakefield, 2013). The interpretation of probability is a key aspect of the philosophy of each approach. In the frequentist approach, probabilities are interpreted as the theoretical limit of the frequency of an event occurring when the situation is repeated an infinite number of times. Inferential recipes, such as specific estimators, are evaluated based on their performance when the data is repeatedly sampled, assuming that the model parameters are fixed but unknown constants. In contrast, the Bayesian approach described in this dissertation considers probabilities to be subjective and interprets them based on the available information. Therefore, individuals may have varying assigned probabilities for the same event. Probabilities are non-existent in this context, as they fluctuate based on the information that is accessible. In a model, any parameters that are not known are considered to be random variables. Inference is then made by analyzing the probability distribution of these parameters, specifically the posterior distribution, which takes into account the data and other relevant information. In practical terms, the significance of interpreting probability is diminished. The number of assumptions needed for valid inference and the range of inferential questions that can be addressed using a specific approach have implications for the robustness of the analysis. It is important to emphasize that several problems that arise when analyzing regression data, such as the sampling method, interpreting parameters, and misrepresenting the average model, are not influenced by philosophy and are typically more significant in practice than the chosen inferential approach for analysis. Both the frequentist and Bayesian approaches possess their strengths and can often be employed together, a methodology that we adhere to and promote in this dissertation. If there are differences in the main findings between different approaches, investigating the causes of these discrepancies can provide valuable insights. It may uncover that a specific analysis is relying on unsuitable assumptions or that one of the approaches is neglecting important information.

References

Asadi, M. B., Orense, R. P., Asadi, M. S., & Pender, M. J. (2022). A unified approach to link small-strain shear modulus and liquefaction resistance of pumiceous sand. Soils and Foundations, 62(1). https://doi.org/10.1016/j.sandf.2021.101098

Basoka, I. W. A., Kasama, K., & Furukawa, Z. (2023a). Crushability of Pumice Particle Based on Statistical Approach. Japan Society of Civil Engineers Western Branch Research Presentation, 381–382.

Basoka, I. W. A., Kasama, K., & Furukawa, Z. (2023b). Linear Regression Model of Pumice Particle Strength. 58th Japan National Conference on Geotechnical Engineering, 2266–2267.

Basoka, I. W. A., Kasama, K., & Furukawa, Z. (2023c, September 15). Effect of particle shape against pumice particle strength. Japan Society of Civil Engineers Research Presentation Annual Meeting.

Basoka, I. W. A., Kasama, K., Furukawa, Z., Yasufuku, N., & Rifa'i, A. (2023). Microscopy and Mechanical Behavior of pumice single particle. In Z. Hossain (Ed.), 13th Int. Conf. on Geotechnique, Construction Materials & Environment (pp. 120–126). Geomate.

Basoka, I. W. A., Kasama, K., Furukawa, Z., Yasufuku, N., & Rifa'i, A. (2024, May). Pumice sand behavior on undrained cyclic loading. 8th International Conference on Earthquake Geotechnical Engineering.

Bengtsson, M. (2021). Empirical Energy and Size Distribution Model for Predicting Single Particle Breakage in Compression Crushing. Mineral Engineering, 171, 1–9.

Fisher, R. V., & Schmincke, H. U. (1984). Pyroclastic Rocks. Springer-Verlag.

He, Y., Cai, G., Gao, L., & He, H. (2022). Effect of Particle Size and Constraint Conditions on Single Particle Strength of Carbonate Sand. Sensors, 22(3), 1–17. https://doi.org/10.3390/s22030765

Huang, Y., & Yu, M. (2013). Review of soil liquefaction characteristics during major earthquakes of the twenty-first century. Natural Hazards, 65(3), 2375–2384. https://doi.org/https://doi.org/10.1007/s11069-012-0433-9

Ishihara, K. (1993). Liquefaction and flow failure during earthquakes. Géotechnique, 43(3), 351–451. https://doi.org/10.1680/geot.1993.43.3.351

Ishihara, K., & Koga, Y. (1981). Case Studies of Liquefaction in the 1964 Niigata

Earthquake. Soils and Foundations, 21(3), 35–52. https://doi.org/https://doi.org/10.3208/ sandf1972.21.3_35

Kasama, K., Furukawa, Z., & Yasufuku, N. (2021). Cyclic shear property and seismic runout analysis for pumice fall deposit. Soil Dynamics and Earthquake Engineering, 143, 1–11. https://doi.org/10.1016/j.soildyn.2021.106588

Kawasumi, H. (1968). General Report on the Niigata Earthquake of 1964.

Kwag, J. M., Ochiai, H., & Yasufuku, N. (1999). Yielding Stress Characteristics of Carbonate Sand in Relation to Individual Particle Fragmentation Strength. In Al-Shafei (Ed.), Engineering for Calcareous Sediments (pp. 79–86).

Liburkin, R., Portnikov, D., & Kalman, H. (2015). Comparing Particle Breakage in an Uniaxial Confined Compression Test to Single Particle Crush Test-Model and Experimental Result. Powder Technology, 2015(284), 344–354.

Liu, C., Liu, F., Song, J., Ma, F., Wang, D., & Zhang, G. (2021). On the measurements of individual particle properties via compression and crushing. Journal of Rock Mechanics and Geotechnical Engineering, 13(2), 377–389. https://doi.org/10.1016/j.jrmge. 2020.06.009

Nakata, Y., Kato, Y., Hyodo, M., Hyde, A. F. L., & Murata, H. (2001). One-Dimensional Compression Behaviour of Uniformly Graded Sand Related to Single Particle Crushing Strength. Soils and Foundations, 41(2), 39–51.

Orense RP, & Pender MJ. (2013). Liquefaction characteristics of crushable pumice sand. Proceedings of the 18th International Conference on Soil Mechanics and Geotechnical Engineering, 1559–1562.

Seed, H. B., & Idriss, I. M. (1971). Simplified Procedure for Evaluating Soil Liquefaction Potential. Journal of the Soil Mechanics and Foundations Division, 97(9), 1249–1273. https://doi.org/10.1061/JSFEAQ.0001662

Tavares, L. M. (2022). Review and Further Validation of a Practical Single-Particle Breakage Model. KONA Powder and Particle Journal, 39, 62–83. https://doi.org/10.14356/kona.2022012

Wakefield, J. (2013). Bayesian and frequentist regression methods (1st ed.). Springer New York. https://doi.org/10.1007/978-1-4419-0925-1

Yoshimoto, N., Hyodo, M., Nakata, Y., Orense, R. P., Hongo, T., & Ohnaka, A. (2012). Evaluation of shear strength and mechanical properties of granulated coal ash based on single particle strength. Soils and Foundations, 52(2), 321–334. https://doi.org/10.1016/j.sandf.2012.02.009

Zhang, X., Baudet, B. A., & Yao, T. (2020). The influence of particle shape and mineralogy on the particle strength, breakage and compressibility. International Journal of Geo-Engineering, 11(1). https://doi.org/10.1186/s40703-020-0108-4

Zhao, B., Wang, J., Coop, M. R., Viggiani, G., & Jiang, M. (2015). An investigation of single sand particle fracture using X-ray microtomography. Géotechnique, 65(8), 625–641.

This page intentionally left blank

CHAPTER III
GEOLOGICAL, CHEMICAL, AND MICROSTRUCTURAL CHARACTERISTICS OF PUMICE

3.1 Introduction

Pumice which is a material that has pores in its material structure due to the formation process of the pumice itself, causes the pumice to have crushable behavior and is widely distributed in volcanic areas. Several researchers have reported several geotechnical failures of the pumice layer (Faris & Fawu, 2014; Hazarika et al., 2019; Kameda et al., 2019; Kasama et al., 2021; Nishimura et al., 2022; Sumartini et al., 2018). This chapter explains the geology of the sampling area pumice used in this study, the chemical and mineral components of the pumice, and the microstructure of the pumice.

3.2 Sample Preparation and Methodology

3.2.1 Material Sample

To keep the quality of the pumice with small variations in terms of the physical and mechanical characteristics, in this study, pumice sold by agricultural companies was used. This pumice was obtained from the Miyakonojo city, Miyazaki prefecture, Kyushu Island, as shown in Figure 3.1. Figure 3.2 shows a sample of pumice composed primarily of pale white pumice, as shown in Figure 3.3(a), and a small amount of black sand as shown in Figure 3.3(b). The samples were initially dried in an oven at approximately 110^{o} to eliminate the water content.

3.2.2 Methodology

(1) Physical Properties of Pumice

In order to examine the basic physical properties of pumice used in this study, particle size distribution (JGS 0131-2009), soil particle density (JGS 0111-2009), and minimum-maximum density (JGS 0162-2009) were conducted.

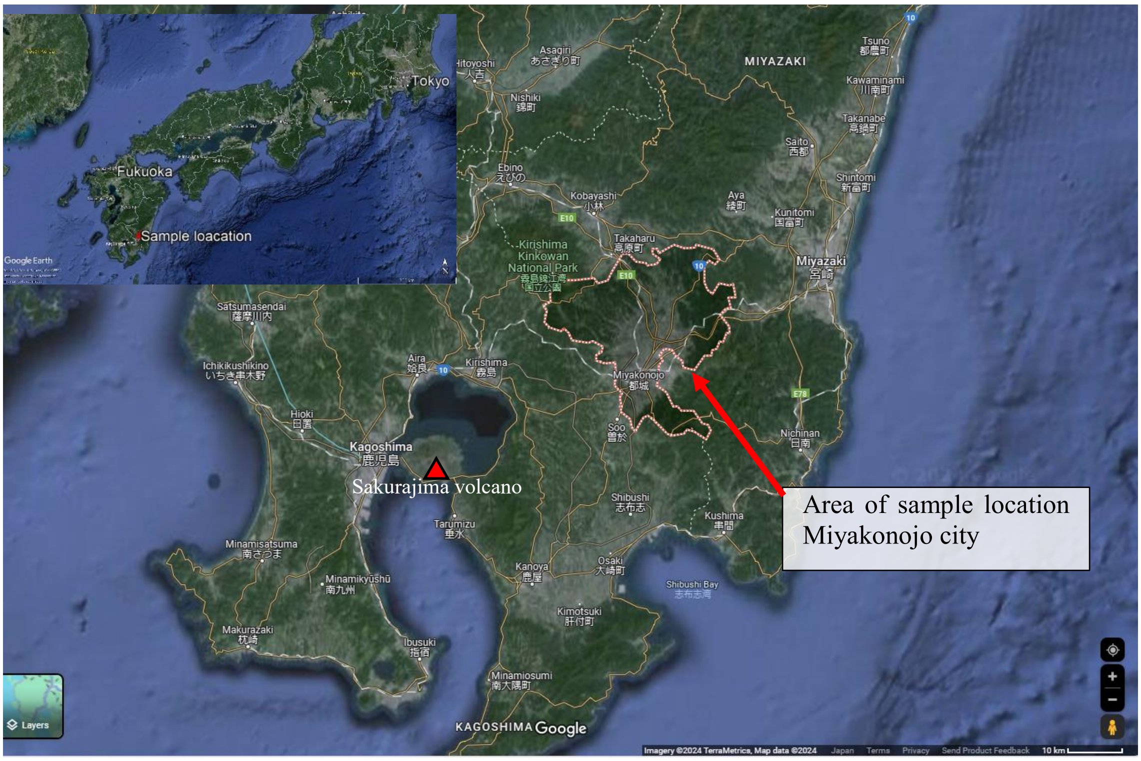

Figure 3.1 Sample location

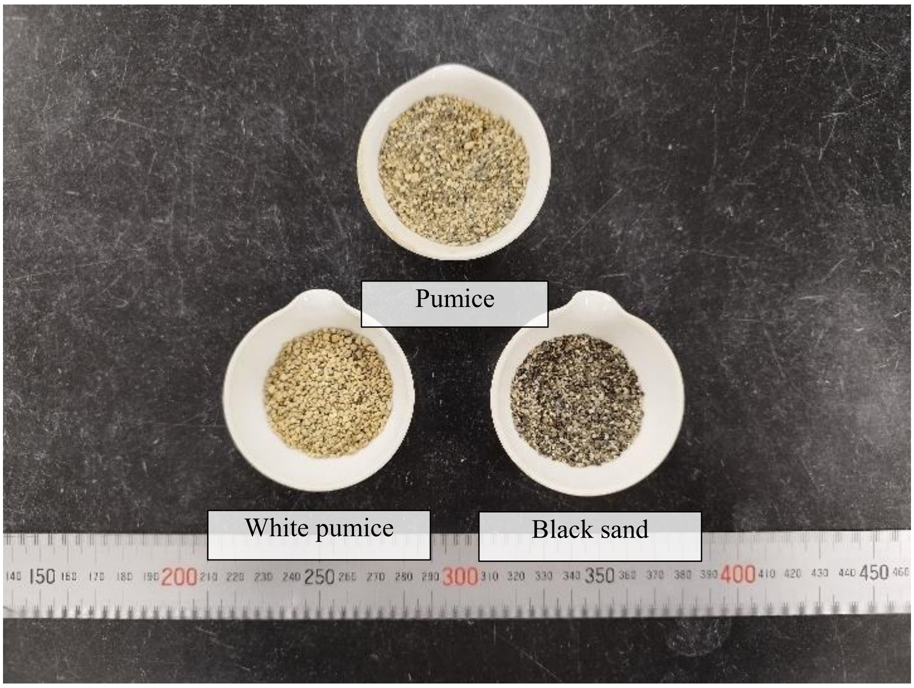

Figure 3.2 Sample of pumice

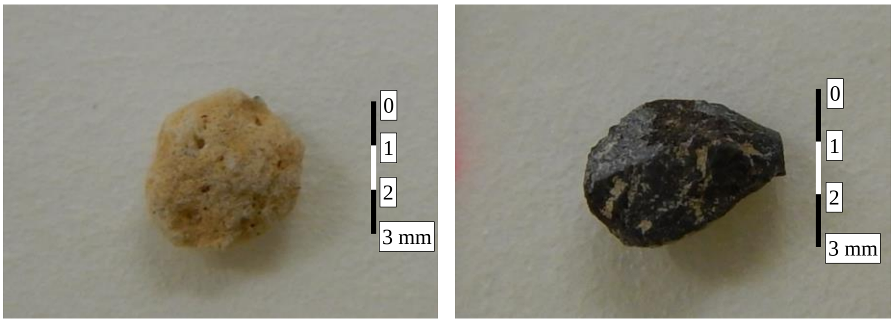

(a) white pumice (b) black sand

Figure 3.3 Particle of sample

(2) X-Ray Fluorescence Analysis

Initially, the pumice sample was thoroughly dried, after which it was crushed into a fine powder. In X-ray fluorescence (XRF) testing, the sample was placed inside a sample tube with a height of about 1 cm and then covered with plastic, as depicted in Figure 3.4. Subsequently, the sample was put into the testing apparatus, as depicted in Figure 3.5, in order to ascertain the chemical components of the pumice.

Figure 3.4 XRF sample

Figure 3.5 XRF apparatus

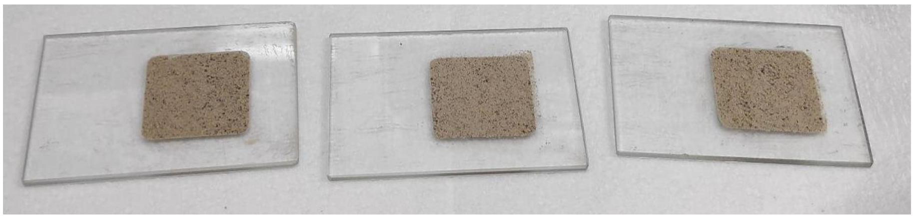

Figure 3.6 XRD sample

Figure 3.7 XRD apparatus

(3) X-Ray Diffractometry Analysis

The sample preparation for X-ray diffractometry (XRD) analysis closely resembles that of XRF testing. It involves grinding the dry sample into a fine powder, which was subsequently deposited onto a glass plate with a thickness of approximately 0.50 mm, as shown in Figure 3.6. Subsequently, the sample was placed into the XRD instrument, as shown in Figure 3.7, for testing purposes. Subsequently, the XRD testing results need to be further scrutinized using distinct software, specifically PDXL2, in order to ascertain the mineral components of pumice.

(4) Scanning Electron Microscopy and Energy Dispersive Spectroscopy Analysis

A Scanning Electron Microscopy (SEM) test was conducted to obtain a microscopic image of pumice. The objective of this study is to ascertain the properties of the pores in the pumice both prior to and following testing. The SEM testing was conducted at the Ultramicroscopy Research Center of Kyushu University using a high vacuum SEM (TES+ULTRA55 model). In order to perform high vacuum SEM, it is necessary to apply a coating layer to the sample beforehand. Two coating materials such as carbon and platinum are utilized as shown in Figure 3.8. According to Lee, R. (1995), using a platinum coating in the sample produces image results with higher resolution. Therefore, this study used a platinum coating. Platinum-coated samples, as shown in Figure 3.9, can be grouped into sets of 9 samples per test. Next, the sample that had been coated was placed into the SEM apparatus, following the procedure shown in Figure 3.10. In SEM analysis, an Energy Dispersive Spectroscopy (EDS) apparatus can be performed to investigate chemical components on the surface of the pumice. For the EDS test, it was necessary to establish the location of the observation point in order to subsequently analyze the chemical components. Prior to the EDS test, the result from the XRF analysis was used as a preliminary reference for identifying the chemical components of the EDS analysis.

(a) carbon coating (b) platinum coating

Figure 3.8 Sample coating

Figure 3.9. SEM and EDS sample after coating

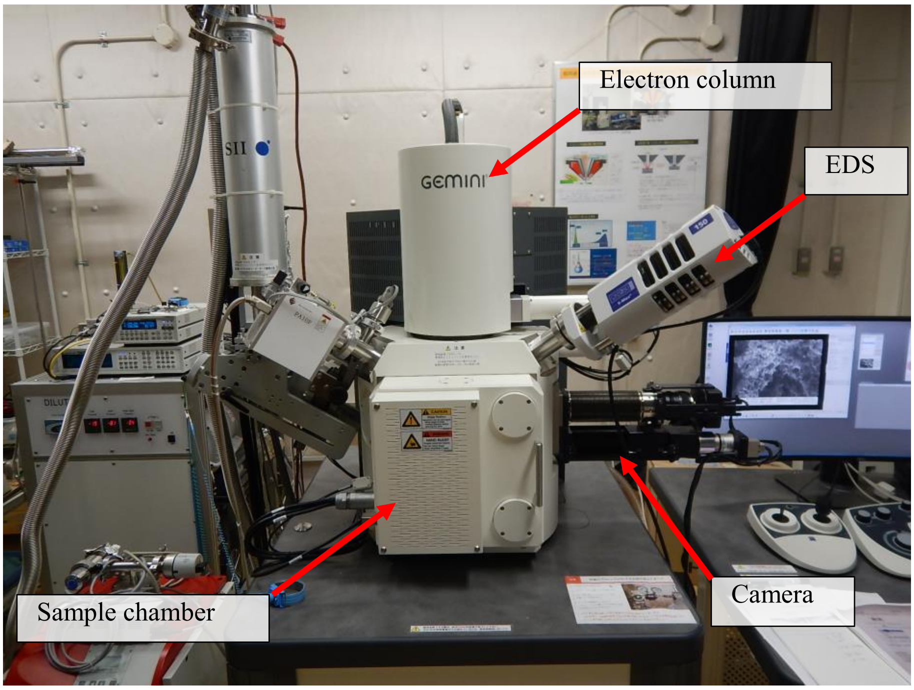

Figure 3.10 SEM and EDS apparatus

3.3 Results and Discussions

3.3.1 Geological Point of View

According to the geology map of the Miyazaki area at a scale of 1:200,000, it is evident that the Miyakonojo city area comprises various soil types. According to the visual geology map in Figure 3.11, the pumice, ash, sand, and gravel soil denoted by the light yellow symbol "Ir" are widely deposited in this area. This is the location from which the samples for analysis and mechanical tests are extracted. This deposit is an Ito pyroclastic flow underlain by the Osumi pumice fall that was formed during the Late Pleistocene period in the Quaternary era. Upon examining this map, it can be seen that there is the presence of multiple faults and thrusts in the nearby region of this area.

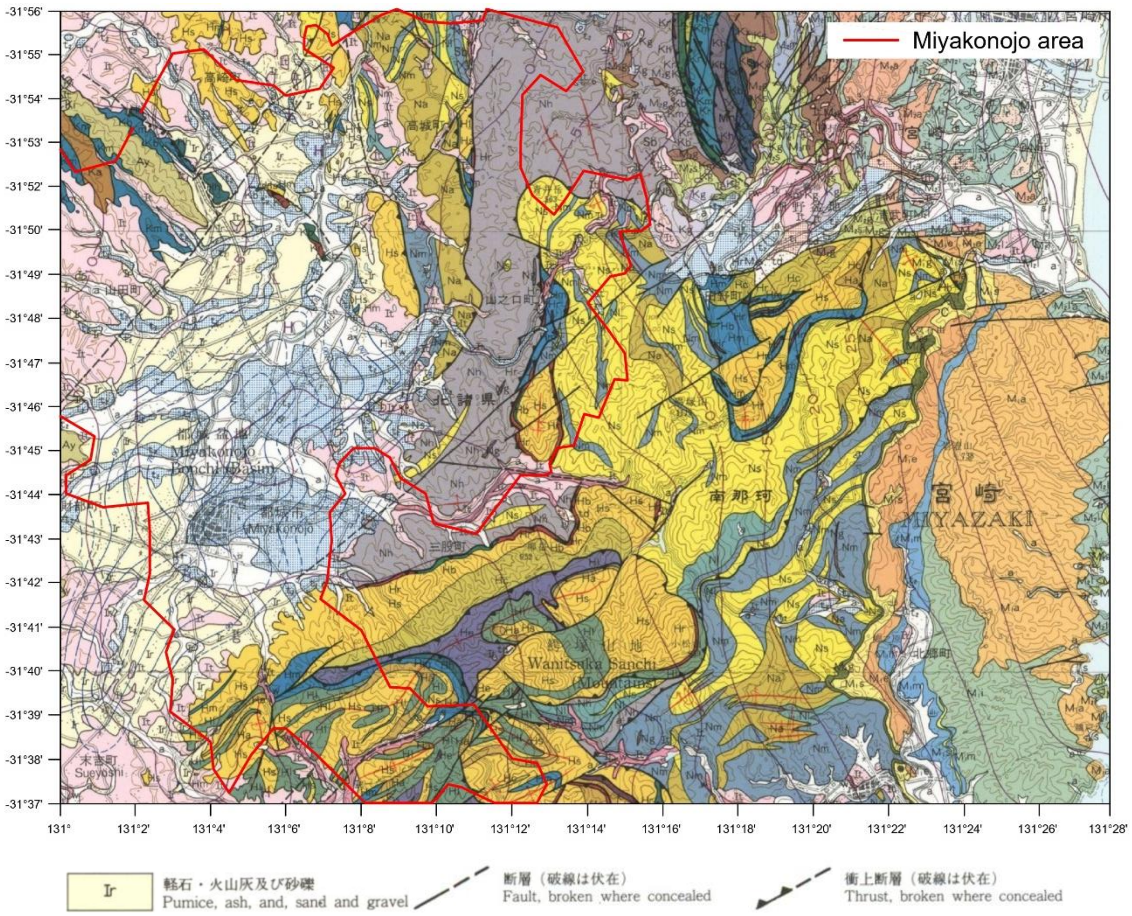

Figure 3.11 Geology map of Miyakonojo area

3.3.2 Physical Properties of Pumice

Table 3.1 shows the test results of the particle size distribution. The results of particle size distribution are compared with the liquefaction potential determined by Tsuchida (1970) in Figure 3.12, this comparison reveals that the size distribution of pumice belonged to the possibility of a liquefaction zone. D_{60}, the diameter of 60% passing material, D_{30}, the diameter of 30% passing material, and D_{10}, the diameter of 10% passing material, of pumice are used to characterize of pumice particle size category. Based on this calculation, we obtained the U_u value of 2.93, which was classified as poorly graded (*P*) where U_u < 10, and $U_c{}'$ value of 1.33. Based on the JGS 0051-2009 standard about the method of classification of geomaterials for engineering purposes, the results can be categorized as a fine fraction <5% and a gravel fraction <5% belonging to the sand poorly graded (*SP*) category. Table 3.2 is the summary of the physical properties of pumice.

Table 3.1 Particle size distribution

Diameter (mm)	Percent finer (%)
9.50	100
4.75	100
2.00	96.17
0.850	29.71
0.425	10.07
0.250	7.71
0.106	6.77
0.075	6.48
0.0536	4.32
0.03801	4.32
0.02424	3.55
0.01419	2.28
0.01006	2.03
0.00719	1.02
0.00361	0.51
0.00148	0

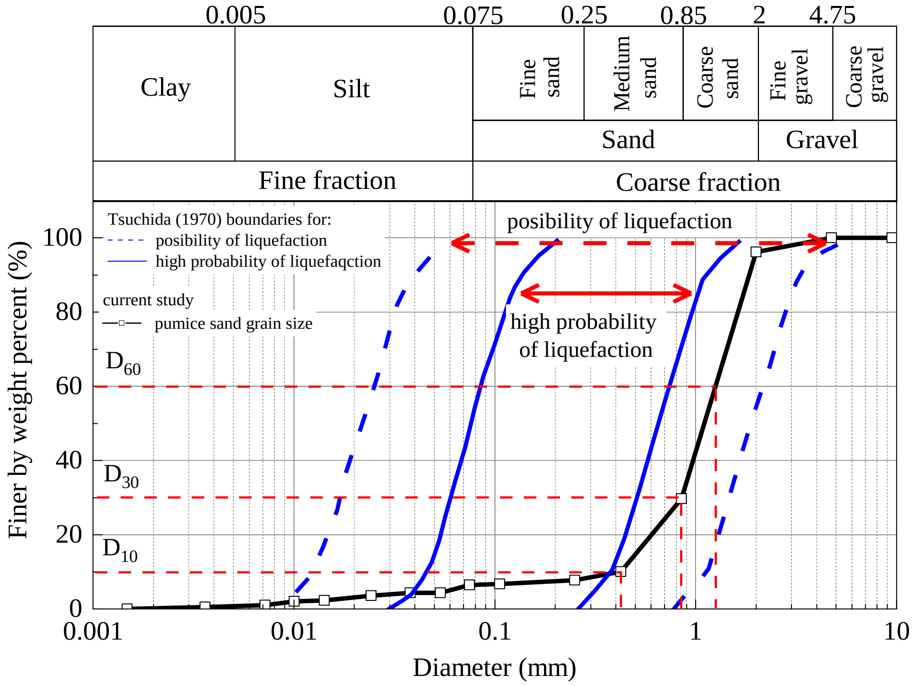

Figure 3.12 Particle size distribution comparison

Table 3.2 Physical properties of pumice

Soil properties	Pumice
Specific gravity, G_S	2.537
Soil classification	*SP*
Maximum density, γ_{max} (gr/cm^3)	1.006
Minimum density, γ_{min} (gr/cm^3)	0.824
Maximum void ratio, e_{max}	2.079
Minimum void ratio, e_{min}	1.523

3.3.3 Microstructural Characteristic

Figure 3.13 shows the SEM results of white pumice prior to single-particle strength testing. It can be demonstrated that the pumice has pores throughout its structure, it is suggested that the presence of these pores results in the crushability of the pumice. Figure 3.14 shows the result of SEM for black sand, it can be seen that black sand does not have any pores. Since the amount of black sand in the sample is small, it can be assumed that the samples represent the characteristics of pumice.

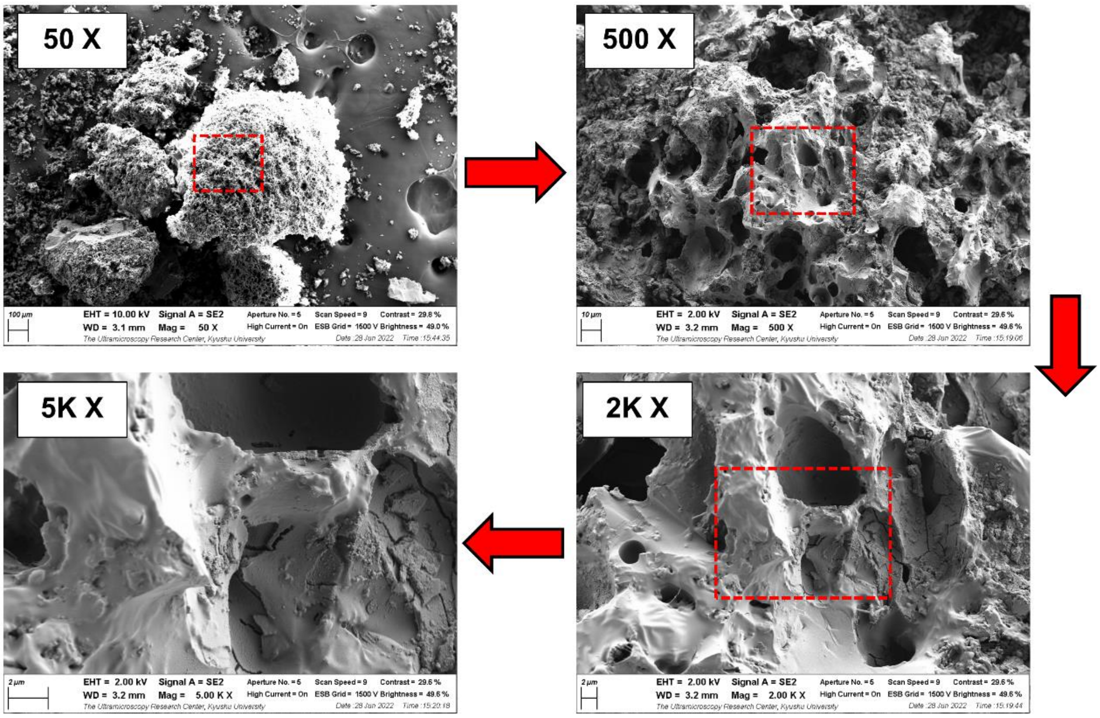

Figure 3.13. SEM results for white pumice

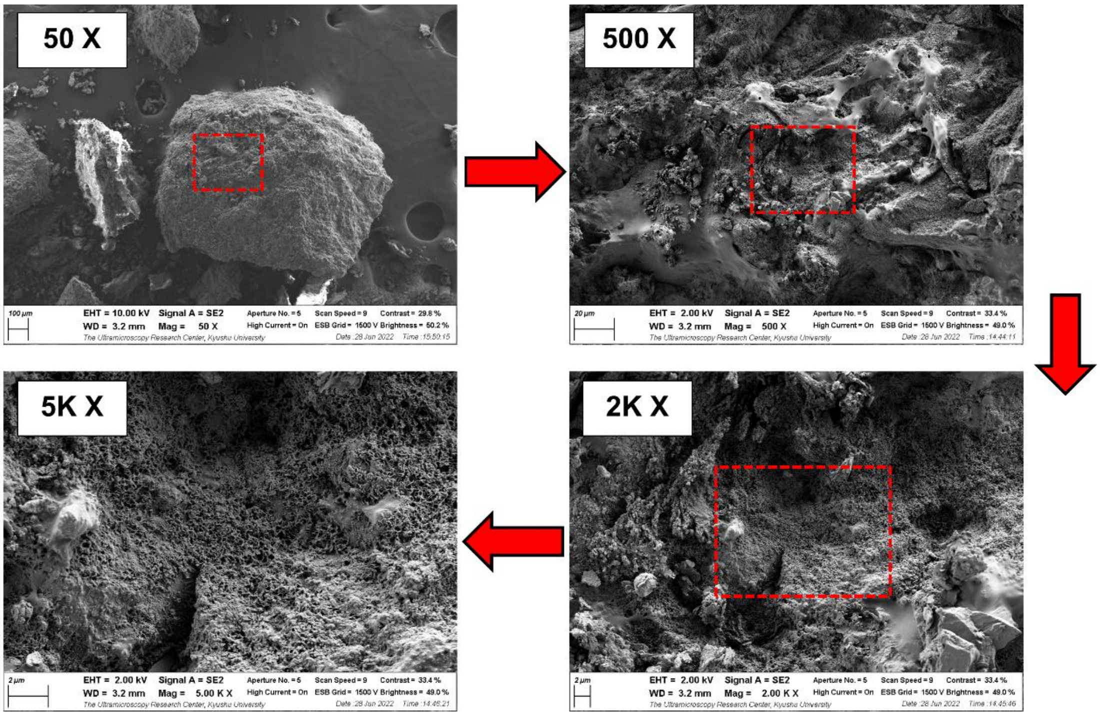

Figure 3.14. SEM results for black sand

3.3.4 Chemical Characteristic

The XRF analysis reveals that pumice consists of silica (Si) at a concentration of 56.5% followed by alumina (Al) at 16.8% and iron (Fe) at 11.2%. Additionally, there are other components present in smaller quantities, such as Calcium (Ca) and potassium (K), as well as various other chemical components, as depicted in Figure 3.15.

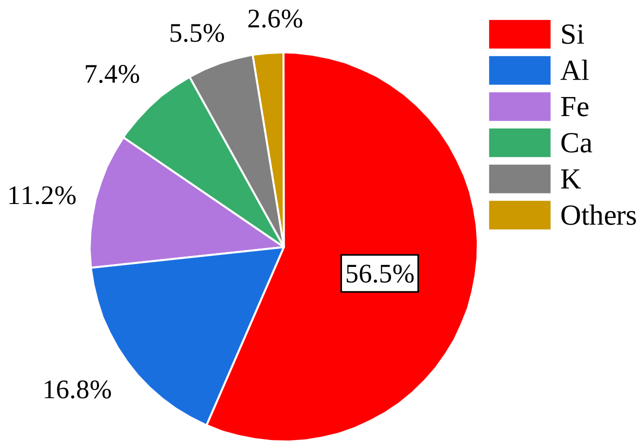

Figure 3.15. Chemical components from the XRF test (Basoka et al., 2023)

Along with SEM testing, EDS analysis is used to further examine the chemical components of pumice. This involves selecting specific chemical components on the material surfaces for analysis. Figure 3.16(a) shows the EDS data observation points on the surface of the white pumice. In Figure 3.16(b), the EDS data observation points for the black sand are shown. The result of EDS analysis is shown in Figure 3.17. Figure 3.17 (a) presents a comparison of the chemical components of white pumice, the analysis reveals that oxygen (O) is the predominant chemical component, with a proportion of 61.13%. Silica (Si) follows with a proportion of 21.7%, while aluminum (Al) constitutes 7.4%. Additionally, other minerals such as calcium (Ca) and iron (Fe) are present in smaller amounts. Figure 3.17(b) provides an overview of the chemical components of black sand. The EDS analysis reveals similar findings for pumice, with oxygen (O) being the predominant chemical component at 72.7%, Silica (Si) accounts for the proportion at 6.4%, while aluminum (Al) with 9.9%, Additionally, there are other minerals present, including manganese (Mn) and iron (Fe). This aligns with the results of prior research, which indicated that pumice primarily consists of silica (SiO_2) and alumina (Al_2O_3) minerals (Kobayashi et al., 1991; Mboya et al., 2011).

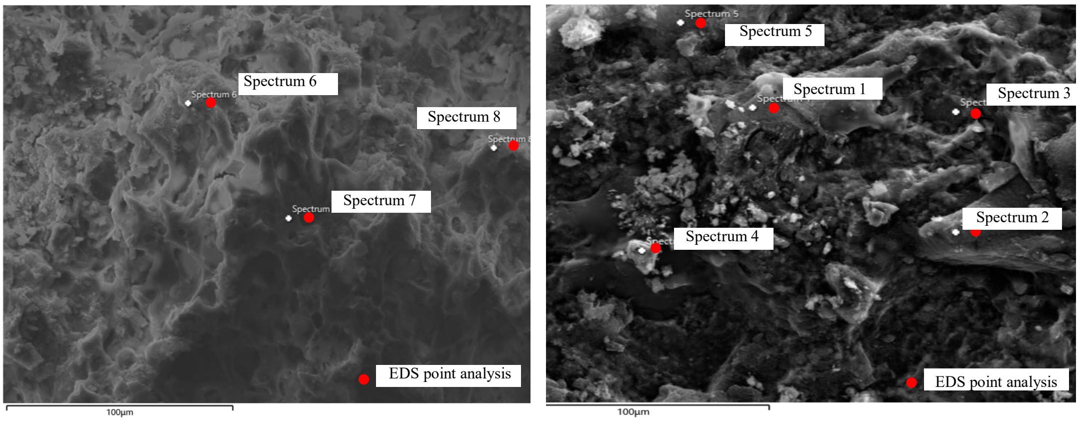

(a) white pumice (b) black sand

Figure 3.16. EDS sampling points

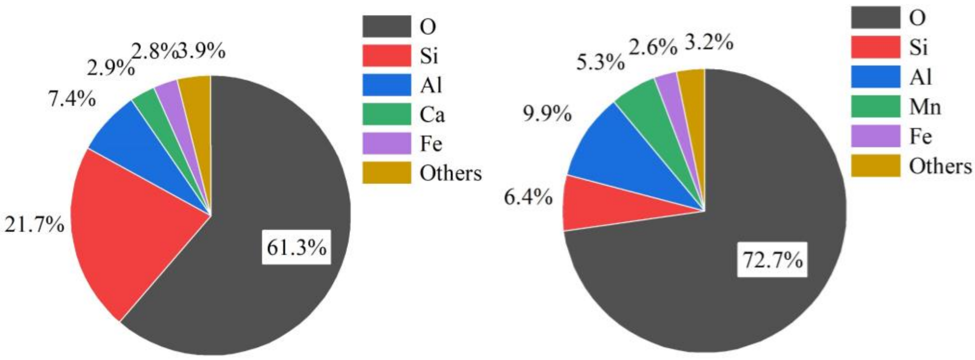

(a) white pumice (b) black sand

Figure 3.17. Chemical components from EDS test

3.3.5 Mineral Characteristic

The XRD test was performed to ascertain the mineral components of the pumice. The mineral components of the pumice were subsequently analyzed using the PXDL2 software, and the results can be found in Table 3.3. When analyzing the mineral components of pumice, it is needed to determine its chemical components based on the results of XRF and EDS analyses. The results of XRF and EDS analyses are used as an initial reference to select the candidate mineral and chemical component for pumice. The quantity of mineral components can be determined through the application of the whole powder pattern fitting (WPPF) method. XRD testing reveals that the predominant mineral components in pumice are quartz (SiO_2) with 66.7% (with a figure of merit of 0.914) and cristobalite-alpha (SiO_2) with 33.3% (with a figure of merit of 1.482). Both minerals share the same chemical components SiO_2, while both have distinct crystalline structures (Gibson & Lafemina, 1996; Tang et al., 2015). If we compare it with the mineral components of standard Toyoura sand, we can see that the main minerals of Toyoura sand are 75% quartz, 22% feldspar, and 3% magnetite (Oda et al., 1978). These mineral components between pumice and Toyoura sand are similar in that quartz is the main mineral component.

Table 3.3 Mineral composition of pumice

Mineral name	Formula	Figure of merit	Content (%)
Quartz	SiO_2	0.914	66.70
Cristobalite-alpha	SiO_2	1.482	33.30

3.4 Summary

The fundamental properties of pumice can be summarized below.

1. The pumice used in this study is from the Ito pyroclastic flow under the Osumi pumice fall, formed during the Late Pleistocene period.
2. The pumice material is classified as a poorly graded sand (*SP*) based on its physical properties, and it also has the potential to undergo liquefaction based on the standard of use in Japan.
3. Based on the result of Scanning electron microscopy (SEM) analysis, it is shown that there are pores in pumice particles that might cause crushable particles.
4. Based on the result of chemical and mineral component analysis such as XRF and XRD analysis, the pumice chemical components are primarily composed of silica (Si) 21.7%, aluminum (Al) 7.40%, oxygen (O) 61.13%, and the rest are other chemical components. The main mineral components of the pumice are quartz (SiO_2) 66.70% and cristobalite-alpha (SiO_2) 33.30%.

References

Basoka, I. W. A., Kasama, K., Furukawa, Z., Yasufuku, N., & Rifa'i, A. (2023). Microscopy and Mechanical Behavior of Pumice Single Particle. In Z. Hossain (Ed.), The 13th International Conference on Geotechnique, Construction Materials and Environment, GEOMATE 2023 (pp. 120–126). The GEOMATE International Society.

Faris, F., & Fawu, W. (2014). Investigation of the initiation mechanism of an earthquake-induced landslide during rainfall: a case study of the Tandikat landslide, West Sumatra, Indonesia. Geoenvironmental Disasters, 1(4).

Gibson, A. S., & Lafemina, J. P. (1996). Structure of Mineral Surfaces. In P. V. Brady (Ed.), Physics and Chemistry of Mineral Surfaces (Vol. 1). CRC Press. https://doi.org/10.1201/9781003068945

Hazarika, H., Sumartini, W. O., Kokusho, T., Kochi, Y., Ishibashi, S., Yamamoto, S., & Matsumoto, D. (2019). Investigation on mechanism of landslides during the 2016 Kumamoto earthquake, Japan. Earthquake Geotechnical Engineering for Protection and Development of Environment and Construction, 821–832.

Kameda, J., Kamiya, H., Masumoto, H., Morisaki, T., Hiratsuka, T., & Inaoi, C. (2019). Fluidized landslides triggered by the liquefaction of subsurface volcanic deposits during the 2018 Iburi–Tobu earthquake, Hokkaido. Scientific Reports, 9(1). https://doi.org/10.1038/s41598-019-48820-y

Kasama, K., Furukawa, Z., & Hu, L. (2021). Practical reliability analysis for earthquake-induced 3D landslide using stochastic response surface method. Computers and Geotechnics, 137, 104303. https://doi.org/10.1016/j.compgeo.2021.104303

Kobayashi, M., Kuroda, R., Suzuki, K., & Fukao, Y. (1991). Models for the Origin of the Pumice Associated with the 1989 Submarine Eruption Off-Ito, Central Honshu, Japan. J. Phys. Earth, 39, 21–26.

Lee, R. H. (1995). Coatings and alternatives for SEM microscopy.

Mboya, H. A., Makunza, J., & Mwishwa, Y. H. B. (2011). Assessment of Pumice Blocks in Comparison to Cement Sand Blocks and Burnt Blocks 'The Case of Mbeya City - Tanzania.' Journal of Civil Engineering Research and Practice, 8(1), 43–55. https://doi.org/10.4314/jcerp.v8i1.69524

Nishimura, I., Noguchi, T., Ono, Y., & Kohno, M. (2022). Subsurface structures based on microtremor observations in landslide area of Tandikat, West Sumatra, Indonesia. International Journal of GEOMATE, 22(90), 57–62. https://doi.org/10.21660/2022.90.gxi282

Oda, M., Koishikawa, I., & Higuchi, T. (1978). Experimental Study of Anisotropic Shear Strength of Sand by Plane Strain Test. Soils and Foundations, 18(1), 25–38. https://doi.org/https://doi.org/10.3208/sandf1972.18.25

Sumartini, W. O., Hazarika, H., Kokusho, T., Ishibashi, S., Matsumoto, D., & Chaudhary, B. (2018). Deformation and Failure Characteristics of Volcanic Soil at Landslides Site due to the 2016 Kumamoto Earthquake. International Association of Lowland Technology, 19(4), 237–244.

Tang, C., Zhu, J., Li, Z., Zhu, R., Zhou, Q., Wei, J., He, H., & Tao, Q. (2015). Surface chemistry and reactivity of SiO2 polymorphs: A comparative study on α-quartz and α-cristobalite. Applied Surface Science, 355, 1161–1167. https://doi.org/https://doi.org/ 10.1016/j.apsusc.2015.07.214

Tsuchida, H. (1970). Prediction and Countermeasure against liquefaction in sand deposit. *Abstract of the Seminar of the Port and Harbour Research Institute*, 3.1-3.33.

CHAPTER IV
MECHANICAL PROPERTIES OF SINGLE PUMICE PARTICLE

4.1 Introduction

According to the explanation in the previous chapter, the pumice exhibits a porous structure and is primarily composed of silica, which is susceptible to crushing under applied loads. In order to understand the behavior of pumice particles comprehensively, it is essential to examine the fundamental characteristics of pumice particles considering the existence of pores in pumice particles. The main goal of the single-particle strength test is to measure the mechanical strength of the single pumice particle and evaluate the effect of a single-particle strength on the strength behaviors of pumice as an assembly of pumice particle under a specific load (Liburkin et al., 2015; Liu et al., 2021).

Several researchers used single-particle strength tests and other tests to observe the mechanical behavior of crushable material. Orense et al. (2016) carried out SEM tests, X-ray CT image tests, single-particle strength tests, and monotonic/cyclic undrained triaxial tests to understand the characteristics of New Zealand-sourced pumice. They indicated that the single-particle strength of pumice is inferior to that of silica sand. Kasama et al. (2021) found that during the preliminary investigation, there was a suspicion that a layer of pumice had the potential to become a slip surface for Takanodai landslides caused by the 2016 Kumamoto earthquake. In this study, a single-particle strength test, cyclic box shear test, and numerical modeling were conducted. According to the study, pumice has a lower single-particle strength than those of general silica sands such as Toyoura sand. Sumartini et al. (2018) performed the SEM test, chemical component test used XRD and XRF, and cyclic undrained triaxial test at the same location as Kasama et al. (2021). This study observed the effect of pumice liquefaction on earthquakes. In addition, Kikkawa et al. (2013) conducted research that compared the geotechnical properties of pumice from the Osumi Peninsula in southern Kyushu, Japan, and New Zealand. The tests conducted included the drain triaxial test and sieve analysis. These studies demonstrated that the characteristics of the materials were highly comparable in physical properties of pumice, despite their distinct origins and variations in particle size distributions. Also, during the drained triaxial test particle crushing was considerable for pumice.

This research employed the hierarchical Bayesian approach, which is more adept at handling intricate models and hierarchical structures compared to frequentist approach to investigate single-particle pumice strength comprehensively. This chapter will examine the mechanical properties of single pumice particles through the single-particle strength test. Additionally, the correlation among single-particle strength of pumice, particle size, roughness, and aspect ratio will be discussed in this chapter. In addition, the microstructure change of pumice particles before and after the single-particle strength test was observed

4.2 Sample Preparation and Methodology

4.2.1 Material

The particle size of the pumice for a single-particle strength test is shown in Table 3.1. The particle size distribution test reveals that 96.17% of the pumice was retained on the 2.000 mm sieve, 29.71% retained on the 0.850 mm sieve, and 10.07% retained on the 0.425 mm sieve. Subsequently, three particle size groups were categorized as the large (L) sample (retained at 2.000 mm), medium (M) sample (retained at 0.850 mm), and small (S) sample (retained at 0.425 mm). According to Table 4.1 and Figure 4.1, a total of 135 particles were tested.

Table 4.1 Sample for single-particle strength test

Sample name	Retained sieve size (mm)	Total test number of
L sample	2.000	45
M sample	0.850	45
S sample	0.425	45

Before a single-particle strength test, the diameter, length, width, perimeter, and area were measured and calculated. Figure 4.1 shows a typical pumice particle for a single-particle strength test.

Figure 4.1 Single pumice particle for single-particle strength test

4.2.2 Single-Particle Strength Test

The testing apparatus was prepared with several components, such as a load cell, displacement gauge using a linear variable differential transformer (LVDT), lightning, apparatus control, data logger, and computer, as shown in Figure 4.2. A single pumice particle was positioned on a flat plate as shown in Figure 4.3. The load cell used had a maximum capacity of 100 N with a precision of 0.0001 N. The precision of the displacement gauge using LVDT was 0.005 mm. After preparing the sample, the load cell, LVDT, and the instrument were set to zero using a data logger application on a computer. The compression rate was 0.50 mm per minute. A data logger recorded the load cell and LVDT.

4.2.3 Weibull Distribution

The Weibull distribution is a widely recognized probability distribution extensively used across various fields of study. Since the 1970s, it has garnered significant attention due to its straightforwardness and adaptability (Lai, 2014). The Weibull distribution is widely acknowledged as a lifetime distribution in various fields, such as reliability engineering, and has been extensively referenced in geotechnical engineering to examine failure phenomena.

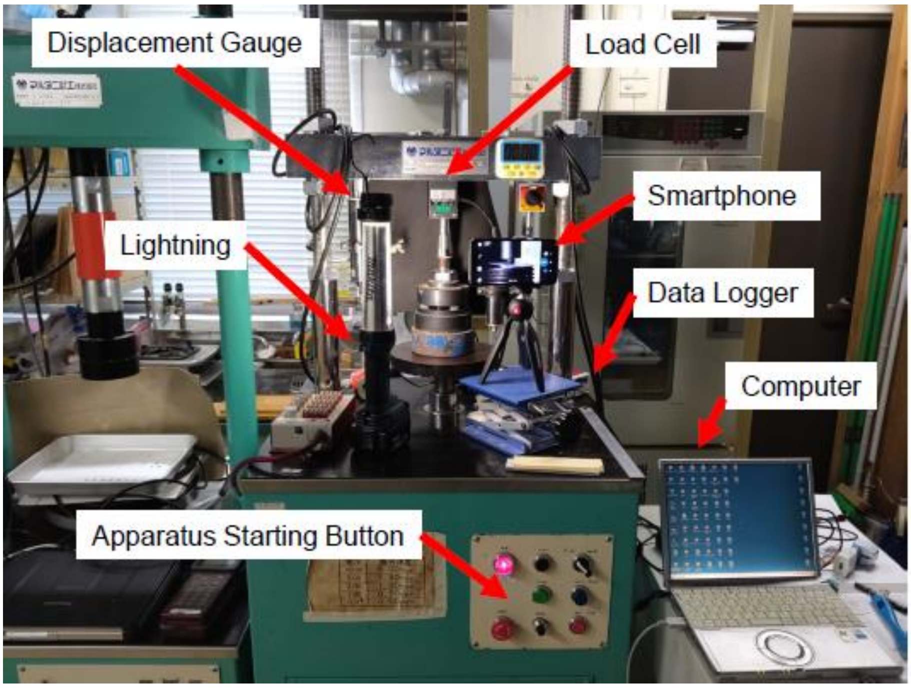

Figure 4.2 Single-particle strength test apparatus


Figure 4.3 Single-particle strength test

Several researchers have already used the Weibull distribution function to evaluate the failure of geomaterial, McDowell & Amon (2000) and Nakata et al. (2001) studied the utilization of the Weibull distribution to understand the mechanism of soil particle failure. Their findings offer substantiation for the applicability of the Weibull distribution in assessing the tensile strength of soil particles, and this validates the utilization of the Weibull distribution as a tool in the examination of the crushability of soil particles. In addition, Zhou et al. (2015) employed the Weibull distribution function for modeling progressive failure processes of slopes on the numerical analysis. Jamei et al. (2011) conducted an accurate forecast of the alterations in the particle size distribution of the crushed material, utilizing Weibull statistics. Jamei et al. (2011) also stated an alternative approach is to utilize the renowned Weibull model, which has gained extensive usage in the analysis of brittle materials. Through statistical analysis, Jansen & Stoyan (2000) showed that the particle sizes affect the Weibull parameter. Nevertheless, to maintain the assumption of a Weibull parameter that remains constant depending on the material, they suggested considering particles of varying sizes made of the same material.

Recent studies confirm the utility of Weibull as a tool for examining particle failure in the field of geotechnical engineering. The probability density function $f(t)$ for the Weibull distribution with standard two-parameter, can be expressed as follows in Eq. 4.1 below.

$$f(t) = \left(\frac{\alpha}{\beta}\right)\left(\frac{t}{\beta}\right)^{\alpha-1} \cdot exp\left[-\left(\frac{t}{\beta}\right)^{\alpha}\right] \qquad \text{Eq. 4.1}$$

The parameter α is the shape parameter also known as the Weibull parameter as mentioned in Jiang & Murthy (2011), Lazzari (2017), Ono (2019), β is the scale parameter, and t is the time failure. The corresponding reliability function $\bar{F}(t)$ is given by Eq. 4.2 below:

$$\bar{F}(t) = exp\left[-\left(\frac{t}{\beta}\right)^{\alpha}\right], \alpha, \beta > 0, t \geq 0 \qquad \text{Eq. 4.2}$$

4.2.4 Bayesian Inference Approach

Figure 4.4 shows the flow chart of the Bayesian inference approach. The first step is to assume the mean mu_a and mu_b for shape (α) and scale (β) parameters in the Weibull distribution indicating a normal distribution. Both variables are subsequently used as inputs for the likelihood function. Ultimately, the posterior was calculated using the aforementioned steps. Afterward, the aforementioned procedure was repeated, and the specimens were amplified using Markov Chain Monte Carlo (MCMC) until a total of 2000 iterations were acquired.

The hierarchical approach was created by combining the sub-models, and the inclusion of all existing uncertainty and the integration of the components is achieved by employing the Bayesian theorem. The hierarchical approach is a widely used method for solving problems in which observable results are modeled by incorporating specific parameters that are probabilistically determined using hyperparameters. Hierarchical thinking is essential for comprehending intricate problems that involve multiple parameters and plays a crucial role in developing computational methodologies (Albert & Hu, 2019; Gelman et al., 2021).

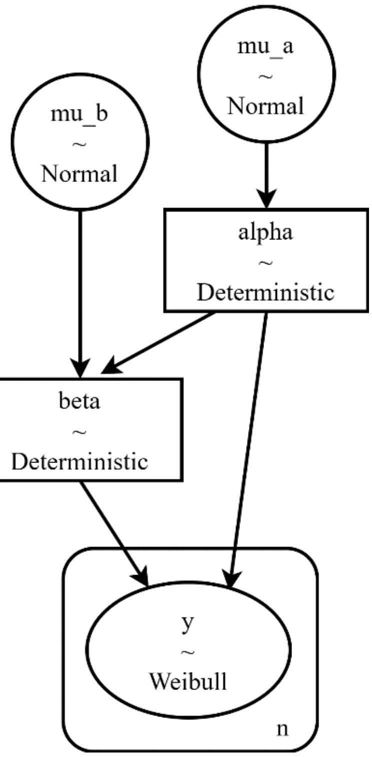

Figure 4.4 Flow chart of Bayesian inference approach (Basoka, et al., 2023a)

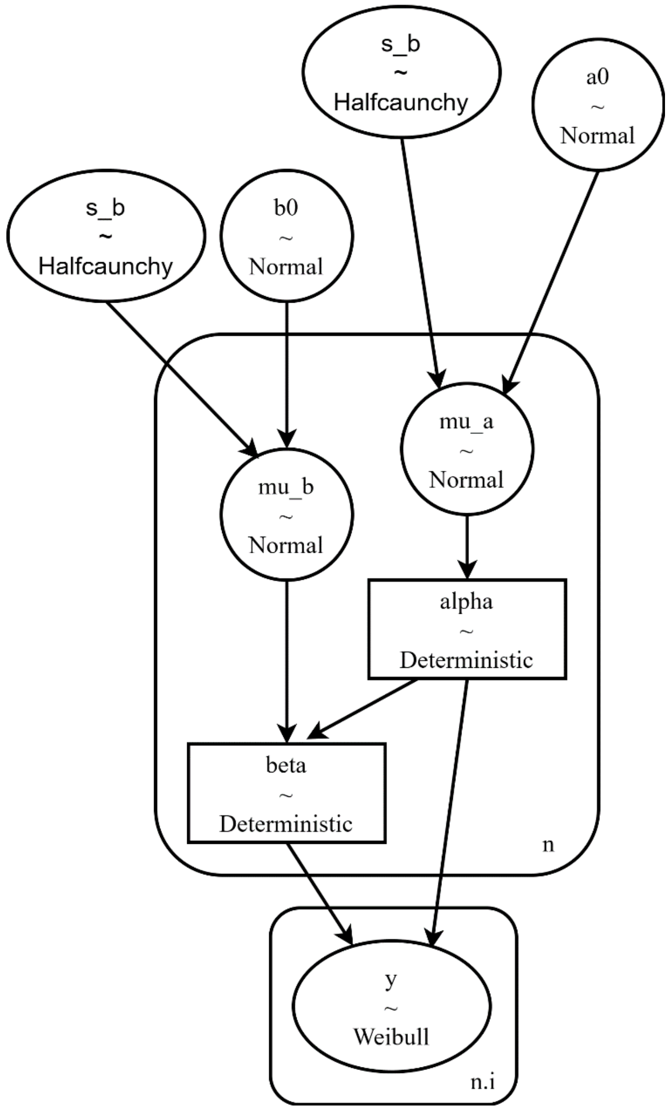

Figure 4.5 Flow chart of Hierarchical Bayesian inference approach (Basoka, et al., 2023a)

Figure 4.5 shows a flow chart for hierarchical Bayesian approach. This model closely resembles the conventional Bayesian inference approach, with the inclusion of additional hyperparameters: s_a (standard deviation for mu_a), b0 (mean for mu_a), s_b (standard deviation for mu_b), and b0 (mean for mu_b). In the previous data section, random variables and observation parameters were utilized for analysis. Subsequently, the posterior is computed by taking into account the quantity of data and the various data groups. The proposed approach entails analyzing the Weibull parameters for each sample group (S, M, and L), in order to understand how sample size affects these parameters the analysis was conducted sequentially on 15, 30, 45, 60, 75, 90, 105, 110, and 135 samples.

The acquired outcomes will be compared with frequentist inference in order to assess any observed alterations. A Bayesian library named PyMC in the Python environment is utilized to analyze the Bayesian approach.

4.3 Results and Discussions

4.3.1 Single-Particle Strength Test Results

Figure 4.6 illustrates a typical test result obtained from a single-particle strength test indicating a striking resemblance to a jigsaw pattern. Based on the result of the single-particle strength test depicted in Figure 4.6, the initial peak observed in the test was regarded as a single-particle strength. Figure 4.7(a) displays the relationships between single-particle strength and particle size while Figure 4.7(b) presents a histogram of all single-particle strengths.

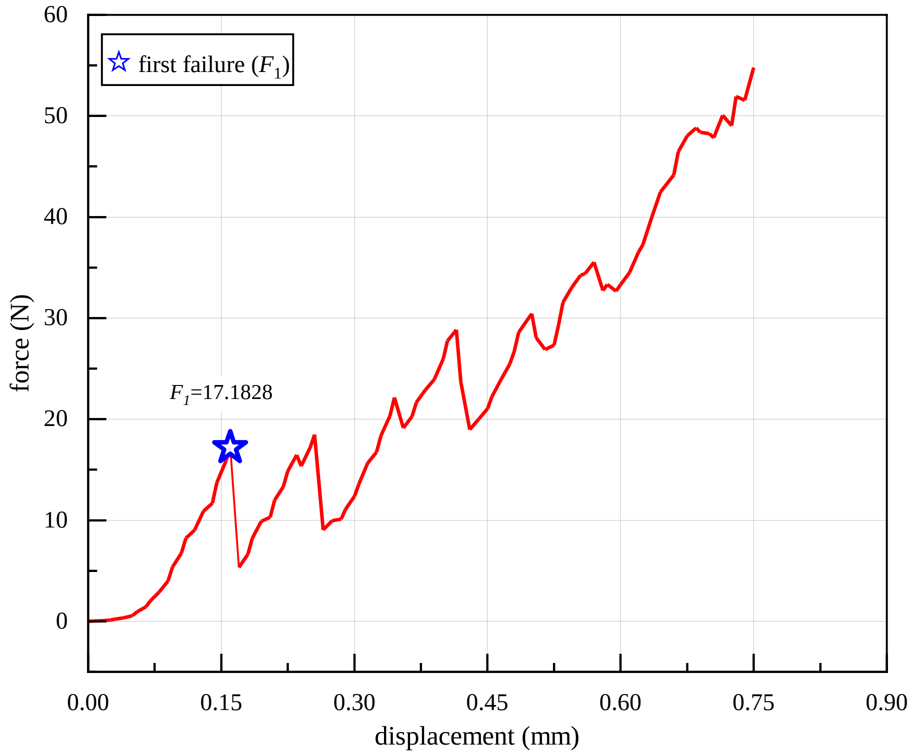

Figure 4.6 Typical test result of single-particle strength

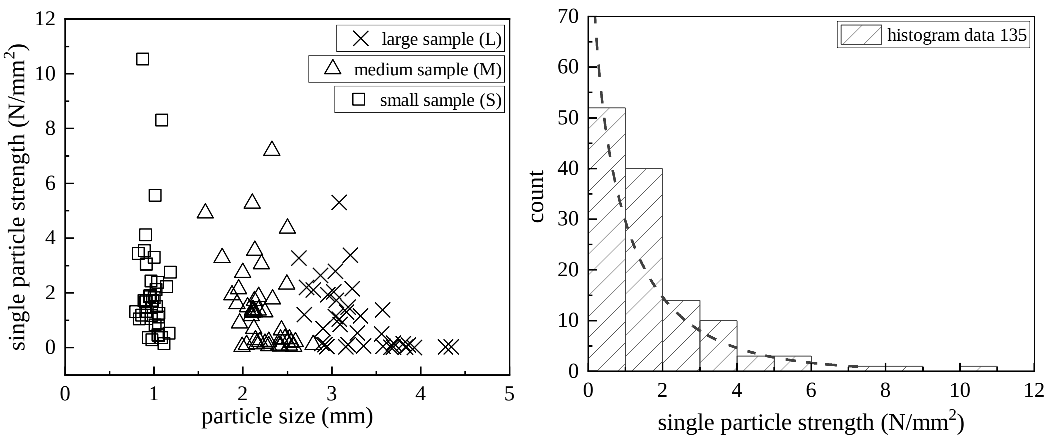

(a) (b)

Figure 4.7 Single-particle strength test result

4.3.2 Particle Behavior Based on Linear Fitting

In order to evaluate the sample number dependency on Weibull distribution to express the single-particle strength of pumice, Figure 4.8(a) depicts a single-particle strength of pumice for randomly selected 15 samples. During this examination, we analyzed three distinct categories of samples: small (S sample), medium (M sample), and large (L sample). Overall, upon examining the entire dataset, it was evident that there was a clear downward trend in the abundance of pumice. As the particle size increases, the single-particle strength decreases. However, when we used the conventional frequentist approach, we observed that the S sample and M sample show a decreasing trend, consistent with the overall data trend. In contrast, the L sample shows a flat correlation and a tendency to increase, which is contrary to the results seen in the S sample and M sample. This is due to the luck of sample number for conventional frequentist analysis. Consequently, a small sample size results in an inaccurate estimation.

The hierarchical Bayesian approach demonstrates excellent performance in analyzing a small dataset, as depicted in Figure 4.8(a). The blue dashed line represents the outcome of linear regression fitting using the hierarchical Bayesian approach, and the red line is linear regression fitting using conventional frequentists. According to this approach, considering the sample group for the entire dataset yields improved outcomes. Specifically, the data from the L sample exhibits a similar trend to the S sample and M sample dataset, which is similar to the experimental findings of previous researchers obtained from single-particle strength test (Kasama et al., 2021; Kwag et al., 1999;

McDowell & Amon, 2000; Nakata et al., 2001; Orense et al., 2016; Soda et al., 2021; Yasufuku & Kwag, 1999). A comparative analysis was conducted between traditional frequentist and hierarchical Bayesian approaches using 135 sample data to provide additional evidence of the effectiveness of hierarchical Bayesian approaches within a small dataset. The results shown in Figure 4.8(b) show that, when a big dataset is used, the results from the traditional frequentist and hierarchical Bayesian approaches follow the same pattern. When comparing the outcomes of linear regression fitting on a sample size of 135, it closely resembles the pattern of linear regression fitting using hierarchical Bayesian with a sample size of only 15. Therefore, it can be inferred that employing the hierarchical Bayesian approach is highly effective in predicting data through the use of fitting regressions.

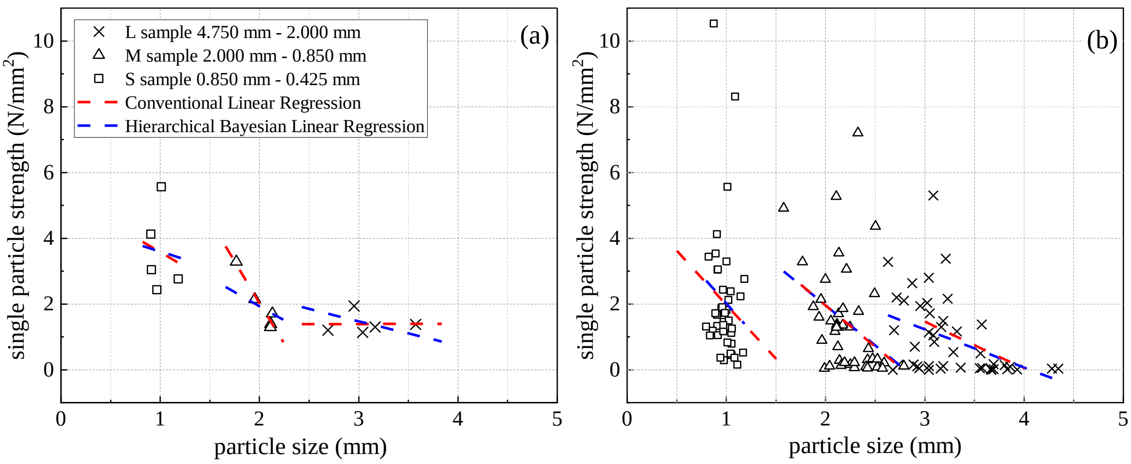

Figure 4.8 (a) Small data set (15 samples) (b) Big data set (135 samples)

4.3.3 Particle Behavior Based on Weibull Parameter.

(1) Bayesian Inference Approach

The Weibull distribution is commonly employed as a standard for examining the failure or durability of a substance. The Weibull distribution consists of two parameters, α (shape parameter) and β (scale parameter). Research conducted by Jiang & Murthy (2011) demonstrates that a Weibull shape parameter is a useful tool for characterizing product quality. They have categorized the shape parameter into three distinct groups: small, medium, and large. The determination of partition points relies on the maximum value of the Weibull shape parameter and is achieved using cluster analysis. A generalized equation has been formulated to accommodate various values of the upper threshold. The magnitude of the shape parameter and the category of failure consequences are the primary criteria for determining the reliability enhancement or maintenance approach for each component in a system. Meanwhile, the scale parameter represents the mean lifespan of the sample and affects the spread of values in the sample distribution (Yu et al., 2023).

This study aims to analyze the shape and scale Weibull parameters for the single-particle strength of pumice. The conventional frequentist, the conventional Bayesian approach, and the hierarchical Bayesian approach are utilized to analyze those parameters. The samples used in these analyses were calculated in several sample sizes from 15, 30, 45, 60, 75, 90, 105, 120, and finally 135 samples. This aims to understand the influence of the number of samples in analyzing Weibull parameters using several methods as mentioned earlier. The Bayesian approach involves determining the prior, likelihood, and posterior, as outlined in Figure 4.4 and Figure 4.5. This study presents a standard outcome of a Bayesian inference trace plot, as illustrated in Figure 4.9, Figure 4.9 specifically illustrates the results obtained from analyzing a sample size of 135. The left-hand side of Figure 4.9 exhibits the kernel density estimate (KDE) plot, which offers an estimation of the probability density function (PDF). Afterward, the right-hand side of Figure 4.9 is the Markov Chain Monte Carlo (MCMC) sampling procedure utilized to acquire 2000 samples from the posterior distribution. The consistent form of the resulting graph suggests that the MCMC sampling method produces a fairly precise interpretation with no divergence of data. Figure 4.10 illustrates a comparison between conventional frequentist and Bayesian approaches for each shape and scale parameter. By examining Figure 4.10, it is clear that the blue line, the Bayesian approach demonstrates that values converge to stability at a faster rate to reach a stable value with a specific number of samples, even when they are not significant. Additionally, as the number of samples increases, the parameter values begin to stabilize and exhibit a discernible pattern, which becomes apparent at a sample size of 45 and shows a good trend from sample 90 onward.

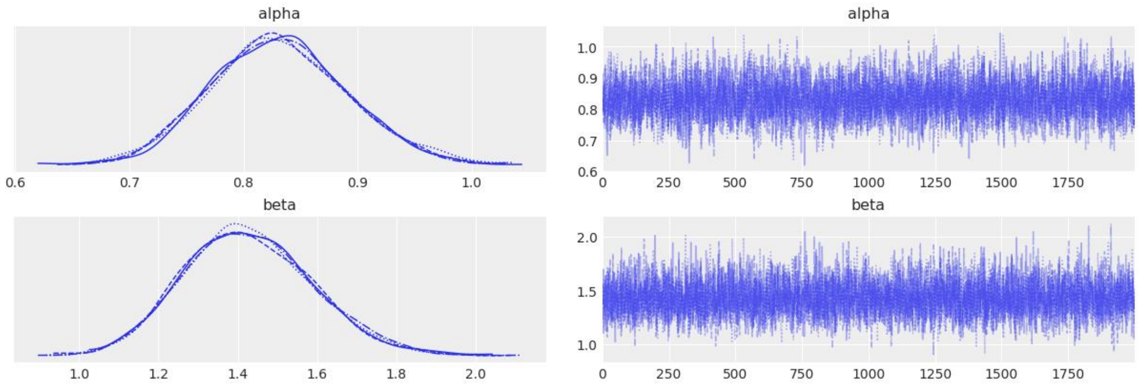

Figure 4.9 Trace plot result of Bayesian inference using 135 data set.

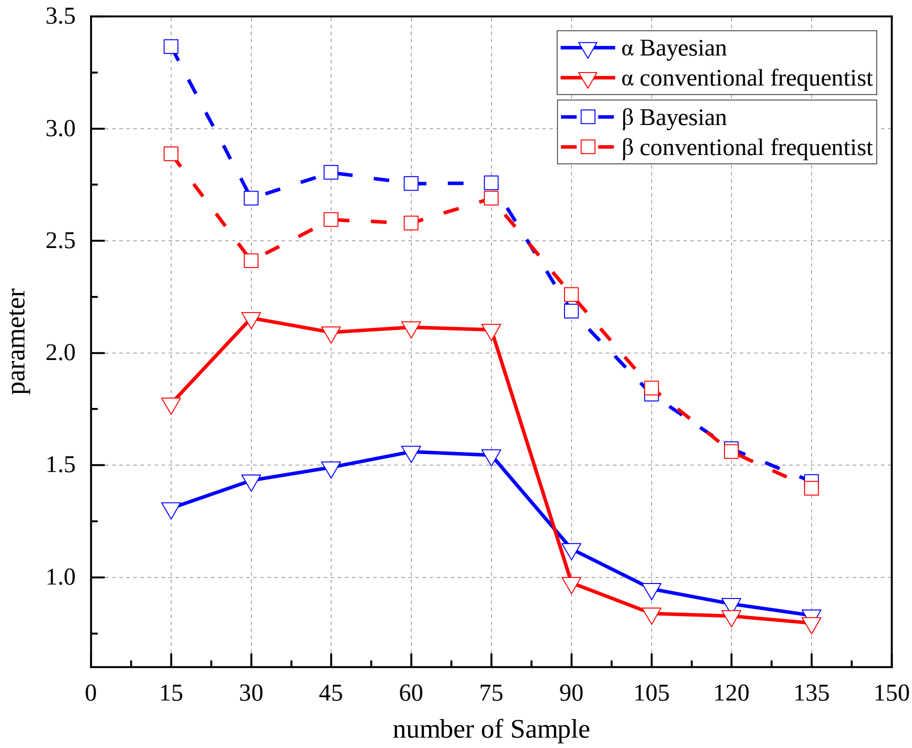

Figure 4.10 Comparison Weibull parameter

(2) Hierarchical Bayesian Inference Approach

Figure 4.11 presents the example output results of each sample group obtained from the Bayesian hierarchical approach consisting of 135 samples. The left-hand side of Figure 4.11 illustrates the configuration of the KDE curve on the parameter density function, which is divided into three sample groups such as S, M, and L depending on drain size. The colors blue, orange, and green correspond to the categories of large, medium, and small samples, respectively. The shape of the curve demonstrates a distinct correlation between the initial probability and the subsequent probability. The homogeneity of the sample graph on the right side of Figure 4.11 indicates that MCMC sampling is effective. MCMC sampling must account for divergence, and its effectiveness is diminished when a graph exhibits a bottleneck shape.

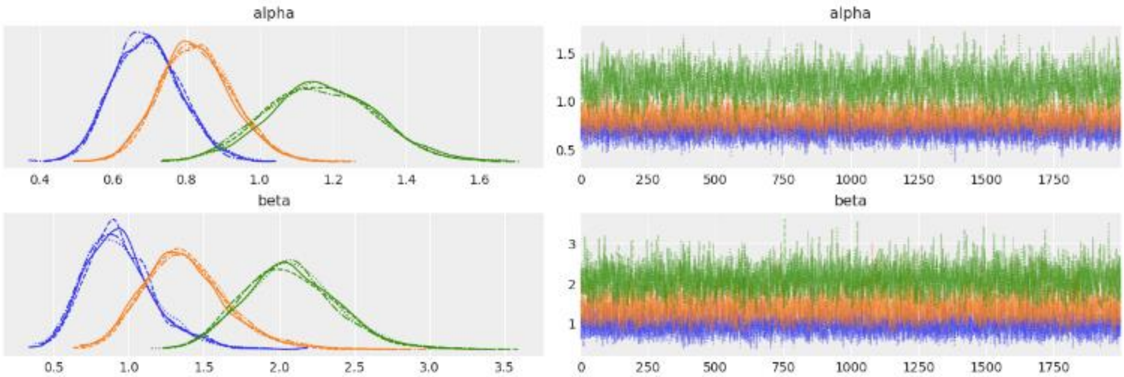

Figure 4.11 Trace plot result of group sample using hierarchical Bayesian inference based on 135 data sets.

Furthermore, this study offers a succinct analysis of the characteristics and variables of each sample group through the utilization of hierarchical Bayesian approach for group samples and conventional Bayesian inference for all samples. These comparisons are conducted for every individual sample utilized in this study, by comparing the sample counts of α and β parameters, it was found that there is a negative correlation between the size of the particles and the Weibull parameters, as depicted in Figure 4.12. Figure 4.12 (a) demonstrates that as the sample number reaches 90, the α parameter value starts to stabilize gradually, without any sudden changes, at a constant value. As the sample number approaches 90, the parameter value stabilizes at a constant level, with a less steep increase compared to when the sample number was smaller. Figure 4.12(b) shows a consistent pattern in the β parameter values across all 90 samples, which is similar to the trend observed for the α parameter.

Figure 4.13 presents a comparison of the α and β parameters for datasets that contain a minimum of 90 individual samples. The stability of the parameters increases as the sample sizes increase. The comparison shows a positive correlation between the α and β parameters, where an increase in one leads to a steady increase in the other. Figure 4.14 illustrates the correlation between the Weibull parameter and particle size. As particle size increases, the value of the Weibull parameter decreases. This implies that a lower α value (<1) indicates an increasing failure rate over time, indicating an upward trend. That suggests that the failure rate rises proportionally with the increase in particle size. The β determines the specific level of durability or size of the distribution. A reduction in the scale parameter results in a decrease in the characteristic durability. The data indicates that the L sample has a higher frequency of failure events compared to the S sample or that the L sample has a lower threshold stress required for failure compared to the S sample.

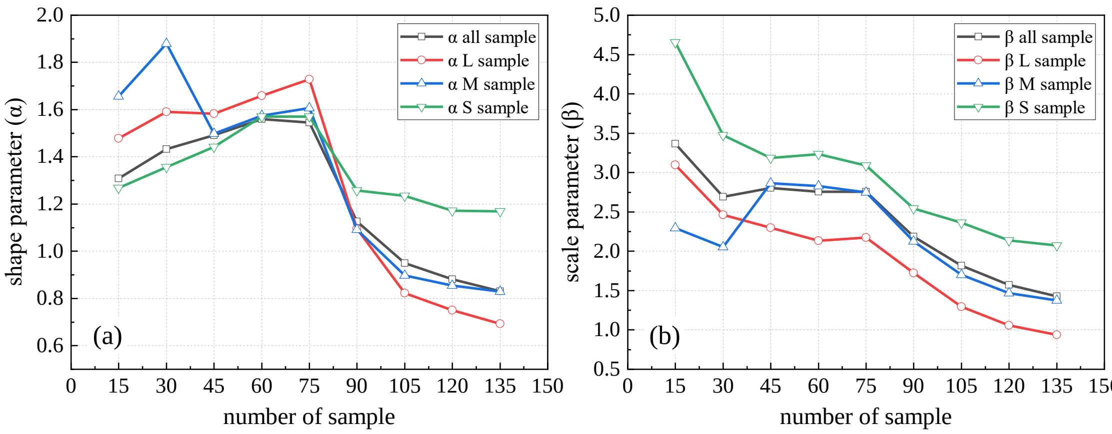

Figure 4.12 Comparison Weibull parameters using Bayesian inference approach

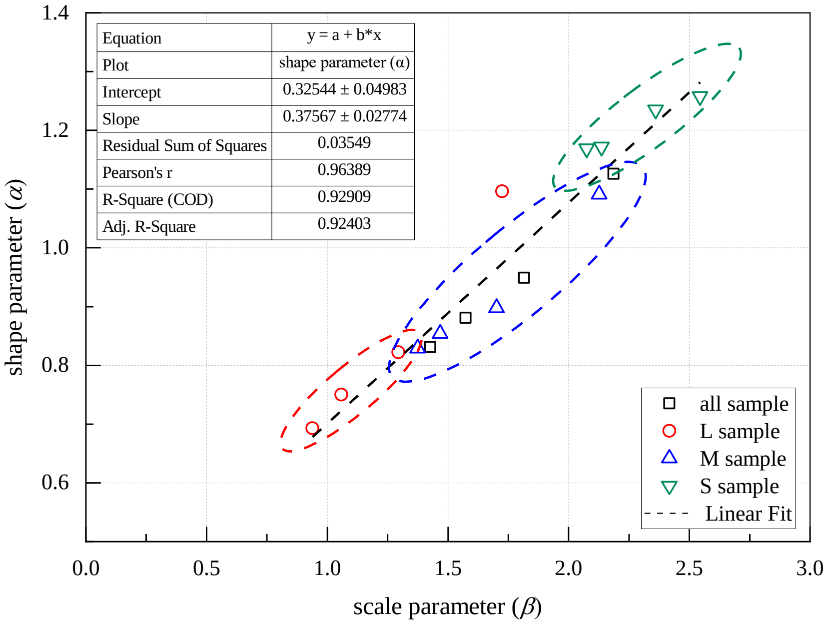

Figure 4.13 Correlation of shape parameter and scale parameter

By keeping the shape parameter constant (α = 0.5, 1.0, 1.5, and 2.0) and adjusting the scale parameter of the pumice according to the increase in the number of samples, we can observe variations in the scale parameter as the amount of data changes. Figure 4.15 depicts the conventional Bayesian approach or for a further explanation we will call it the nonhierarchical Bayesian approach, which does not consider the sample group. It is evident that the scale parameters decrease relatively as the amount of data increases. This is indicated by the decreasing trend line observed in the sample of 45. The same principle is applicable to Figure 4.16, where the hierarchical Bayesian approach is employed to examine sets of data that exhibit comparable patterns. When we reverse the process and fix the scale parameter values (β = 0.5, 1.0, 1.5, and 2.0), the shape parameter (α) also known as the Weibull parameter, does not exhibit significant variations over the increases in sample number and remains relatively constant as seen in Figure 4.21 for all sample using nonhierarchical Bayesian approach and in Figure 4.18 for group sample using hierarchical Bayesian approach. However, it is important to note that this value exhibits a relatively stable pattern when the number of samples reaches 30 to 45, which aligns with the earlier statement that a minimum of 45 samples is required to accurately depict the characteristics of the pumice.

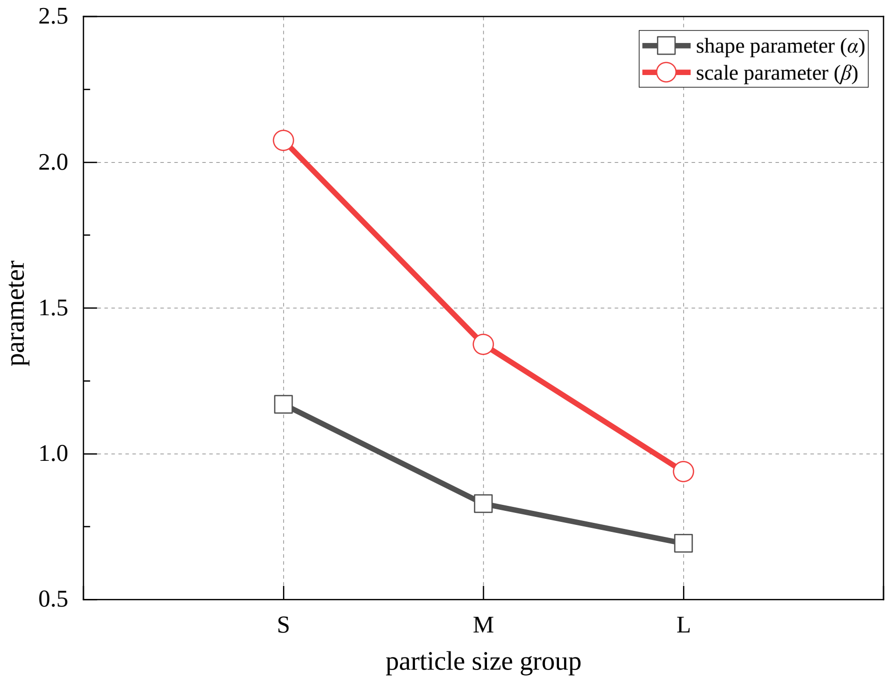

Figure 4.14 Relationship of Weibull parameter and particle size

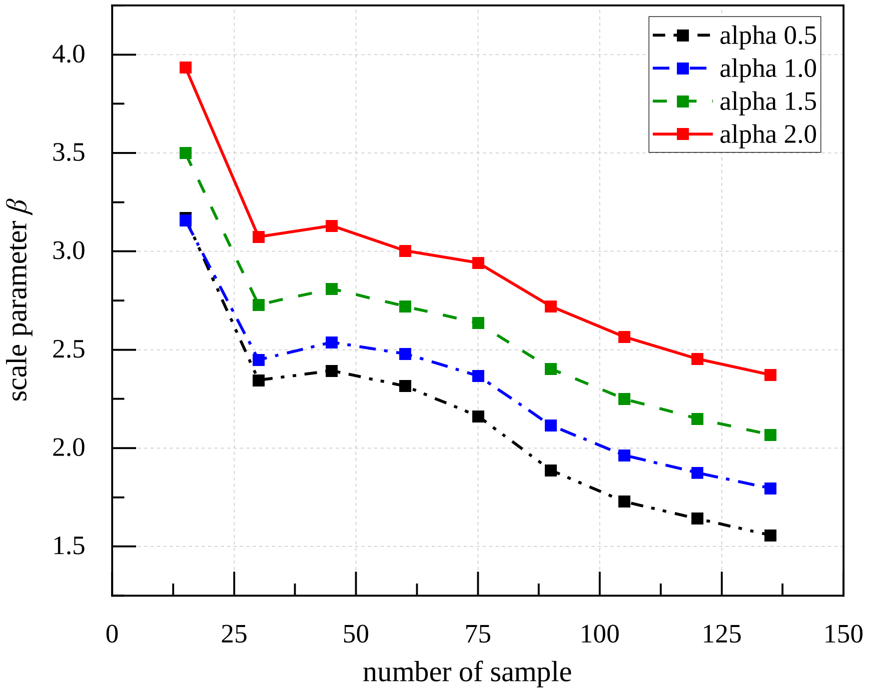

Figure 4.15 Constant α for all sample using nonhierarchical Bayesian

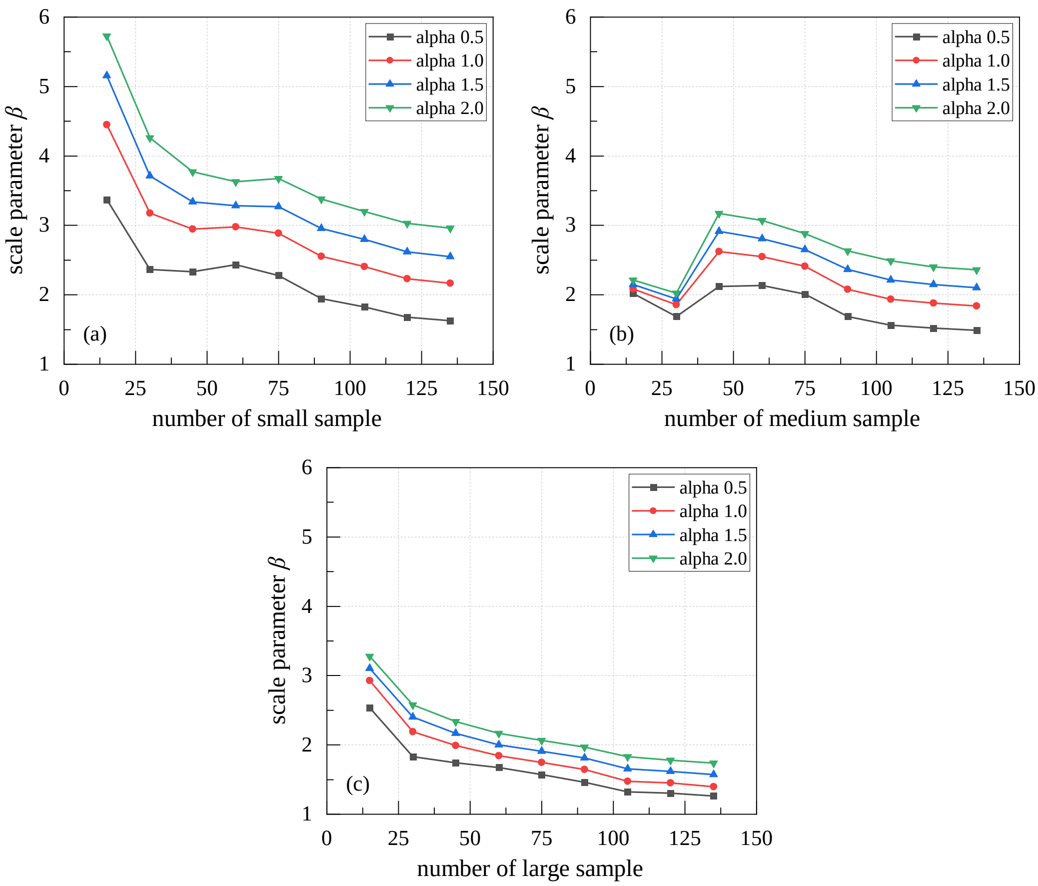

Figure 4.16 Constant α for group sample using hierarchical Bayesian

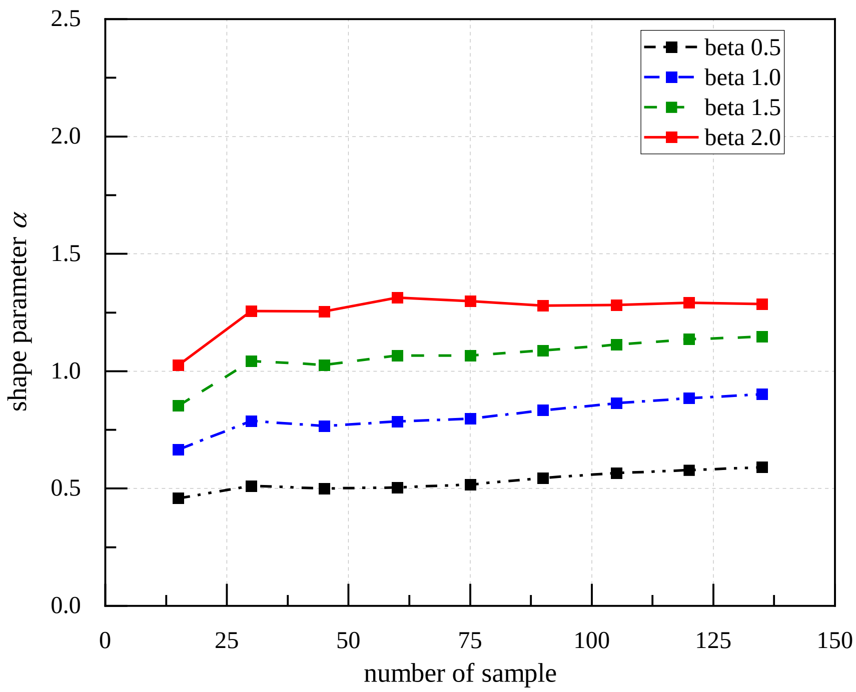

Figure 4.17 Constant β for all samples using nonhierarchical Bayesian

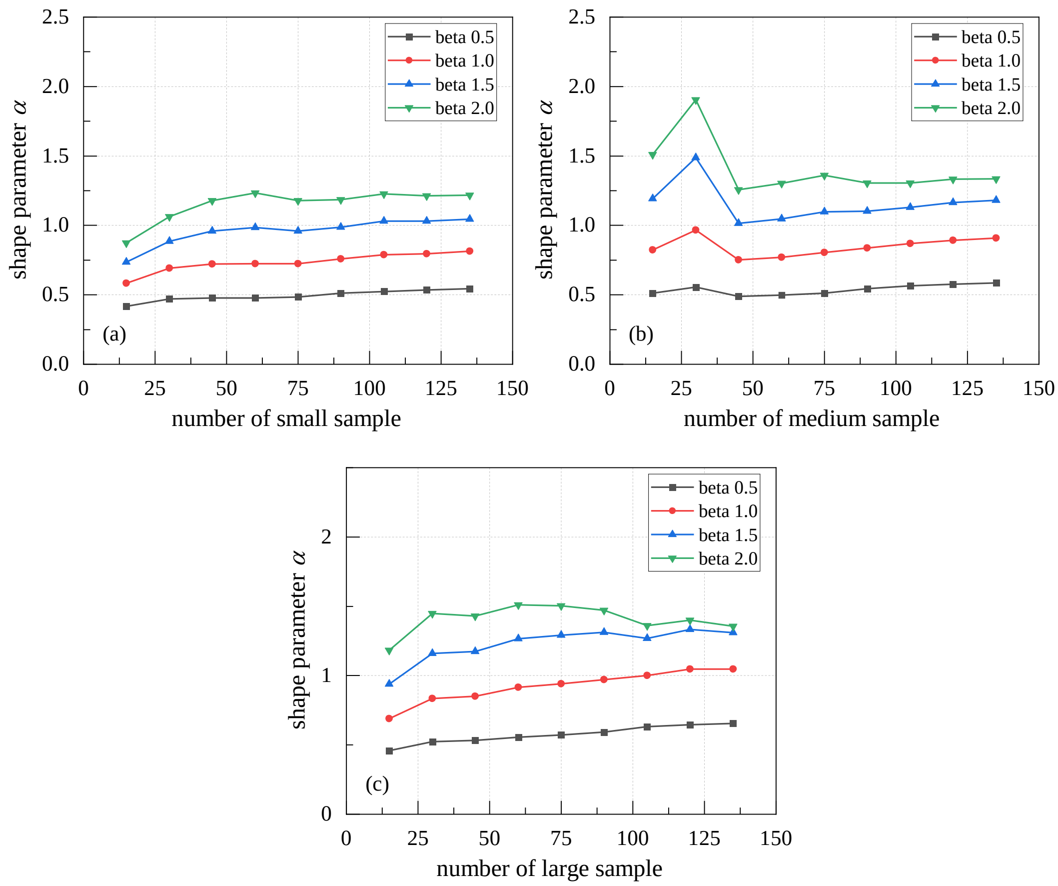

Figure 4.18 Constant β for group sample using hierarchical Bayesian

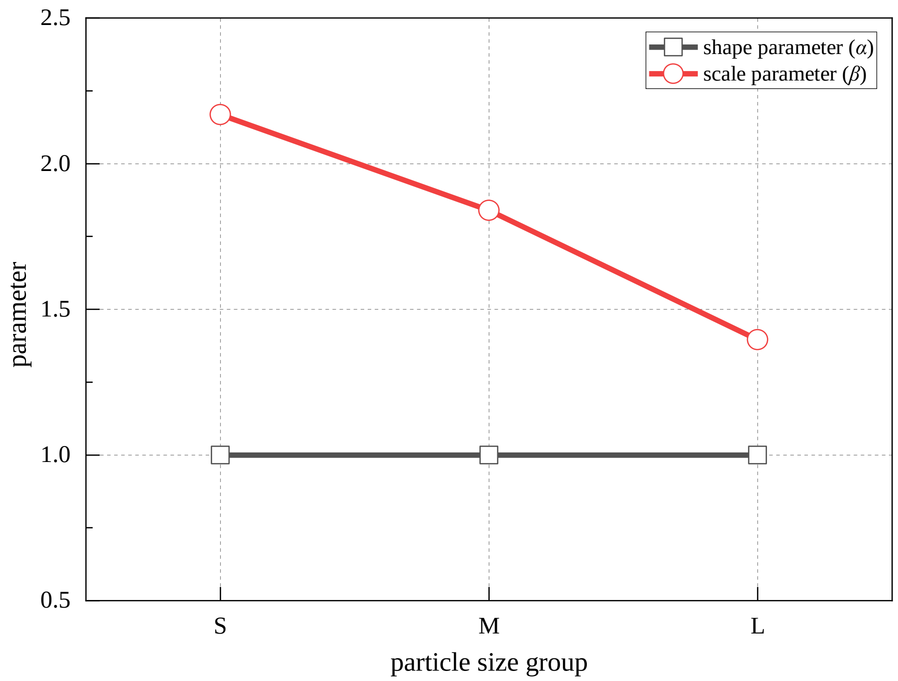

Figure 4.19 Relationship of scale parameter and particle size with constant shape parameter

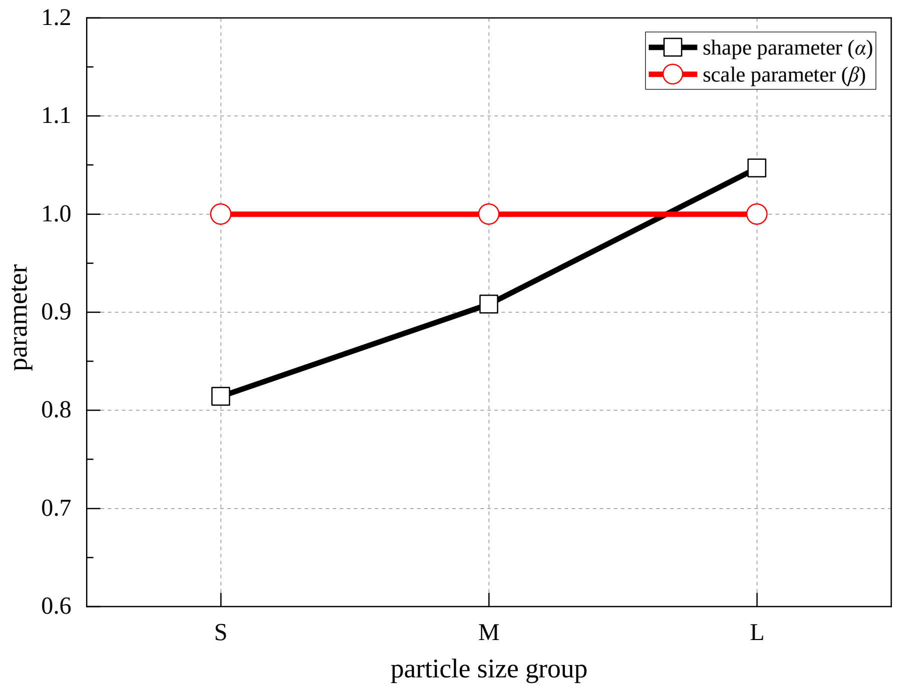

Figure 4.20 Relationship of shape parameter and particle size with constant scale parameter

Figure 4.19 and Figure 4.20 show the relationship between the parameters when one of them is held constant at a value of 1 and using 135 data results. Figure 4.19 demonstrates an inverse relationship between the scale parameter and particle size, indicating that the scale parameter decreases as the particle size increases. In contrast, Figure 4.20 illustrates a positive relationship between the shape parameter value and particle size, indicating that the shape parameter value increases as the particle size increases. As previously mentioned the shape parameter also known as the Weibull modulus is mostly described as failure criteria for crushable material. To compare the Weibull modulus of pumice with other materials, we can examine, when the scale parameter is set to 1 the shape parameter or Weibull modulus is increased within increasing the particle size as can be seen in Figure 4.20 these results are in accordance with observations made by the previous researcher by McDowell & Amon (2000) and Nakata et al. (2001). The results can be found in Table 4.2 reveals that the Weibull modulus of pumice is the lowest among other materials.

4.3.4 Particle Behavior Based on Particle Shape

In order to discuss the effects of particle shape such as the aspect ratio and roundness coefficient on the results of the single-particle strength test, Figure 4.21 shows the relationships among single-particle strength, aspect ratio, and roundness coefficient. Figure 4.21(a) indicates that the correlation between aspect ratio and single-particle strength is widely dispersed and does not exhibit a significant relationship between the two parameters. The particle roundness and the single-particle strength show a minimal correlation as depicted in Figure 4.21(b) same as Figure 4.21(a). Figure 4.22 depicts the relationship between aspect ratio and roundness. It demonstrates that the roundness coefficient increases with increasing aspect ratio.

Table 4.2 Weibull modulus from several materials

Material	Particle size (mm)	Weibull modulus	Source
Silica$_{1.4\text{-}1.7}$	1.4-1.7	3.04	(Nakata et al., 2001)
Silica$_{0.6\text{-}0.71}$	0.6-0.71	2.17	
Silica$_{0.25\text{-}0.3}$	0.25-0.3	1.82	
Toyoura	0.106-0.25	2.17	
Aio	0.85-2.0	1.93	
Masado	1.4-1.7	1.23	
Glass ballotini (G.B.)	0.85-1.0	5.9	
Angular glass (A.G.)	0.85-1.0	2.1	
Quiou sand	1	1.32	(McDowell & Amon, 2000)
	2	1.51	
	4	1.16	
	8	1.65	
	16	1.93	
Pumice$_{(S)}$	0.80-1.62	0.814	Current study
Pumice$_{(M)}$	1.57-3.30	0.908	
Pumice$_{(L)}$	2.63-5.57	1.047	

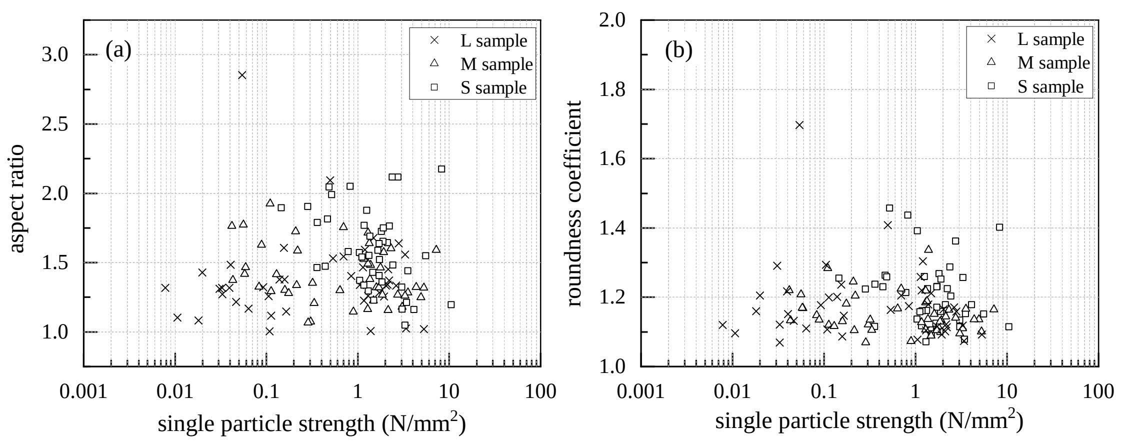

Figure 4.21 The relationship between stress, aspect ratio, and roundness coefficient

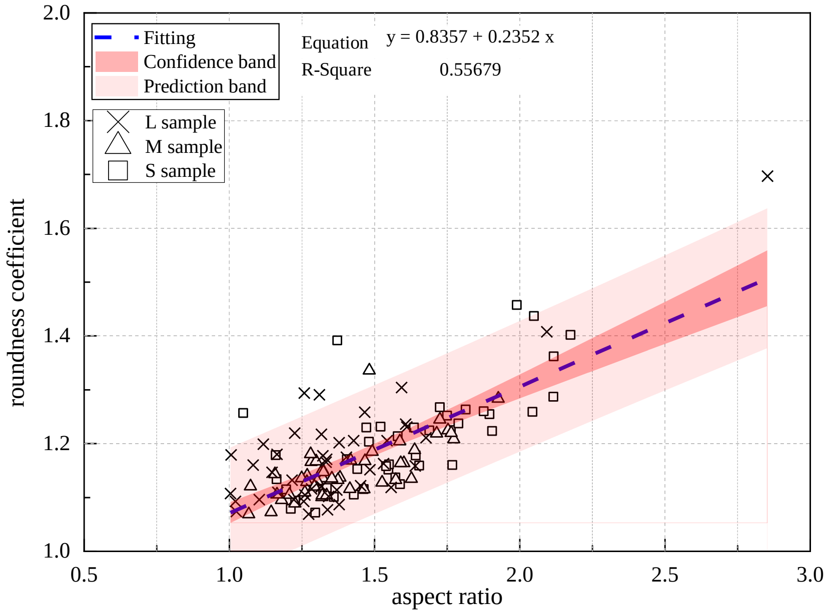

Figure 4.22 The relationship between aspect ratio and roundness coefficient

4.3.5 Microstructural Behavior of Pumice

In the examination of the microstructural changes in pumice particles, the observed particles are those that were present at the end of the single-particle strength test, as shown in Figure 4.23. Figure 4.24(a) shows the visible pores of the pumice before conducting the single-particle strength test, resembling thin layers similar to an ant nest. The red circle in Figure 4.24(b) denotes the pores of the pumice after the single-particle strength test, filled with smaller broken particles. Upon closer examination of the pumice pores depicted in Figure 4.25(a), a more distinct view of the pumice pores becomes apparent, the red dotted line in Figure 4.25(b) shows the failure of pumice pore layers. The test demonstrates that the presence of pores in the pumice has a substantial impact on its collapse behavior, resulting in a low bearing capacity.

Figure 4.26(a) demonstrates that the red-colored initial state proposed by Image J (image analysis software) revealed the existence of pores. Figure 4.26(b) shows the results of the SEM test conducted on the pumice particles after the completion of the single-particle strength test. Table 4.3 shows the outcomes of the changes in pore volume. The table demonstrates a decrease in the surface area of pores in pumice particles. In contrast, as the area decreases, the number of pores increases. This observation indicates that pores of the pumice become narrower, and small new pores form due to cracks caused by the applied pressure on the pumice.

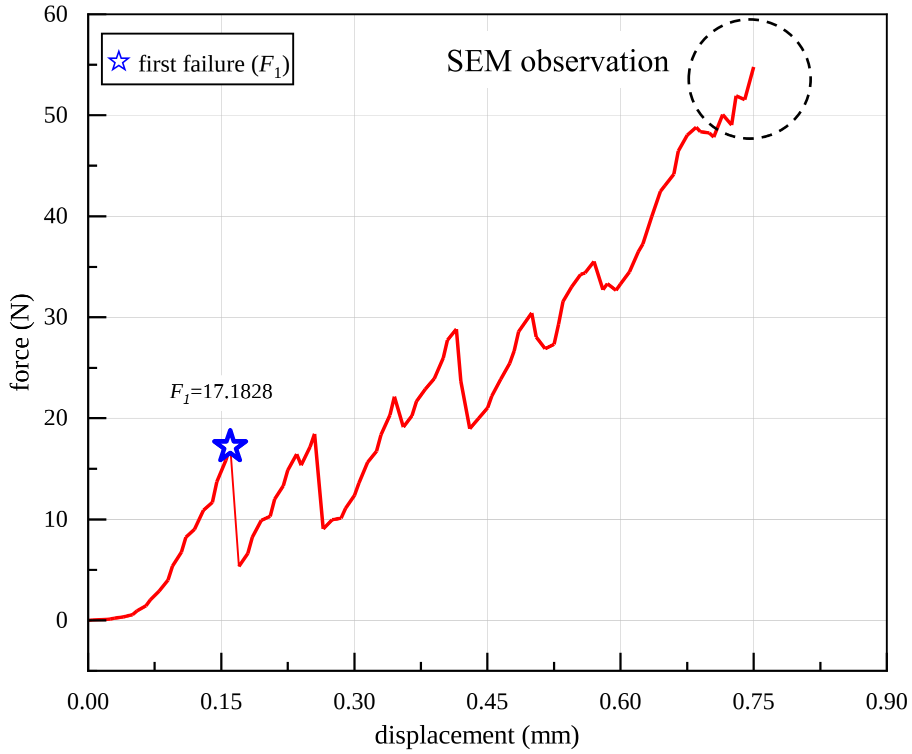

Figure 4.23 SEM observation at the end of single-particle strength test

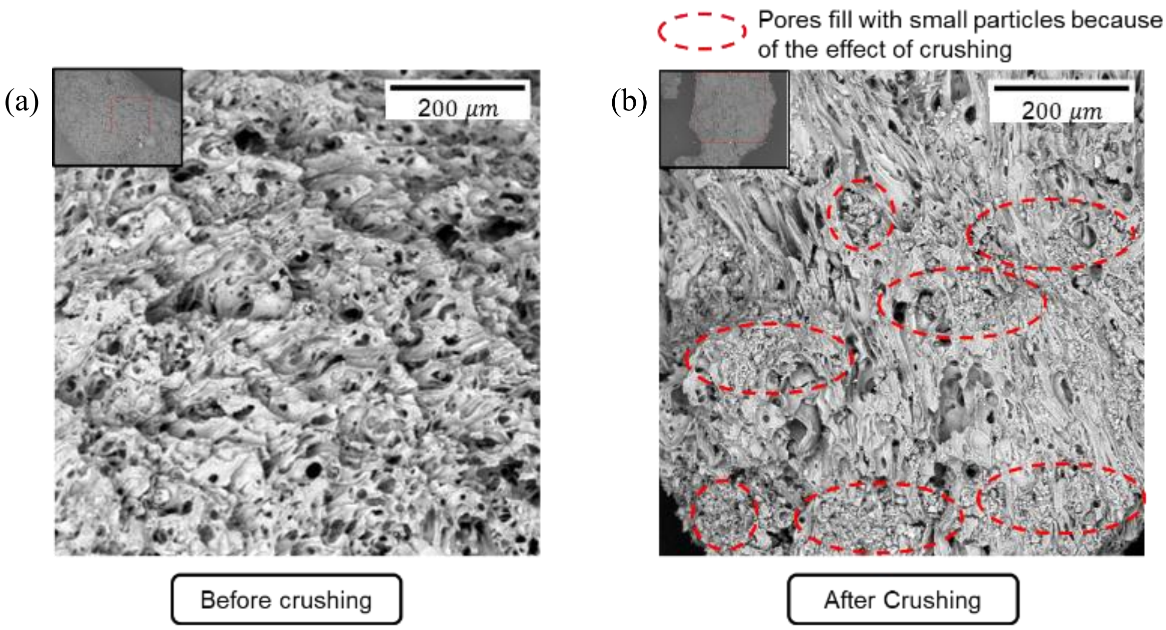

Figure 4.24 SEM results of pumice particle (Basoka, et al., 2023b)

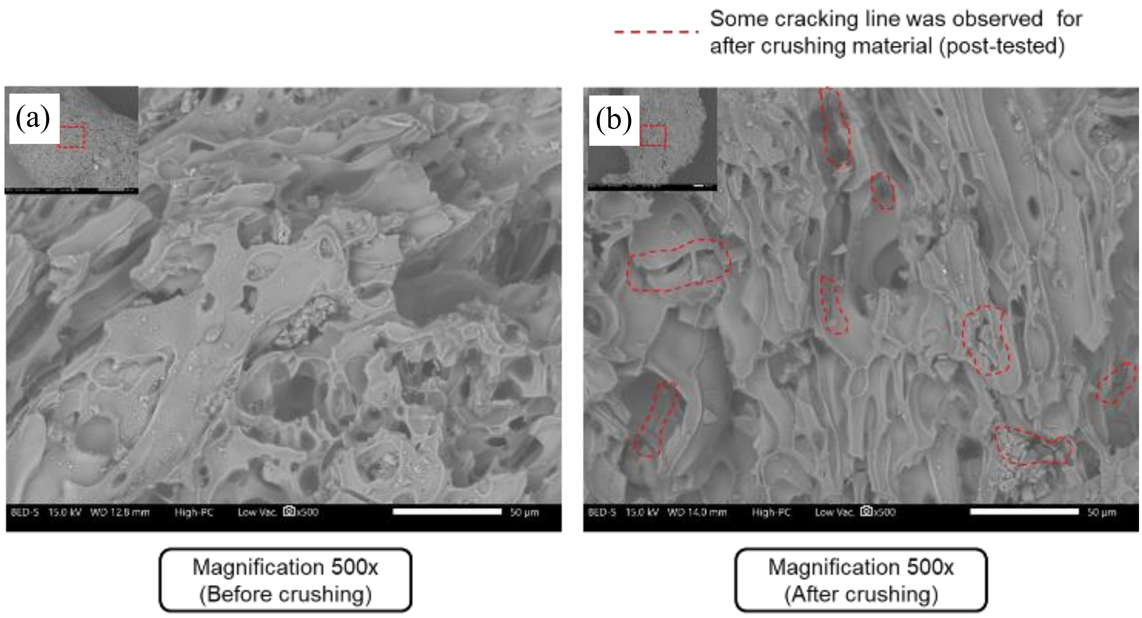

Figure 4.25 SEM results of pumice particle for crack observation (Basoka, et al., 2023b)

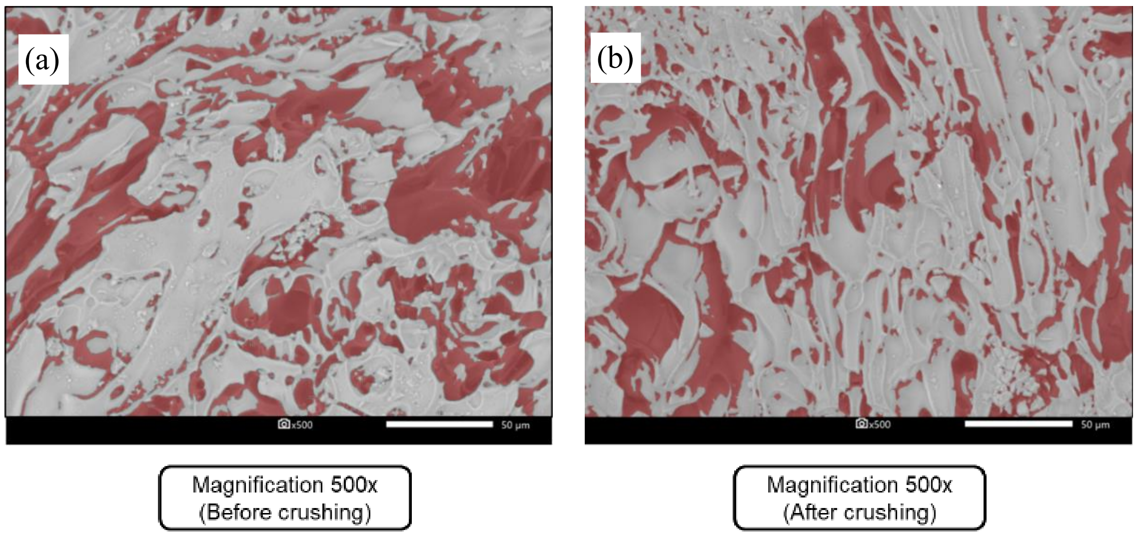

Figure 4.26 Pore of pumice particle before and after single-particle strength test (Basoka, et al., 2023b)

Table 4.3 Number of pores before and after single-particle strength test

	Before	After
Count	245	406
Total area pore (μm^2)	18569.16	14535.81
Average size total area pore (μm^2)	75.792	35.802
Area pore (%)	37.395	29.398

4.4 Summary

In this study, pumice particles were subjected to a single-particle strength test, followed by the analysis of their microstructural components using SEM. The results can be summarized as follows:

1. Based on the single-particle strength test it can be observed the strength of pumice decreases when the size of the particle is increased.
2. The frequentist and hierarchical Bayesian analyses of the linear relationship between particle size and particle stress exhibit little differences because the data set is quite high, using up to 135 samples. When the data set is small (15 data), linear fitting using the hierarchical Bayesian approach yields excellent results. In contrast, the prediction error obtained using the conventional frequentist approach on a small sample size can be corrected by employing the hierarchical Bayesian approach. This situation is further confirmed when a large data set is used. The hierarchical Bayesian approach consistently outperforms the frequentist approach in terms of prediction accuracy for the linear fitting to predict particle strength based on diameter.
3. In the last test using 135 samples, we can obtain most of the shape parameter (α) parameter result < 1, which means the sample is "decreasing failure rate" or, in other words, single-particle strength is decreased within increasing particle size.
4. The explication of the scale parameter (β) parameter describes how distributed the data is, the higher the scale parameter value, the more spread the shape of the Weibull curve.
5. The Weibull distribution parameters yield slightly dissimilar outcomes compared to those obtained through the linear fitting approach. When the sample size is small, specifically 15, both the conventional frequentist and Bayesian approach yield unsatisfactory results. However, when the sample size increases to 45, the Bayesian approach is a more balanced point between the conventional frequentist and Bayesian approach. Finally, when the sample size reaches 90, both conventional frequentist and Bayesian approaches exhibit a similar trend. It is evident that in specific situations, it is necessary to use a minimum number of samples in order to obtain accurate values.
6. The relationship between particle shape (aspect ratio and roundness coefficient) and particle strength does not exhibit a significant correlation. The data distribution

demonstrates this, showing no tendency for particle strength to increase or decrease under the influence of particle shape.

7 The aspect ratio and roundness coefficient exhibit a positive correlation. An increase in aspect ratio with increasing roundness coefficient similar to those of typical crushable soils.

8 Following the single-particle strength test, microstructural analysis observations using SEM on the pumice particles reveal a reduction in the pore area, while the number of pores increases as a result of particle crushing.

References

Albert, J., & Hu, J. (2019). Probability and Bayesian Modeling (1st ed.). Chapman and Hall/CRC. https://doi.org/https://doi.org/10.1201/9781351030144

Basoka, I. W. A., Kasama, K., Furukawa, Z., & Rifa'i, A. (2023a). Bayesian hierarchical model on crushability of pumice particle strength. Geotechnics for Sustainable Infrastructure Development - Geotec Hanoi., Vietnam.

Basoka, I. W. A., Kasama, K., & Furukawa, Z. (2023b). Crushability Effect of Pumice Pore Size. Annual Reports of The Ultramicroscopy Research Center Kyushu University, No. 47, Fukuoka, Japan, August 2023

Basoka, I. W. A., Kasama, K., Furukawa, Z., Yasufuku, N., & Rifa'i, A. (2024). The Physical and Mechanical Properties of Single Pumice Sand Particle. GEOMATE Journal, 26(115), 73–80. https://geomatejournal.com/geomate/article/view/4497

Gelman, A., Carlin, J. B., Stern, H. S., Dunson, D. B., Vehtari, A., Rubin, D. B., Carlin, J., Stern, H., Rubin, D., & Dunson, D. (2021). Bayesian Data Analysis (3rd ed.).

Jamei, M., Guiras, H., Chtourou, Y., Kallel, A., Romero, E., & Georgopoulos, I. (2011). Water retention properties of perlite as a material with crushable soft particles. Engineering Geology, 122(3), 261–271. https://doi.org/https://doi.org/10.1016/j.enggeo.2011.06.005

Jansen, U., & Stoyan, D. (2000). On the validity of the Weibull failure model for brittle particles. Granular Matter, 2(4), 165–170. https://doi.org/10.1007/s100350000052

Jiang, R., & Murthy, D. N. P. (2011). A study of Weibull shape parameter: Properties and significance. Reliability Engineering & System Safety, 96(12), 1619–1626. https://doi.org/https://doi.org/10.1016/j.ress.2011.09.003

Kasama, K., Furukawa, Z., & Yasufuku, N. (2021). Cyclic shear property and seismic runout analysis for pumice fall deposit. Soil Dynamics and Earthquake Engineering, 143, 1–11. https://doi.org/10.1016/j.soildyn.2021.106588

Kikkawa, N., Pender, M. J., & Orense, R. P. (2013). Comparison of the Geotechnical Properties of Pumice Sand from Japan and New Zealand. Proceedings of the 18th International Conference on Soil Mechanics and Geotechnical Engineering, 239–242.

Kwag, J. M., Ochiai, H., & Yasufuku, N. (1999). Yielding Stress Characteristics of Carbonate Sand in Relation to Individual Particle Fragmentation Strength. In Al-

Shafei (Ed.), Engineering for Calcareous Sediments (pp. 79–86).

Lai, C.-D. (2014). Generalized Weibull Distributions. Springer New York. https://doi.org/10.1007/978-3-642-39106-4

Lazzari, L. (2017). Statistical Analysis of Corrosion Data. In Engineering Tools for Corrosion (pp. 131–148). https://doi.org/10.1016/B978-0-08-102424-9.00008-2

Liburkin, R., Portnikov, D., & Kalman, H. (2015). Comparing Particle Breakage in an Uniaxial Confined Compression Test to Single Particle Crush Test-Model and Experimental Result. Powder Technology, 2015(284), 344–354.

Liu, C., Liu, F., Song, J., Ma, F., Wang, D., & Zhang, G. (2021). On the measurements of individual particle properties via compression and crushing. Journal of Rock Mechanics and Geotechnical Engineering, 13(2), 377–389. https://doi.org/10.1016/j.jrmge.2020.06.009

McDowell, G. R., & Amon, A. (2000). The Application of Weibull Statistics to the Fracture of Soil Particle. Soils and Foundations, 40(5), 133–141.

Nakata, Y., Kato, Y., Hyodo, M., Hyde, A. F. L., & Murata, H. (2001). One-Dimensional Compression Behaviour of Uniformly Graded Sand Related to Single Particle Crushing Strength. Soils and Foundations, 41(2), 39–51.

Ono, K. (2019). A Simple Estimation Method of Weibull Modulus and Verification with Strength Data. Applied Sciences, 9(8). https://doi.org/10.3390/app9081575

Orense, R. P., Pender, M. J., Hyodo, M., & Nakata, Y. (2016). From Micro to Macro: An Investigation of the Geomechanical Behavior of Pumice Sand. In T. Rotanda, M. Cecconi, F. Silvestri, & P. Tommasi (Eds.), Volcanic Rocks and Soils (1st ed., Issue 2, pp. 45–62). CRC Press. https://doi.org/https://doi.org/10.1201/b18897

Soda, R., Ishihara, S., Kushimoto, K., Kano, J., & Ozaki, K. (2021). Single-particle crush test for ultrafine particles and direct numerical simulation of fracture process. Powder Technology, 384, 387–401. https://doi.org/10.1016/j.powtec.2021.02.023

Sumartini, W. O., Hazarika, H., Kokusho, T., Ishibashi, S., Matsumoto, D., & Chaudhary, B. (2018). Deformation and Failure Characteristics of Volcanic Soil at Landslides Site due to the 2016 Kumamoto Earthquake. International Association of Lowland Technology, 19(4), 237–244.

Yasufuku, N., & Kwag, JM. (1999). Significance of soil particle fragmentation strength related to soil crushability. In Hong & et.al. (Eds.), Eleventh Asian Regional

Conference on Soil Mechanics and Geotechnical Enginering (pp. 149–452).

Yu, D., Jin, L., Li, J., Qin, X., Zhu, Z., & Zhang, J. (2023). Monitoring the Weibull Scale Parameter Based on Type I Censored Data Using a Modified EWMA Control Chart. Axioms, 12(5). https://doi.org/10.3390/axioms12050487

Zhou, X. P., Zhao, Y., & Qian, Q. H. (2015). A novel meshless numerical method for modeling progressive failure processes of slopes. *Engineering Geology*, *192*, 139–153. https://doi.org/https://doi.org/10.1016/j.enggeo.2015.04.005

CHAPTER V
ONE-DIMENSIONAL CONSOLIDATION PROPERTIES OF PUMICE

5.1 Introduction

It is important to examine the mechanical behavior of soil from the viewpoint of particle crushability and to comprehend the impact of particle crushing on the mechanical behavior of soils. Several researchers employ a one-dimensional consolidation test with constant strain loading to assess the contribution of soil particle crushability on the one-dimensional compression behavior. Nakata et al. (2001) conducted a one-dimensional consolidation test with a constant rate of strain loading and single-particle tests for Toyoura sand and silica sand to investigate their crushable properties. The studies discovered that the logarithm of the tensile stress for a single particle embedded in a soil matrix at the maximum compression index can be a function of the logarithm of the single-particle strength. Miranda Pino & Baudet (2015) observed the fragmentation of soil particles in seven reconstituted carbonate sands with varying mineralogist and particle sizes using a one-dimensional consolidation test with a constant rate of strain loading. The results show there was a higher occurrence of particle breakage, particularly for weak carbonate sands. Zhou et al. (2014) examined the one-dimensional compression characteristics of granular soil using the discrete element method (DEM) and Weibull distribution of single soil particle strength. The DEM simulations were validated by comparing the simulation results with the experimental data obtained from oedometer tests conducted for sand specimens. DEM simulations, which incorporate a particle crushing criterion, have successfully replicated the one-dimensional compression behavior of real sands observed in experiments. The accuracy of the proposed method was confirmed to predict the rate of particle crushing, which is the primary microscopic mechanism governing the one-dimensional compression of sands. Kikkawa et al. (2013) conducted a drained triaxial compression test and a one-dimensional compression test for pumices from Japan and New Zealand. One of the important characteristics of the drained shear behavior for two pumices is that they have a tendency to deform in a one-dimensional compression manner under significant confining pressure. Generally speaking, the characteristics of these two pumices, which come from different sources, are quite comparable. Furthermore, Kasama et al., 2021 explained the e-log$p$ curve for pumice fall deposits obtained from the one-dimensional consolidation test with the constant rate of strain loading. Consolidation was completed within 50 min for all loading stages. The consolidation yield stress and compression index are 107.8 kPa and 0.56 respectively while the initial void ratio is 4.2. The decrease in void ratio beyond consolidation yield stress is remarkable which is caused by the soil particle crushing beyond specific stress ranges.

From the given explanations, it is evident that the yield stress of one-dimensional compression behavior for sand specimens is considered to initiate sand particle crushing. This chapter examines the compression behavior of pumice using a one-dimensional consolidation test with the constant rate of strain loading and then compares the results with those obtained from a single-particle strength test.

5.2 Sample Preparation and Methodology

5.2.1 Material

The pumice utilized in this study was commercially sourced from the Miyakonojo area, Miyazaki Prefecture, Kyushu Island shown in Figure 5.1. Figure 5.1(a) is the photo of a pumice, and Figure 5.1(b) is the photo of a single pumice particle. The sample was prepared dry conditioned with four different relative densities (D_r) as seen in Table 4.1.

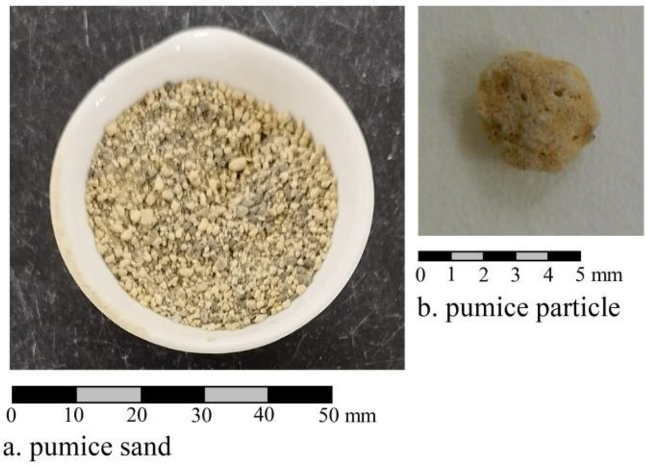

Figure 5.1 Sample for one-dimensional consolidation test

Table 5.1 Testing condition for one-dimensional consolidation test with the constant rate of strain loading

No	D_r (%)	Initial void ratio (e_0)
1	50	1.776
2	60	1.723
3	70	1.671
4	80	1.620

5.2.2 One-Dimensional Consolidation with the Constant Rate of Strain Loading

A one-dimensional consolidation test with the constant rate strain loading (JIS A 1227 : 2009) applies continuous loading for soil specimens with a constant strain rate under one-sided drainage conditions and measures the pressure applied in the axial direction and the pore water pressure on the undrained surface of the specimen. This test method is used to examine the soil compressibility, permeability, and consolidation rate. The test method has several advantages compared with conventional one-dimensional consolidation tests with constant step loadings: (1) It allows for shorter test times; (2) It enables the collection of continuous data; (3) It allows for the independent determination of soil compressibility and permeability without assuming the stress-strain relationship of the soil matrix; (4) It has a wide range of applications, from ultra-soft clay to hard clay and from organic soil to sandy clay. (5) It is easy to automate the testing process; (6) It does not involve any impact during loading. However, there are several drawbacks to consider. Firstly, it is not possible to collect data about secondary consolidation. Secondly, the results may be influenced by time effects caused by variations in strain rate. Lastly, specialized testing equipment capable of continuous loading and precise measurement is necessary. Thus far, this test method has been employed as an abbreviated technique to reduce the duration of testing. Nevertheless, there are situations where it is necessary to employ a constant strain rate loading technique. This is particularly important when loading ultra-soft clay without causing any deformation or when consistently obtaining consolidation properties close to the consolidation yield stress of hard clay.

To assess the compressibility of the pumice, a compressibility test was conducted in accordance with the JIS A 1227: 2009 standard. Figure 5.2 displays the one-dimensional consolidation test with the constant rate of strain loading apparatus.

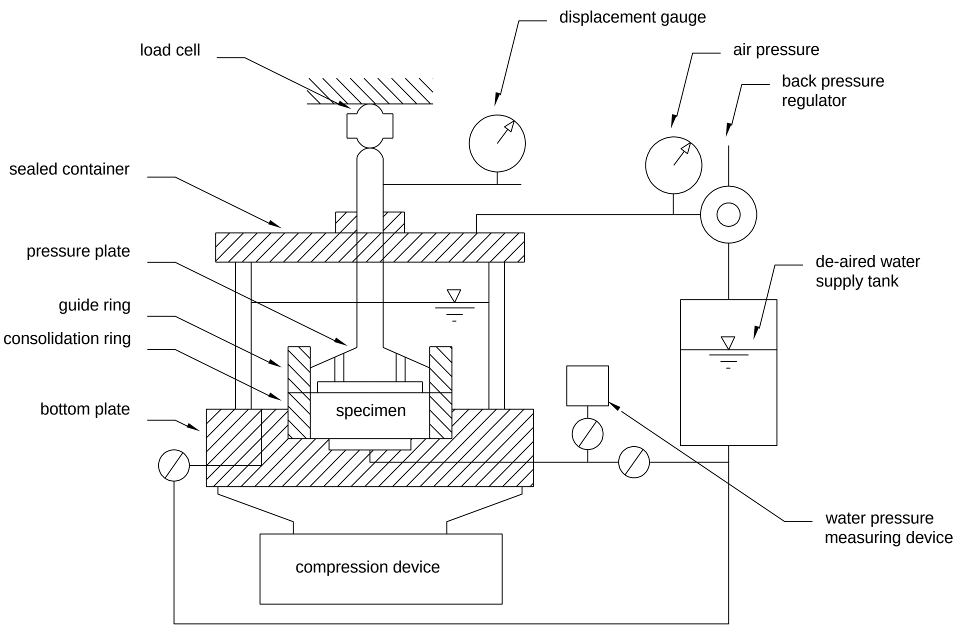

Figure 5.2 Configuration example of one-dimensional consolidation test with the constant rate of strain loading (JIS A 1227 : 2009)

To figure out the relationship between the one-dimensional consolidation test with the constant rate of strain loading and single-particle strength, Nakata et al. (2001) introduced Eq. 5.1.

$$F_{sp} = \sigma \left(\sqrt[3]{\frac{(1+e)\pi}{6}} \right)^2 \bar{d}^2 \qquad \text{Eq. 5.1}$$

where F_{sp} is the force on a single particle embedded in a soil matrix, σ is the normal stress which refers to yield stress (p_c) in this study, $\bar{d}$ is the mean particle diameter, e is the void ratio.

5.3 Results and Discussions

Figure 5.3 shows the single-particle strength depending on particle diameter, indicating that single-particle strength increases with decreasing pumice diameter size as mentioned in the previous chapter. The red line in Figure 5.3 represents the fitting line between the single-particle strength and particle diameter derived from the complete dataset (135 data). The fitting line is used to determine the average size for each group of particles. This average size is then projected onto the fitting line to obtain a representative single-particle strength for each group, as shown in Table 5.2.

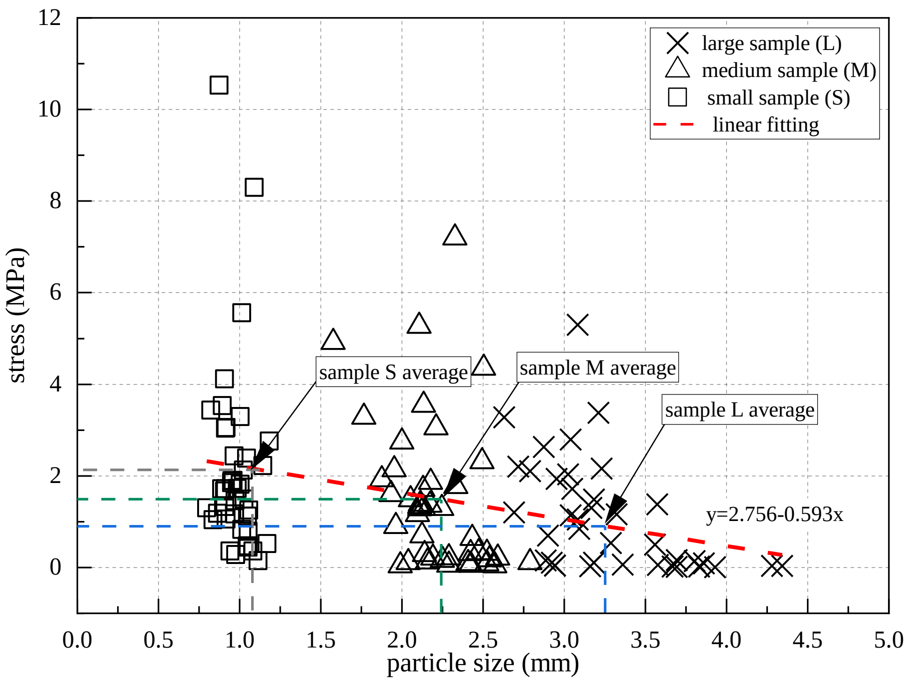

Figure 5.3 Overall single-particle strength test results

Table 5.2 Average size and single-particle strength based on single-particle strength test

Sample	particle size (mm)	stress (MPa)	force (N)
L	3.25	0.8282	28.4547
M	2.22	1.4367	15.8202
S	1.14	2.0814	3.06377

The results of the one-dimensional consolidation test with the constant rate of strain loading for pumice are depicted in Figure 5.4, compared with similar tests for clay studied by Mesri & Feng (2019) and Toyoura sand studied by Nakata et al. (2001). The yield stress p_c in this one-dimensional consolidation test with the constant rate of strain loading can be considered to initiate the crushable behavior of the pumice particle. It can be seen that the p_c of pumice lies between clay and Toyoura sand. Despite its visual resemblance to sand, the pore structure of pumice causes its p_c to be lower than that of Toyoura sand and higher than that of clay. However, the void ratio of pumice is similar to that of clay.

Moreover, a comparison of the findings from Kasama et al. (2006) study on the p_c of various materials reveals that the current study of pumice exhibits a lower p_c position than other materials can be seen in Figure 5.5. This indicates that pumice has a higher potential for being crushed, as lower p_c corresponds to greater crushability. In addition, the correlation between p_c and D_r of pumice is analogous to that of other materials, whereby an increase in D_r corresponds to an increase in the required p_c. Based on Figure 5.4 we can obtain yield stress (p_c) and compression index (C_c) for each D_r value of pumice in Table 5.3. Figure 5.6 illustrates the relationship between the variation of D_r, C_c, and p_c of pumice, it demonstrates that the C_c value decreases as D_r increases, while the p_c value increases proportionally with the increase in D_r.

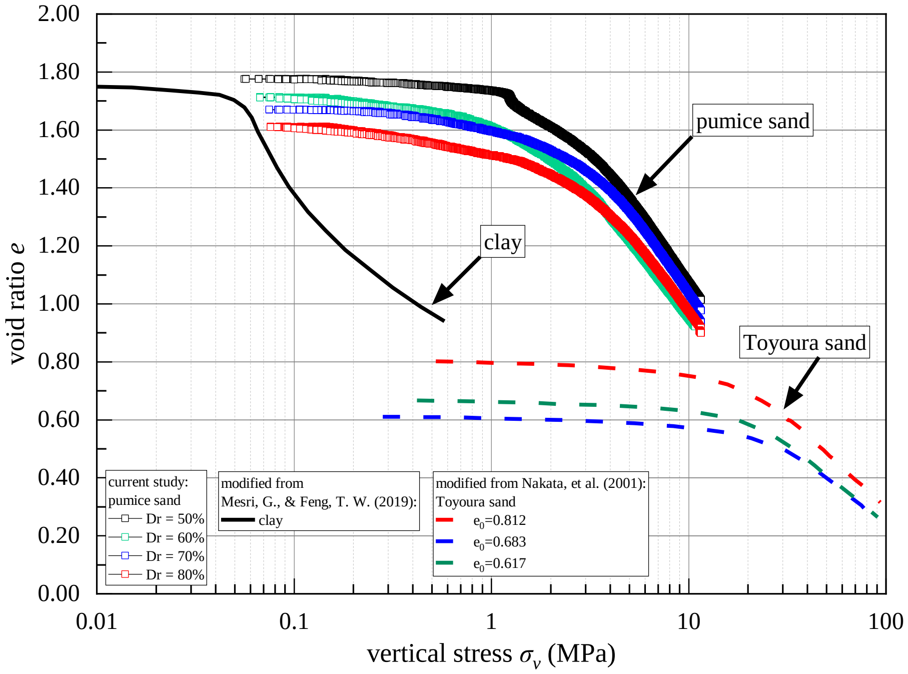

Figure 5.4 Constant strain rate consolidation test result (Basoka et al., 2024)

Table 5.3 Yield stress and compression index of pumice

relative density D_r (%)	yield stress p_c (MPa)	compression index C_c
50	0.724	0.810
60	0.749	0.936
70	0.965	0.569
80	1.048	0.640

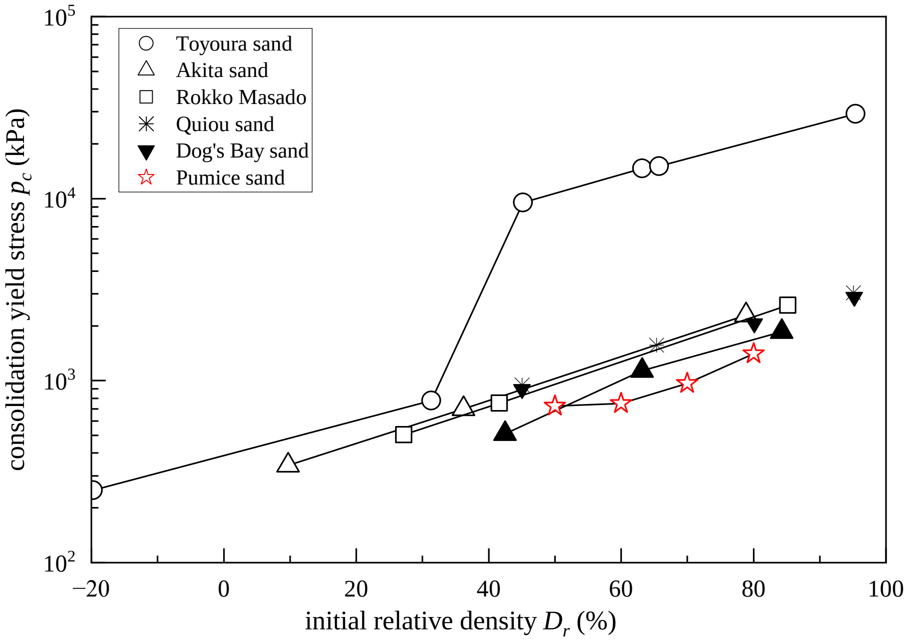

Figure 5.5 Yield stress comparison (modified from Kasama et al. (2006))

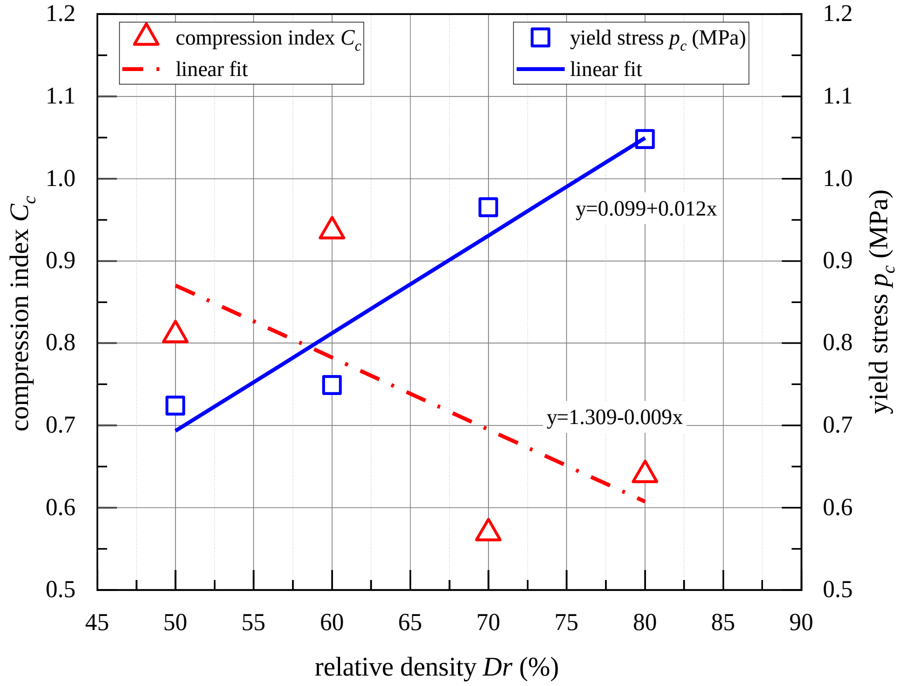

Figure 5.6 Comparison of compression index and yield stress

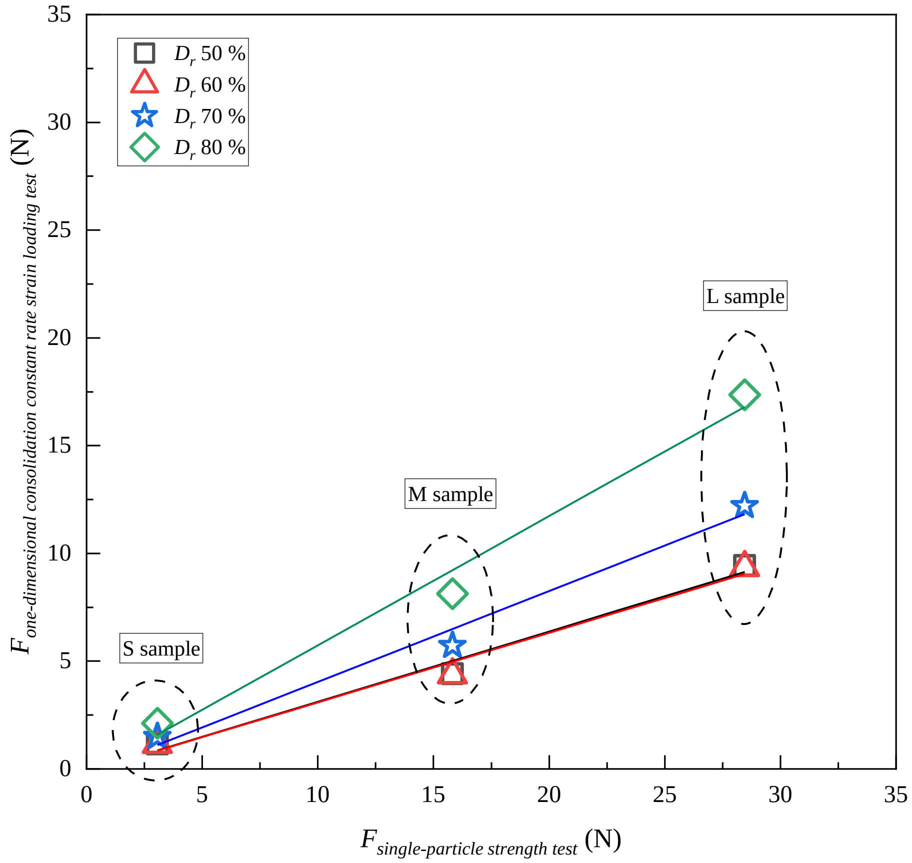

Figure 5.7 Correlation of single-particle strength of one-dimensional consolidation constant rate strain loading test and single-particle strength test

Figure 5.7 illustrates the correlation between the single-particle strength between single particle strength test and one-dimensional consolidation test with the constant rate of strain loading. It is noted that the yield stress p_c is converted to F_{sp} from the yield stress p_c for the pumice, as described by Eq. 5.1. These results demonstrate that there is a close relationship between single-particle strength of pumice as the D_r becomes higher.

5.4 Summary

Based on the results and discussions presented in the previous section, a concise summary can be formulated as follows:

1. The yield stress (p_c) of pumice is between clay and Toyoura sand (clay 0.05 MPa, pumice 0.724 MPa – 1.048 MPa, and sand 10 MPa). The pore structure of pumice causes lower p_c than Toyoura sand and higher p_c than clay irrespective of the void ratio is similar to clay.
2. The pumice has greater crushability if we compare it to other materials based on yield stress pumice which is around 0.724 MPa – 1.048 MPa with a relative density of 40% to 80%. For the compression index of pumice, we obtained 0.569 to 0.936 with a relative density of 40% to 80%.
3. The correlation between p_c and D_r of pumice is similar to that of other materials, with an increase in D_r corresponding to an increase in required p_c. It also demonstrates that the C_c value decreases as D_r increases, while the p_c value increases proportionally with the increase in D_r.
4. The correlation between the single-particle strength and the yield stress obtained from the one-dimensional consolidation test with a constant rate of strain loading is influenced by the D_r value, with higher D_r values that indicate a closer match between the single particle strength from the consolidation test and the single-particle test. Conversely, when the D_r decreases the single particle correlation further away, and when the value of D_r falls between 50% and 60%, there is no significant difference in the relationship between the single particle strength value and the p_c.

References

Basoka, I. W. A., Kasama, K., & Furukawa, Z. (2024). Constant strain rate consolidation testing for pumice sand. Japan Society of Civil Engineers Western Branch Research Presentation, 431–432.

JIS A 1227 : 2009. (2009). Test method for one-dimension consolidation properties of soils using constant rate of strain loading.

Kasama, K., Furukawa, Z., & Yasufuku, N. (2021). Cyclic shear property and seismic runout analysis for pumice fall deposit. Soil Dynamics and Earthquake Engineering, 143, 1–11. https://doi.org/10.1016/j.soildyn.2021.106588

Kasama, K., Zen, K., & Iwataki, K. (2006). Undrained Shear Strength of Cement-Treated Soils. Soils and Foundations, 46(2), 221–232. https://doi.org/https://doi.org/10.3208/sandf.46.221

Kikkawa, N., Pender, M. J., & Orense, R. P. (2013). Comparison of the Geotechnical Properties of Pumice Sand from Japan and New Zealand. Proceedings of the 18th International Conference on Soil Mechanics and Geotechnical Engineering, 239–242.

Mesri, G., & Feng, T. W. (2019). Constant rate of strain consolidation testing of soft clays and fibrous peats. In Canadian Geotechnical Journal (Vol. 56, Issue 10, pp. 1526–1533). Canadian Science Publishing. https://doi.org/10.1139/cgj-2018-0259

Miranda Pino, L. F., & Baudet, B. A. (2015). The effect of the particle size distribution on the mechanics of fibre-reinforced sands under one-dimensional compression. Geotextiles and Geomembranes, 43(3), 250–258. https://doi.org/https://doi.org/10.1016/j.geotexmem.2015.02.004

Nakata, Y., Kato, Y., Hyodo, M., Hyde, A. F. L., & Murata, H. (2001). One-Dimensional Compression Behaviour of Uniformly Graded Sand Related to Single Particle Crushing Strength. Soils and Foundations, 41(2), 39–51.

Zhou, B., Wang, J., & Wang, H. (2014). A new probabilistic approach for predicting particle crushing in one-dimensional compression of granular soil. Soils and Foundations, 54(4), 833–844. https://doi.org/https://doi.org/10.1016/j.sandf.2014.06.014

CHAPTER VI
STATIC AND CYCLIC STRENGTH PROPERTIES OF PUMICE

6.1 Introduction

Pumice is commonly found in regions with volcanic activity, such as Indonesia, Japan, Central America, and New Zealand. The unique structure of pumice, characterized by its cavities, as discussed in the previous chapter, necessitates additional investigation. The pumice in volcanic regions also is subjected to frequent dynamic loading caused by earthquakes, resulting in failure at multiple locations (Chiaro et al., 2022; Crosta et al., 2005; Faris & Fawu, 2014; Hosobuchi et al., 2021; Kasama et al., 2021; Siebe et al., 2017; Umar et al., 2018).

Several studies have been conducted to investigate the effects of cyclic loading on pumice, Orense RP & Pender MJ (2013) conducted a study on the liquefaction of pumice sand using material from Waikato, New Zealand. The study also confirms that pumice is capable of being crushed. Therefore, the conventional methods used to evaluate liquefaction in general coarse-grained sands may not be suitable for pumice. The study conducted cyclic undrained triaxial tests and observed that the effect of relative density on the liquefaction resilience of pumice is less significant compared to general hard-grained sand. In this study, Orense RP & Pender MJ (2013) showed that when the confining pressure increases the cyclic strength decreases, but when the density increases the cyclic strength also increases. Asadi et al. (2022) conducted a study using natural pumice (NP) from the North Island in New Zealand and general hard-grained sands, such as Toyoura sand. The study involved multiple sets of bender elements and cyclic undrained triaxial tests. The findings indicated that the NP sands exhibit significantly reduced shear modulus (G_{max}) in comparison to general sand, leading to increased deformability during the initial phases of the cyclic loading test. Over different values of consolidation stress (σ_c') and relative density (D_r), NP sands have substantially higher values of cyclic yield strain due to their lower G_{max} and higher cyclic resistance ratio (CRR) when compared with those of general sands. Furthermore, Faris & Fawu (2014) conducted a study on the pumice responsible for triggering landslides in Padang, West Sumatra, Indonesia. The results obtained from the cyclic triaxial compression test demonstrated that the effective confining pressure and initial shear stress showed a significant influence on the augmentation of pore water pressure.

In Japan, several researchers have observed the dynamic behavior of pumice. Kasama et al. (2021) conducted a series of cyclic box shear tests for a pumice fall deposit from Takanodai, Japan, and indicated that shear stress and vertical stress decrease under constant volume. The stress path for pumice fall deposits under constant-volume loading has cyclic mobility similar to liquefied soil. Sumartini et al. (2018) conducted a study to examine the effect of cyclic loading on the shear strength property of pumice. The study involved a series of undrained static and cyclic triaxial compression tests. The triaxial compression test demonstrated semi-dilative behavior under monotonic loading conditions with low confining stress and exhibited contractive behavior under high confining stress. During the cyclic triaxial tests conducted with in-situ confining pressure, researchers observed the occurrence of cyclic mobility under lower cyclic stress and flow failure under higher cyclic stress. In addition, Umar et al. (2019), conducted a series of cyclic loading tests on pumice. This study involved monotonic and cyclic undrained triaxial tests, as well as large-strain torsional simple shear tests. The test results indicated that pumice exhibits flow-type failure behavior, which is characterized by a sudden increase in shear strains when subjected to monotonic shear loadings. In contrast, when subjected to cyclic shear stress, there is a gradual accumulation of additional pore water pressure, which serves as an indication of an impending failure characterized by the rapid occurrence of significant shear strains.

According to those studies, it is evident that the increase in pore water pressure during an earthquake leads to liquefaction in the pumice. Additionally, there is evidence that the crushable behavior of pumice during cyclic loading may also contribute to failure. This study aims to investigate the behavior of pumice under cyclic loading conditions, specifically focusing on variations in relative density and confining pressure; these two factors have not been extensively investigated in prior studies. This study utilized commercially available pumice sourced from the Miyakonojo Area in Miyazaki prefecture, Kyushu Island. The purpose of this is to ensure the repeatability of test results and sample preparation using pumice so that the results obtained accurately reflect the properties of the pumice itself. In addition to that, the majority of the additional examination of laboratory test results is conducted using traditional frequentist approach. However, in this study, we will employ the hierarchical Bayesian approach, which offers its own set of benefits, as explained previously in Chapter 4.

6.2 Sample Preparation and Methodology

6.2.1 Material

The pumice is commercial samples (acquired from companies that collect pumice material for commercial purposes in the agricultural industry) collected from the surrounding regions of Miyakonojo area, Miyazaki Prefecture, Kyushu Island, Japan. Figure 6.1 (a) shows a pumice that was utilized in a triaxial test. This sample comprises two distinct materials, distinguished by the color of their particle. The majority of the sample is composed of white pumice as depicted in Figure 6.1 (b), while a smaller portion consists of black sand, as shown in Figure 6.1 (c). The sample selection process was conducted meticulously, considering factors such as ease of obtaining continuous samples, maintaining sample gradation, and striving for a higher level of homogeneity within the sample. Table 6.1 shows the fundamental physical characteristics of the pumice obtained from the Miyakonojo area.

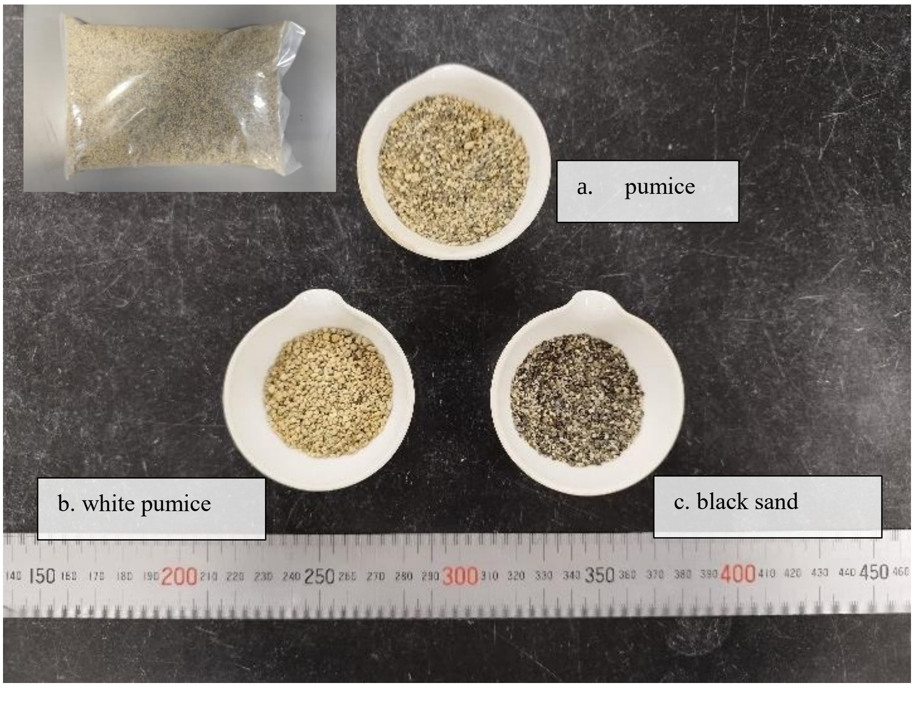

Figure 6.1 Pumice sample for triaxial test

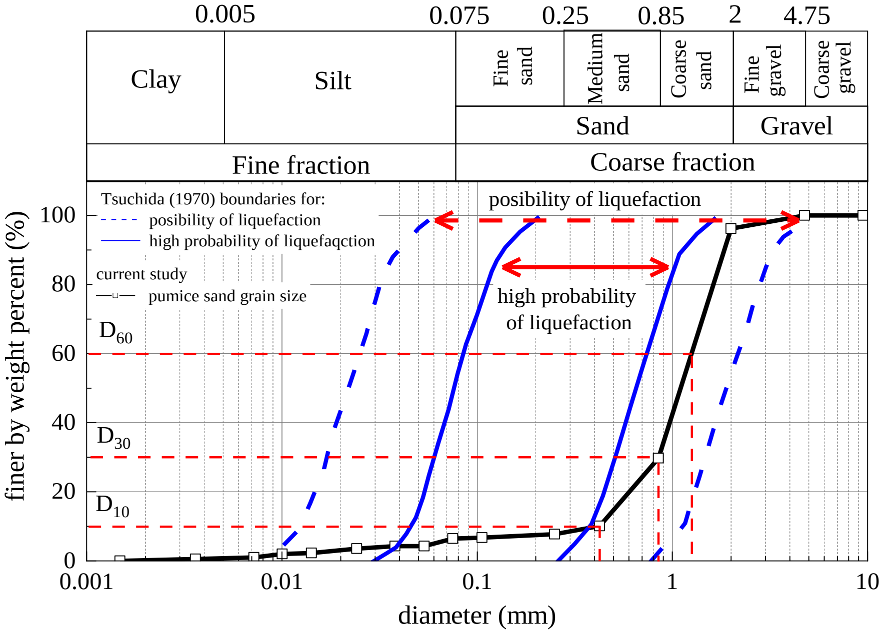

Figure 6.2 Particle size distribution and liquefaction potential

Table 6.1 Physical properties of pumice

Minimum density (g/cm^3)	0.804
Maximum density (g/cm^3)	0.953
Maximum void ratio	2.156
Minimum void ratio	1.661
Specific gravity	2.537

6.2.2 Sample Preparation and Methodology

The sample was prepared according to the guidelines specified in JGS 0530-2020 for the preparation of specimens consisting of coarse granular material, specifically for the purpose of conducting triaxial tests. The preparation of specimens involved utilizing the negative pressure technique. The sample was then remolded by dividing it into multiple layers and compacting it to the specified density with a hammer. Subsequently, a suction pressure of -20 kPa is applied to the sample to maintain its shape when the mold is removed. The load cell used is placed inside the chamber to minimize the impact of friction between the sample and the load cell caused by the connection rod.

The saturation process involves using the double negative pressure method, where a negative pressure of -80 kPa is applied inside the sample while a negative pressure of -60 kPa is applied outside the sample. This guarantees the maintenance of a constant negative pressure differential of -20 kPa. The water flushing process is iterated several times on the sample to eradicate any entrapped air. This process was iterated until the sample completely eliminates any air. The sample was subsequently exposed to a back pressure of 200 kPa in order to enhance saturation, as determined by the Skempton pore pressure value (*B*) being greater than 0.95. The sample was allowed to rest for a minimum of 2 hours until it reached saturation. The study involved subjecting the sample to a confining pressure range of 50 and 100 kPa. Once the specified Skempton value is reached (≥ 0.95), the consolidation process was started (around 2-3 hours), and the sample was then prepared for cyclic undrained triaxial testing. Consolidation undrained triaxial test carried out refer to JGS 0522-2020, consolidation drained test carried out refer to JGS 0524-2020, and cyclic undrained triaxial tests carried out refer to JGS 0541-2020 standard about the method for cyclic undrained triaxial tests on soils.

The undrained and drained static triaxial tests were conducted using three different levels of σ_c 25 kPa, 50 kPa, and 100 kPa with D_r 60%. During the cyclic undrained triaxial test, a constant cyclic stress ratio (*CSR*) value is used to apply a uniform sinusoidal load to the pumice. The *CSR* values used in the test are 0.15, 0.20, 0.25, 0.30, and 0.35, with variation D_r and confining stress (σ_c) as indicated in Table 6.2. When the *CSR* is 0.15 and the sample condition is D_r 40% and σ_c 50 kPa, the liquefaction phenomenon does not occur until the number of cycle loading approaches 1000. On the other hand, when the *CSR* value is high, specifically 0.35, and the sample condition was D_r 40% and confining 100 kPa, the sample experiences a double amplitude axial strain (*DA*) of more than 5% and the excess pore water pressure ratio value exceeds 0.95 in a cycle that has not yet reached 1 cycle. Additionally, due to time constraints, the samples were not tested under the same conditions, which led to results that were not included in the analysis. The stress parameters utilized in this investigation are as follows:

mean effective stress

$$p' = (\sigma_a' + 2\sigma_r')/3 \qquad \text{Eq. 6.1}$$

deviatoric stress

$$\sigma_d = \frac{P_c + P_E}{2A_c} \times 1000 \qquad \text{Eq. 6.2}$$

excess pore water pressure ratio

$$r_u = \frac{\Delta u}{\sigma'_c} \qquad \text{Eq. 6.3}$$

where σ'_a is axial effective stress σ'_r is lateral effective stress which is also referred to as σ'_c (effective confining stress), $P_c + P_E$ is compression and extension cyclic axial loading single amplitude, Δu is excess pore water pressure, A_c is the specimen cross-sectional area after consolidation.

Table 6.2 Testing condition for cyclic undrained triaxial test

Specimen	σ_c	*CSR*	D_r (%)	*B*
1	50 kPa	0.20	43.24	98.38
2		0.25	41.36	96.23
3		0.30	40.89	98.56
4		0.35	42.37	98.04
5		0.25	73.89	97.56
6		0.30	71.10	98.38
7	100 kPa	0.15	40.99	96.23
8		0.20	44.37	96.06
9		0.25	40.90	96.89
10		0.30	42.38	96.09
11		0.20	70.13	96.30
12		0.25	71.34	97.06
13		0.30	71.47	97.40
14		0.35	74.57	96.35

6.3 Results and Discussions

6.3.1 Static Undrained Triaxial Compression Test

(1) Stress-Strain Behavior

Figure 6.3 illustrates the correlation between deviatoric stress and axial strain under undrained and drained triaxial compression tests. From Figure 6.3, it is evident that the sample exhibits strain-hardening behavior under the undrained condition, and this means that the deviatoric stress increases continuously as the axial strain increases until it achieves a maximum strain of 15%. Unlike the undrained condition, the sample demonstrates strain softening in drained conditioned, characterized by an initial peak in stress at a specific strain, followed by a subsequent decline and a relatively constant stress level as the axial strain grows. The hardening behavior under undrained conditions demonstrates that increased pore water pressure leads to the sample experiencing hardening behavior. This phenomenon also contributes to the hardening behavior of pumice. In the drained condition, when the water is drained from the sample, there is no increase in pore water pressure. As a result, the sample reaches a point where it cannot sustain the applied force, leading to a softening process. The undrained and drained processes demonstrate that pumice exhibits strain hardening under short-term conditions such as transient loading or earthquakes. However, it demonstrates strain-softening behavior over extended periods when water can be drained from the sample. In addition, the pumice exhibits a higher degree of crushability during drain conditions, as illustrated in Figure 6.6, which contributes to its strain-softening behavior.

(2) Strength Parameter

Figure 6.4 illustrates Morh's circle and provides the shear strength parameter for undrained and drained conditions. In the undrained condition, the cohesion value is 25.93 kN/m^2, and the friction angle is 51.07 °. In the drained condition, the cohesion value is 11.99 kN/m^2, and the friction angle is 35.85 °. In these tests, the undrained condition typically yields lower values because of the decrease in mean effective stress caused by increased pore water pressure. However, the drained condition results in a lower value for pumice. By examining the particle size gradation change after undrained and drained triaxial compression tests as shown in Figure 6.6, we can observe more particle crushability of pumice under drained conditions. This behavior is closely related to the crushability of pumice, as explained in Chapter 4. Consequently, the crushable behavior of pumice reduces its shear strength in drained conditions.

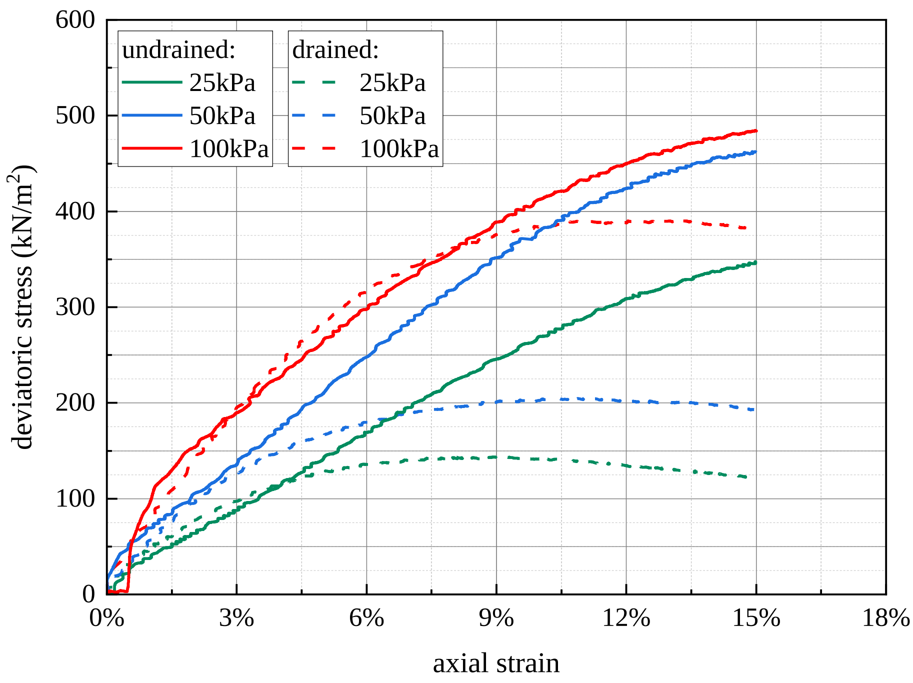

Figure 6.3 Stress versus axial strain of undrained and drained conditions

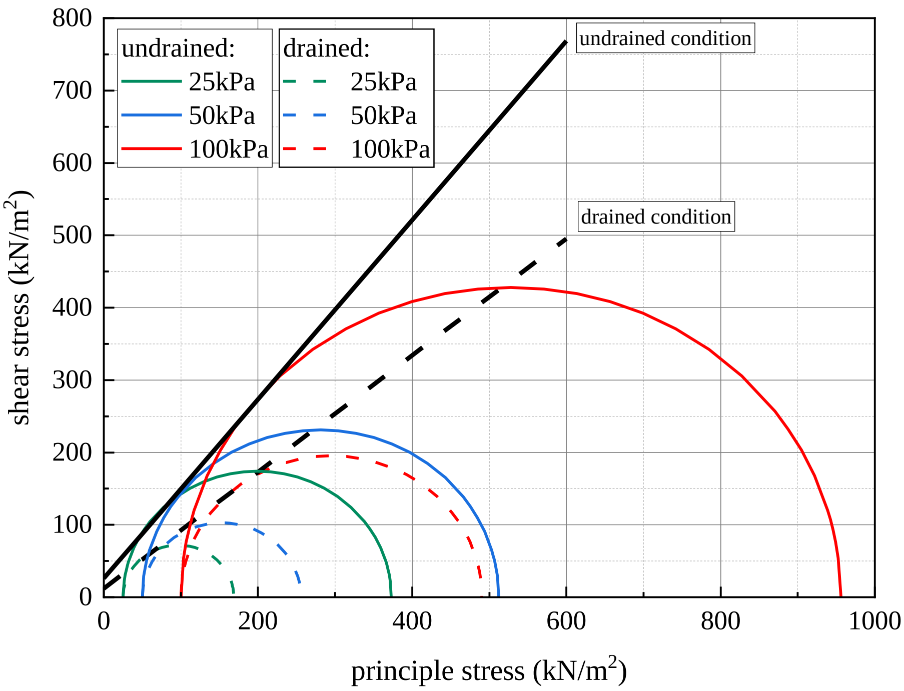

Figure 6.4 Mohr circle of undrained and drained conditions

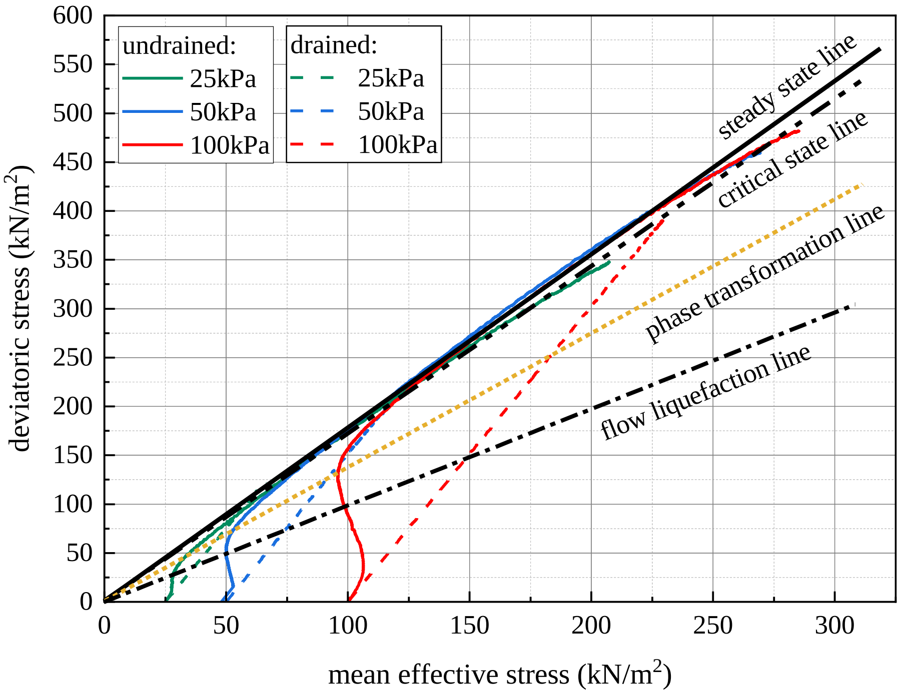

Figure 6.5 Stress path under undrained and drained conditions

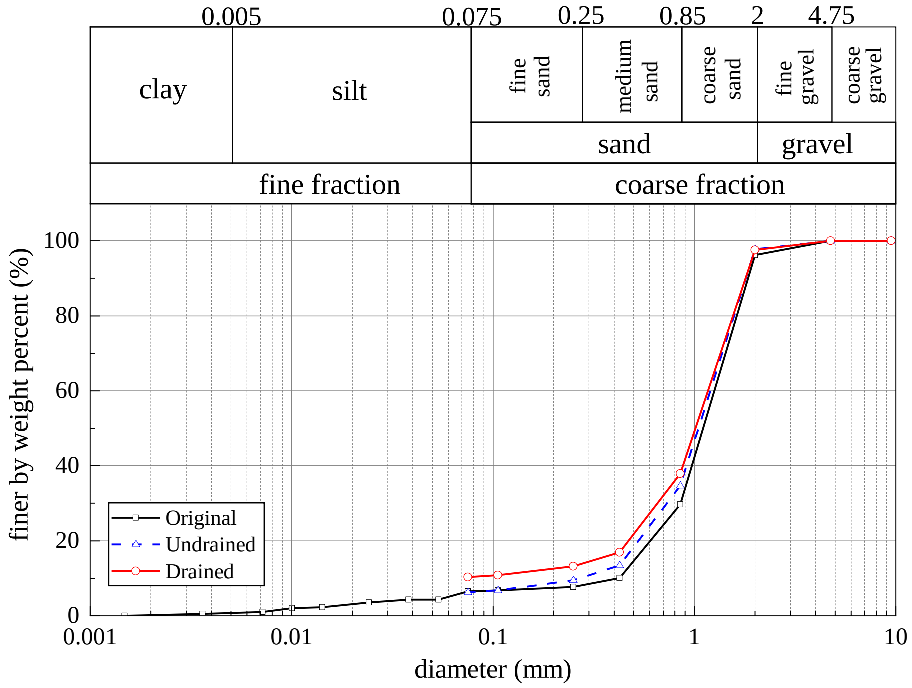

Figure 6.6 Particle size distribution before and after static triaxial compression test

(3) Stress Path

Figure 6.5 illustrates the stress path under both undrained and drained conditions. Several researchers explained the stress path under undrained and drained conditions using several representative lines (Ishihara et al., 1975; Kang et al., 2019; Umar et al., 2019). This graphic shows the steady-state line from undrained conditions and the critical-state line from drained conditions. The steady-state line seems elevated compared to the critical-state line. However, the difference between the steady-state line and the critical-state line is insignificant which is attributed to the compressible nature of the pumice. We can also observe the flow liquefaction line, which represents the rate of change in mean effective stress during the contractive phase. This line marks the threshold for the onset of liquefaction. Additionally, we can observe the phase transformation line, which indicates the minimum mean effective stress value of each stress path under drained conditions. In other words, this line represents the transition from contractive behavior to dilative behavior. This line means the liquefaction behavior under static loads by examining the previously described line boundaries.

6.3.2 Cyclic Undrained Triaxial Test

(1) Cyclic Stress Ratio (*CSR*)

Figure 6.11 illustrates the correlation between the cyclic stress ratio and the number of cycles for specimens 1–14, as detailed specimen conditions can be seen in Table 6.2. Figure 6.11 demonstrates that a higher *CSR* leads to a lower number of cycles needed to induce liquefaction (*DA* 5% or $r_u >= 0.95$), this result is consistent with the general trend observed for a given relative density and confining pressure.

(2) Axial Strain

The relationship between axial strain and loading cycle is depicted in Figure 6.4. It is observed that increasing the *CSR* value not only decreases the resistance of the pumice to liquefaction but also reduces the number of cycles required to reach 5% *DA*. All specimens are halted once the sample reaches a 5% *DA* condition. This is based on the JGS 0541-2020 standard to stop the experiment until 5% *DA* is reached, and also because if this pumice is allowed to continue to the *DA* position beyond 6%, it exhibits a failure behavior known as necking. This failure phenomenon can be observed in Figure 6.7.

Therefore, sample testing is terminated when the sample reaches a liquefaction condition with a *DA* of 5%. This approach facilitates the observation and comparison of differences in D_r and σ_c on the sample.

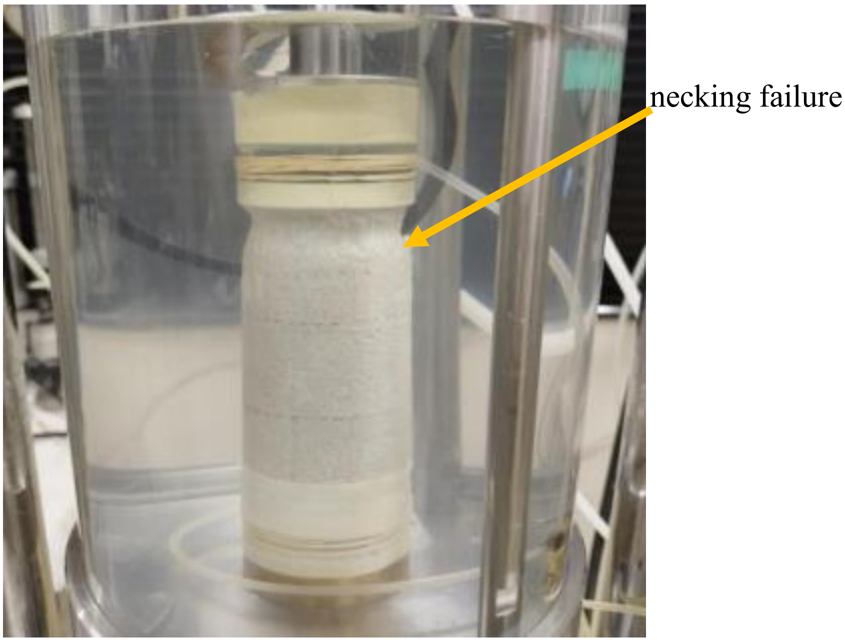

Figure 6.7 Necking failure for *DA* > 6%, testing condition for σ_c = 100 kPa, D_r = 70 %, *CSR* = 0.35

(3) Excess Pore Water Pressure Ratio

Figure 6.13 shows the pore water pressure increases with the number of cycles. For *CSR* from 0.20 to 0.35, it can be seen that there is a moment where the excess pore water pressure ratio (r_u) value is $\geq$ 0.95 calculated by Eq. 6.3, but the sample still needs an additional cyclic loading to reach 5% *DA*.

(4) Stress Path

Figure 6.14 is a stress path illustrating the correlation between mean effective stress calculated by Eq. 6.1 on the horizontal axis and deviatoric stress calculated by Eq. 6.2 on the vertical axis. The relationship between mean effective stress and deviatoric stress shows cyclic mobility when the sample starts to liquefy represented as a phase transformation line until it reaches the failure state as represented by the failure line illustrated by Ishihara et al. (1975) in Figure 6.8. By examining the same illustration, one can observe the initiation of cyclic movement in the pumice. For example in Figure 6.9 of specimen 14, cyclic mobility commences during the third cycle.

(5) Stress-Strain

Based on the relationship between deviatoric stress and axial strain in Figure 6.15, it can be seen that the pumice is mobilized in the direction of compression, which can be seen by the axial strain value, which tends towards the negative. Apart from this, it is also clear that in specimens with a σ_c of 50 kPa, the axial strain in the form of an extension loading (where the axial strain is positive) ranges from 1-2%, whereas for specimens with a σ_c 100 kPa, the axial strain in the form of an extension loading is no more than 1%. This behavior is attributed to the increased confinement of the specimen at higher pressures. The relationship between deviatoric stress and axial strain in small strain conditions reveals a parameter in the cyclic behavior of a material known as the shear modulus (G). In this study, the shear modulus can be estimated using Eq. 6.4, which is related to the young modulus (E). The young modulus can be calculated using Eq. 6.5, for each parameter for calculation is illustrated by Figure 6.10, which represents specimen 14. When calculating shear modulus using Eq. 6.4, we can assume the Poisson's ratio (v) is equal to 0.50 for undrained conditions.

$$G = \frac{E}{2(1+v)} \qquad \text{Eq. 6.4}$$

$$E = \frac{2\sigma_c}{(\varepsilon_1 + \varepsilon_2)} \qquad \text{Eq. 6.5}$$

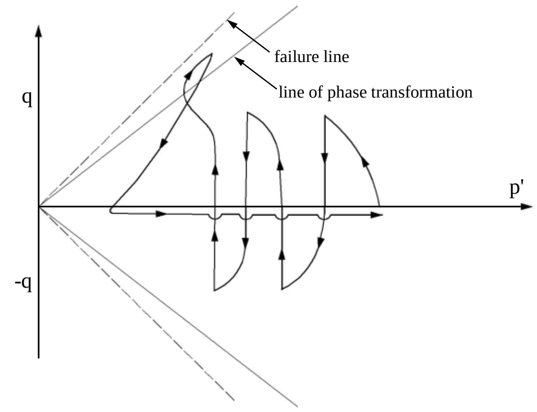

Figure 6.8 Illustration for large shearing and cyclic mobility (modified from Ishihara et al. (1975))

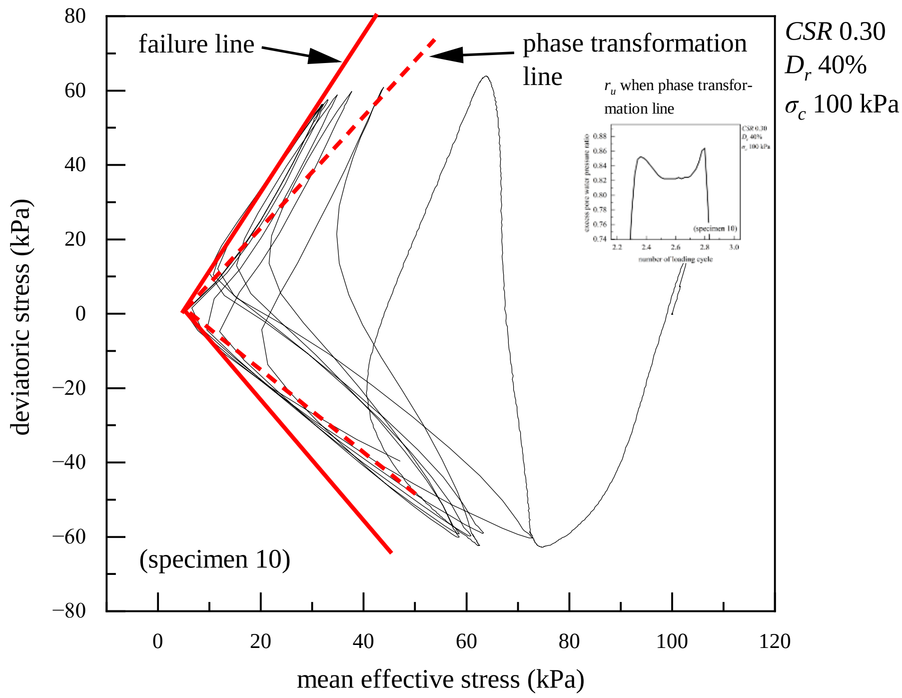

Figure 6.9 Typical of cyclic mobility (example specimen 10)

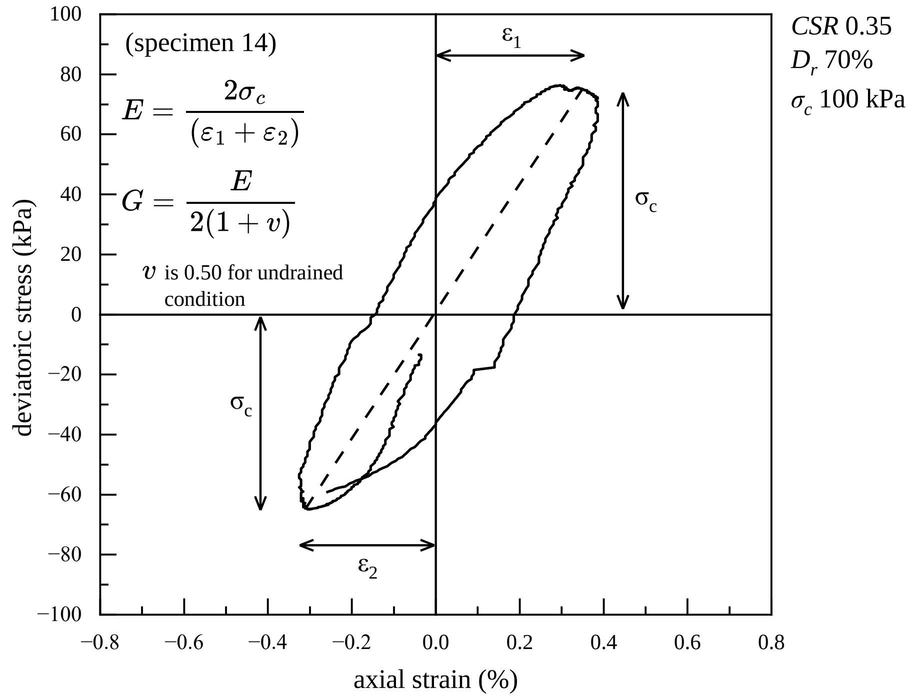

Figure 6.10 Typical of deviatoric stress versus axial strain for small strain (1st cycle) to calculate young modulus (example specimen 14)

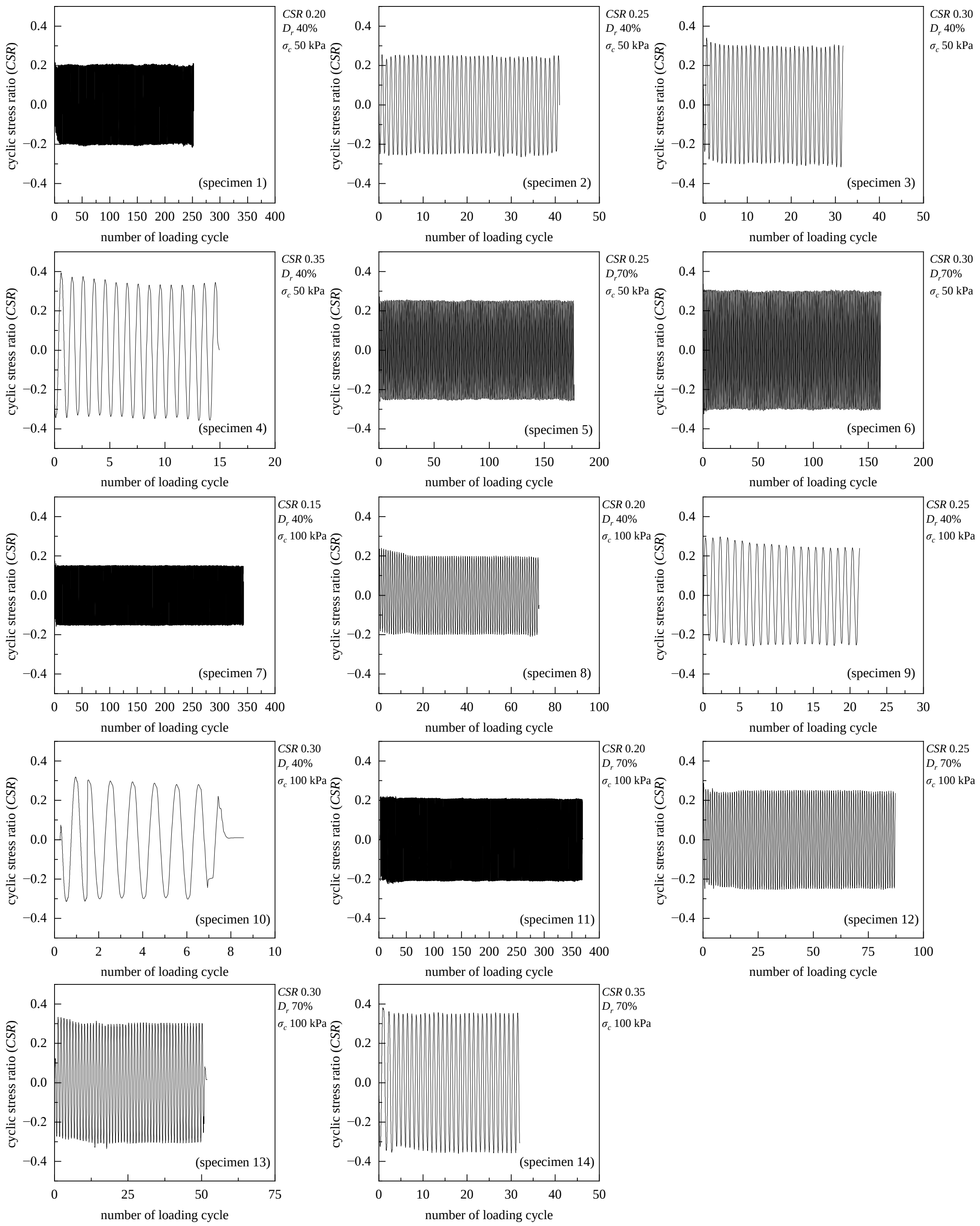

Figure 6.11 Cyclic stress ratio versus number of cycle

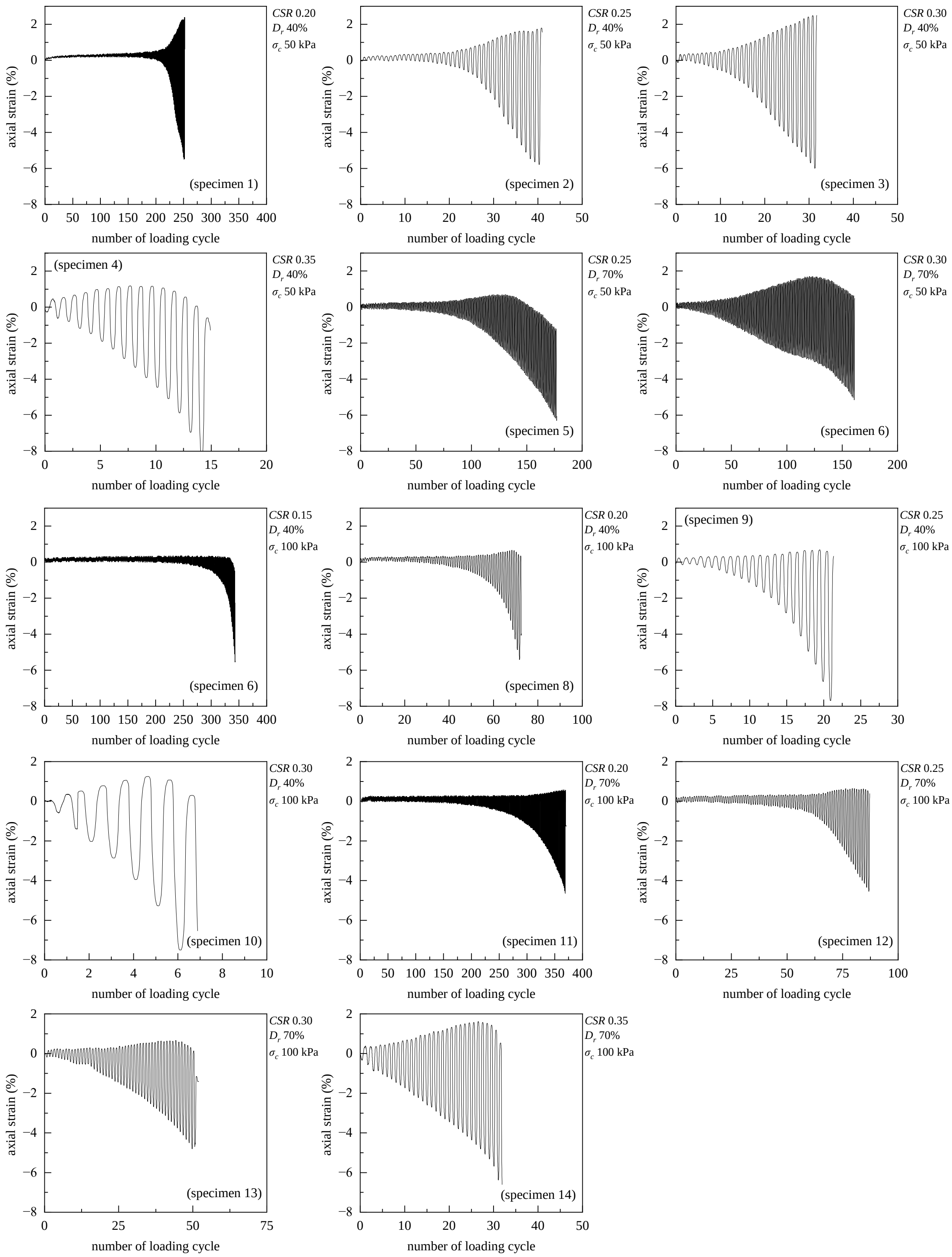

Figure 6.12 Axial strain versus number of cycle

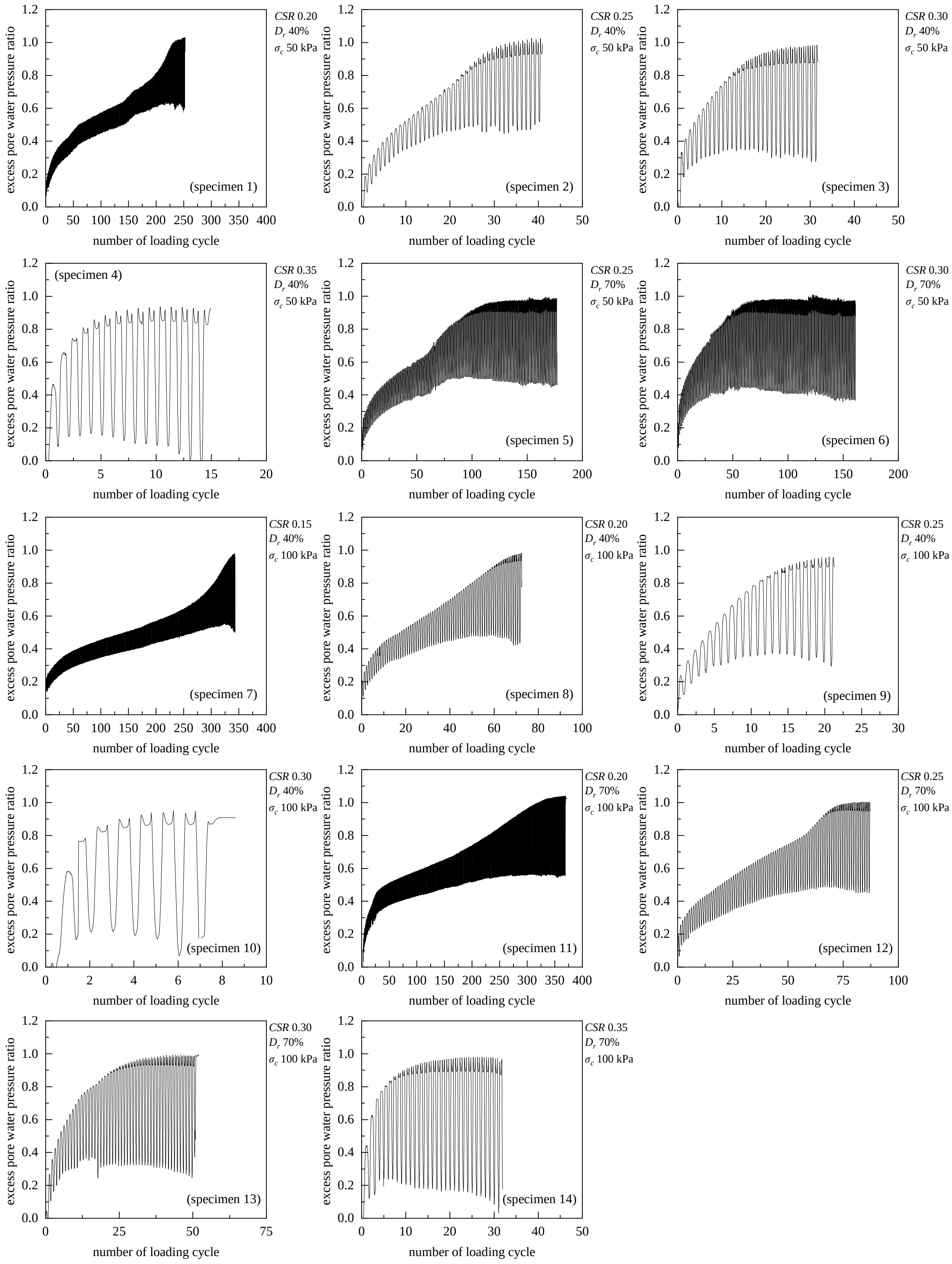

Figure 6.13 Excess pore water pressure versus number of cycle

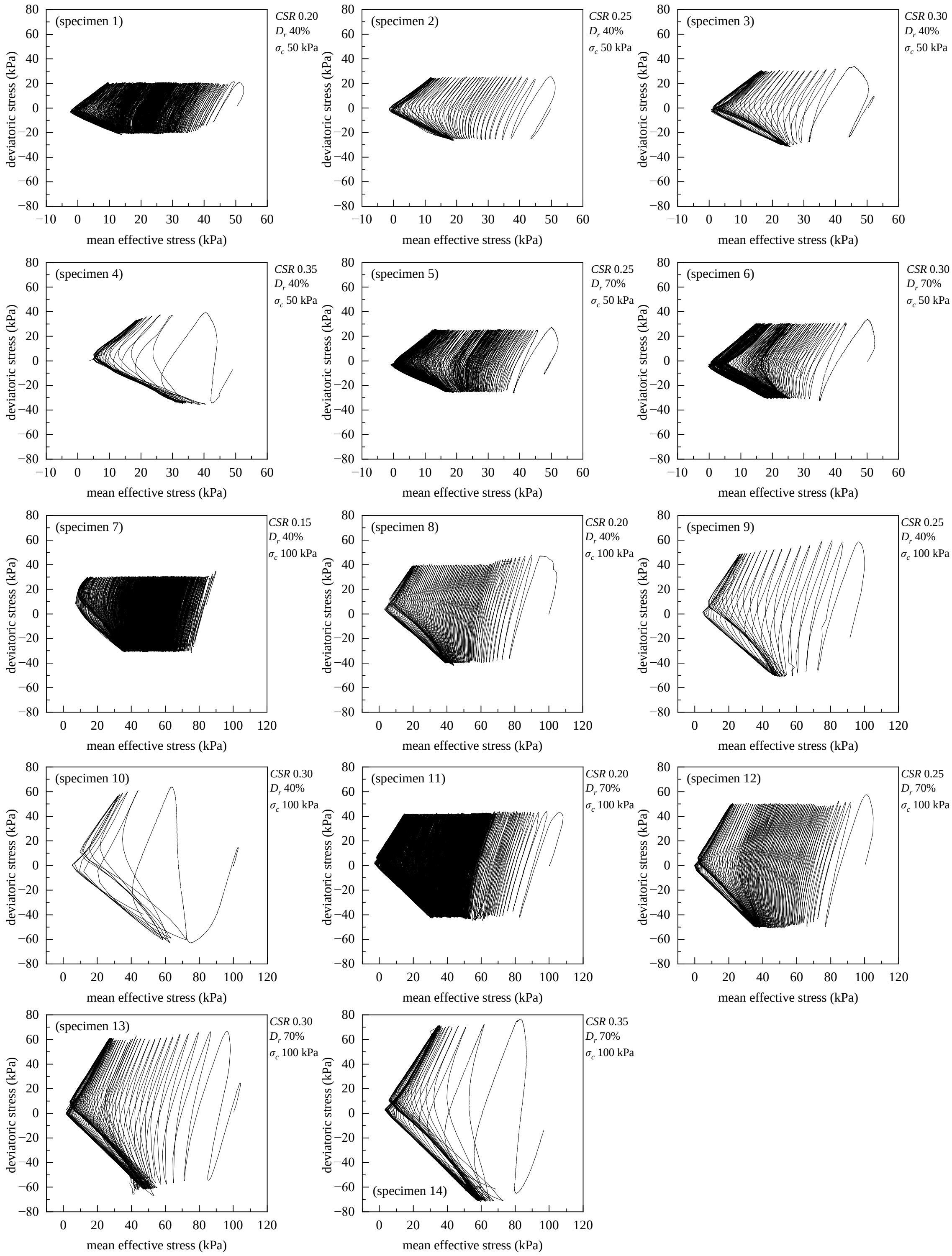

Figure 6.14 Deviatoric stress versus mean effective stress

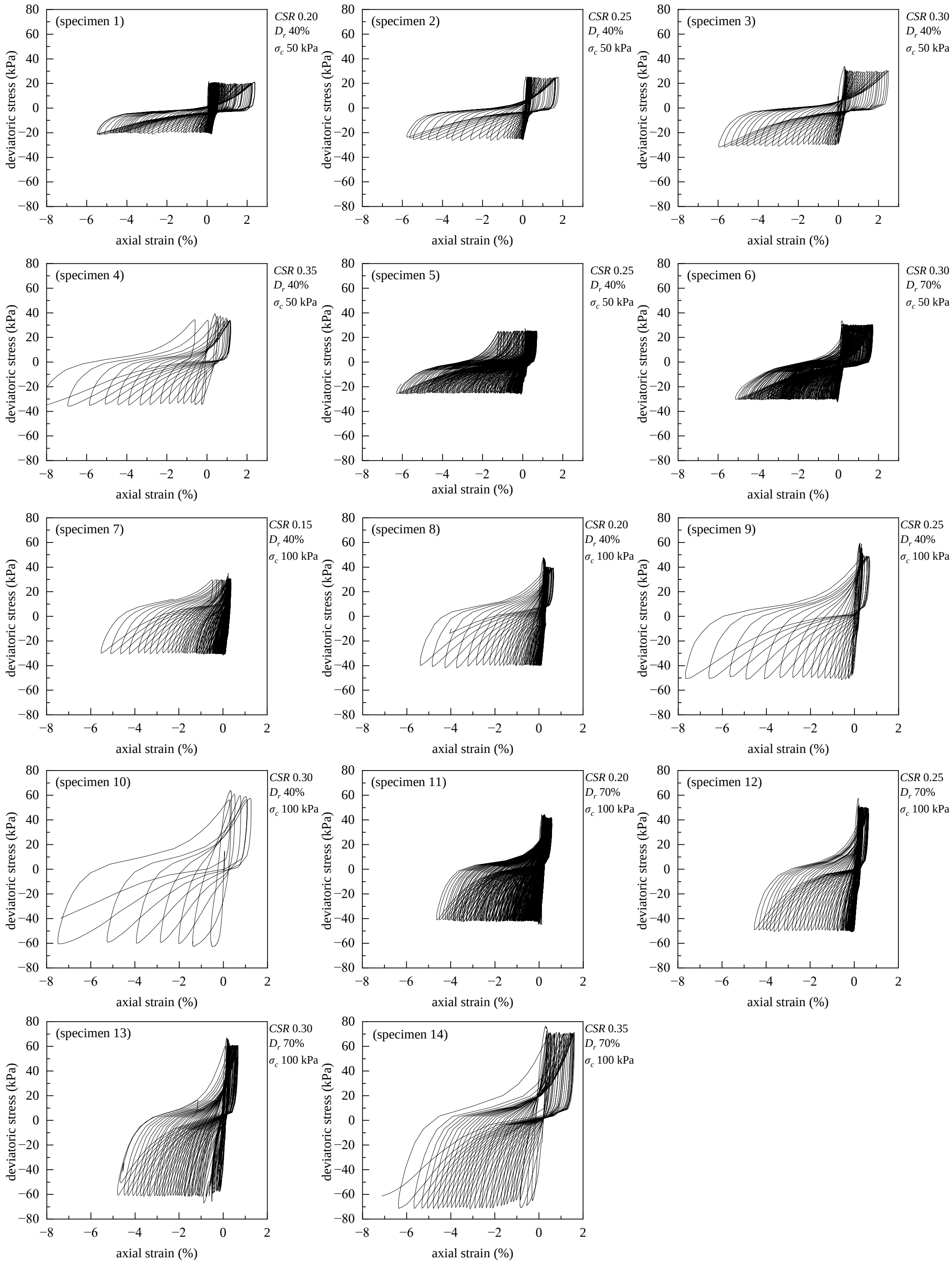

Figure 6.15 Deviatoric stress versus axial strain

6.3.3 Liquefaction Resistance

The number of cyclic loading to reach cyclic mobility, 1% *DA*, 2% *DA*, and 5% *DA* (liquefaction occurred) is summarized in Table 6.3 and plotted in Figure 6.16. In Figure 6.16, we can see that cyclic mobility occurs before the sample reaches 1% *DA*. However, when the *CSR* value is 0.35, the cycles required for cyclic mobility surpass those needed to reach 1% *DA*. Its mean cyclic mobility occurred after the sample reached 1% *DA*. For *CSR* = 0.35, the axial strain required to achieve a 1% *DA* is primarily attributed to the axial static stress applied to the sample rather than the cyclic load exerted.

Table 6.3 Number of cycles needed for cyclic mobility, 1% *DA*, 2% *DA*, 5% *DA*

Specimen	σ_c	*CSR*	D_r (%)	Number of cycles			
				Cyclic mobility	*DA*		
					1%	2%	5%
1	50 kPa	0.2	43.24	200	218	225	238
2		0.25	41.36	21	23	27	34
3		0.3	40.89	9	10	15	23
4		0.35	42.37	2.5	1	3	9
5		0.25	73.89	68	95	115	175
6		0.3	71.1	25	42	65	139
7	100 kPa	0.15	40.99	285	312	329	355
8		0.2	44.37	45	53	61	70
9		0.25	40.9	7	8	12	17
10		0.3	42.38	2	1	2	4
11		0.2	70.13	266	279	319	368
12		0.25	71.34	54	62	70	89
13		0.3	71.47	15	17	27	51
14		0.35	74.57	5	3	8	22

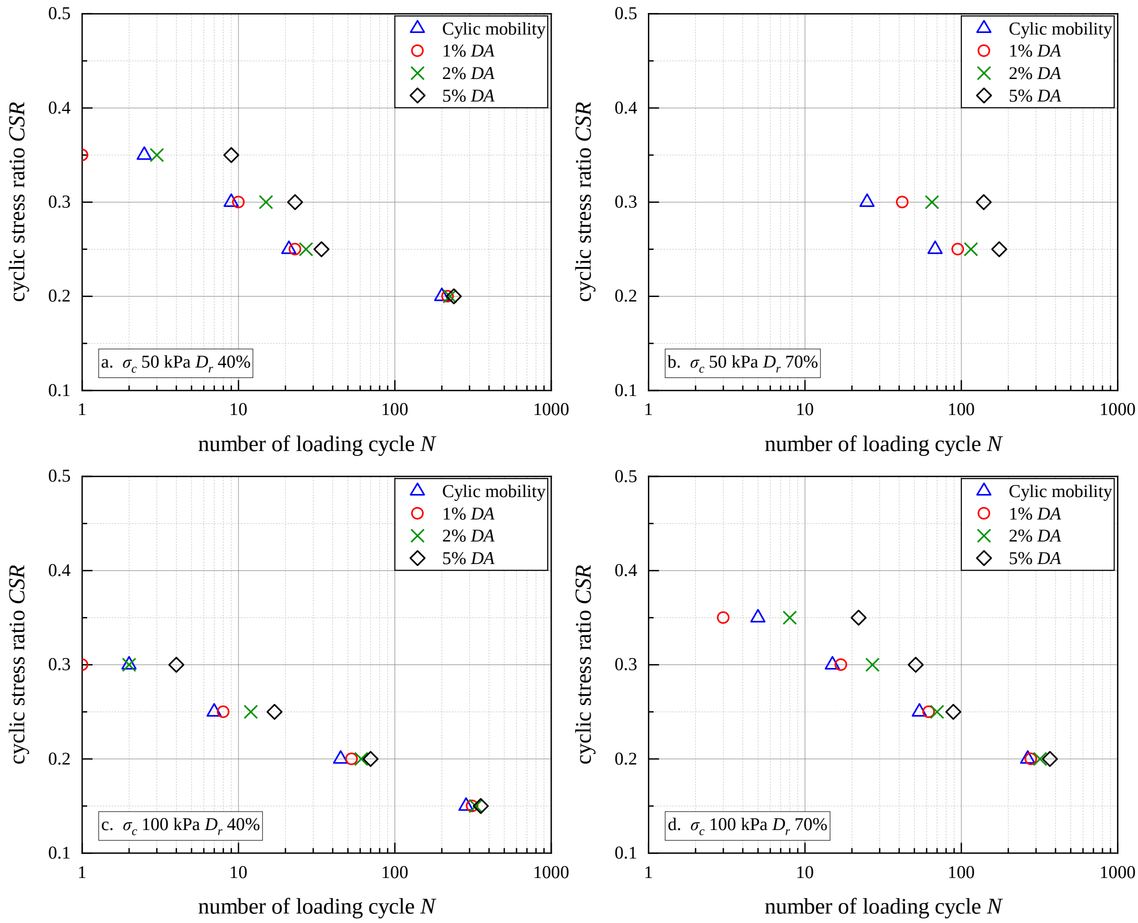

Figure 6.16 *CSR* and number of cyclic loading (a) $\sigma_c = 50kPa\ D_r = 40\%$, (b) $\sigma_c = 50kPa\ D_r = 70\%$, (c) $\sigma_c = 100kPa\ D_r = 40\%$, (d) $\sigma_c = 100kPa\ D_r = 70\%$

(1) Confining Pressure Effect

This section aimed to analyze the influence of σ_c on pumice. Two different σ_c values, specifically 50 kPa and 100 kPa, were applied to observe the effect of σ_c on the liquefaction resistance. Figure 6.17 illustrates the effect of two different σ_c on various D_r values. Figure 6.17 (a) illustrates the relationship between the number of cyclic loading needed to achieve cyclic mobility conditions and the double amplitude strain level (expressed as 1% *DA*, 2% *DA*, and 5% *DA*) in a sample with a $D_r = 40\%$ it is evident that increasing the σ_c leads to a decrease in the number of cyclic loading needed to achieve the liquefaction state. In other words, a higher σ_c 100 kPa reduces the liquefaction resistance, resulting in a lower number of cyclic loading required at a σ_c 100 kPa and a higher number of cycles required at a σ_c 50 kPa. This phenomenon was also observed in samples with a D_r 70% in Figure 6.17 (b), wherein the number of cyclic loading needed was lower under a σ_c 100 kPa as compared to σ_c 50 kPa. It is not general understanding for researchers to compare the effect of confining pressure on sand-like materials, particularly those found in the Japanese region. It is generally understood that variations in confining pressure on sand-like materials do not have a significant effect on the number of cycles required to reach liquefaction conditions (Hyodo, Tanimizu, et al., 1994). Therefore, when testing sand-like materials, 100 kPa is often used as the standard confining pressure for cyclic undrained triaxial tests Orense RP & Pender MJ (2013) results further supported this finding by examining the effect of confinement on pumice. Orense RP & Pender MJ (2013) used pumice sourced from New Zealand for testing samples with different levels of σ_c including 35 kPa, 100 kPa, and 500 kPa. The confining pressure dependency on the liquefaction strength was also observed in Orense RP & Pender MJ (2013).

(2) Relative Density Effect

In order to discuss the effect of D_r on the liquefaction curve of pumice, Figure 6.18 shows the liquefaction curve depending on D_r. Specifically, Figure 6.18 (a) shows a pumice subjected to σ_c 50 kPa. It is evident that the relative density enhances the liquefaction strength of pumice. Similarly, in Figure 6.18 (b), it is evident that when σ_c 100 kPa, the sample with D_r 70% requires a greater number of cyclic loading compared to that of the sample with D_r 40%. This trend of liquefaction strength of pumice agrees with those of general sand.

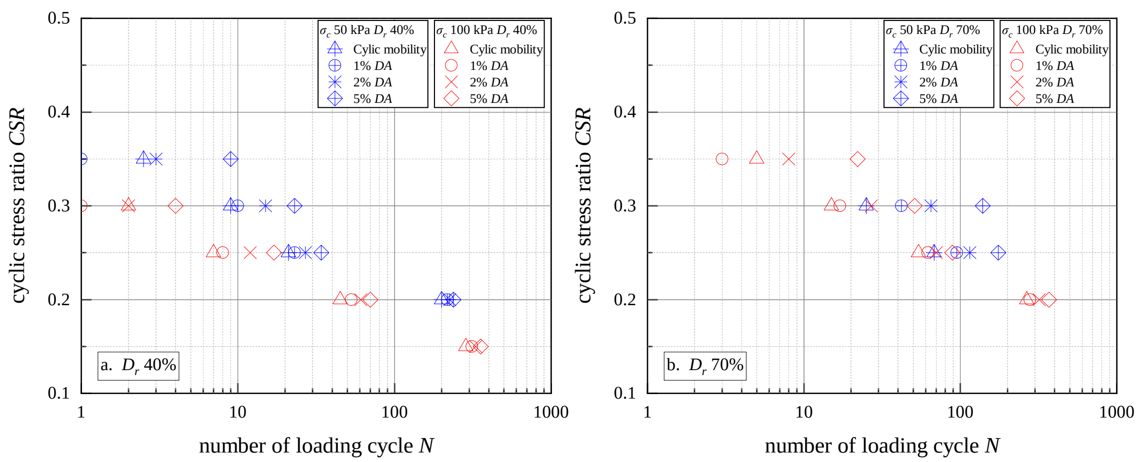

Figure 6.17 Effect of confining pressure

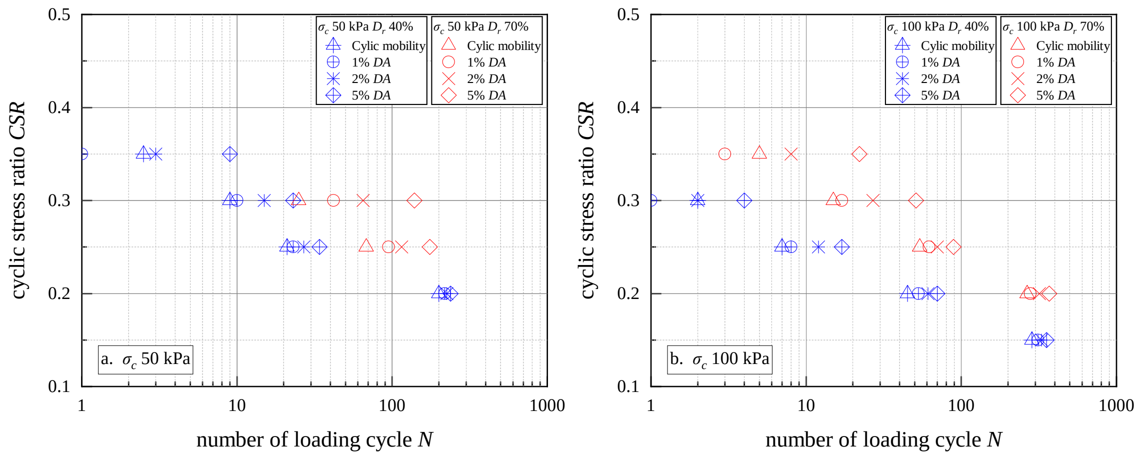

Figure 6.18 Effect of relative density

(3) Liquefaction Resistance Comparison

Figure 6.19 illustrates the liquefaction curve using *DA* = 5%. It was confirmed that confining pressure σ_c affects the liquefaction resistance of pumice. There is limited research on the effect of σ_c on the liquefaction resistance of pumice. It has been observed the liquefaction resistance of pumice increases as the σ_c decreases. However, this relationship is not widely known for general geomaterials like sand. Hence, a comparison was conducted between the findings of the present investigation and those of prior studies, as depicted in Figure 6.20. In Figure 6.20 Hyodo et al. (1994) have shown that σ_c does not affect the liquefaction resistance of sand materials generally, in the other hand Pumice exhibits clear liquefaction resistance dependency on confining pressure, which is supported by Orense RP & Pender MJ (2013) based on the test result for pumice sourced from New Zealand. As for the effect of relative density D_r on the liquefaction resistance, the pumice characteristic is consistent with other materials such as sand. Namely, the increase in D_r leads to an increase in the liquefaction resistance as shown by Asadi et al. (2022).

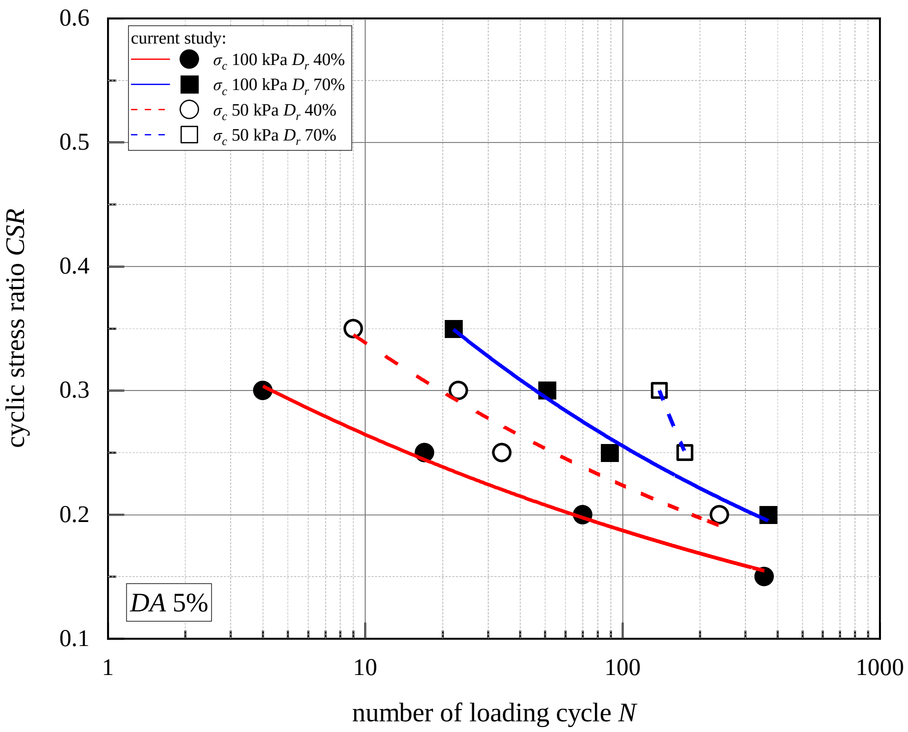

Figure 6.19 Comparison of liquefaction resistance (5% *DA*)

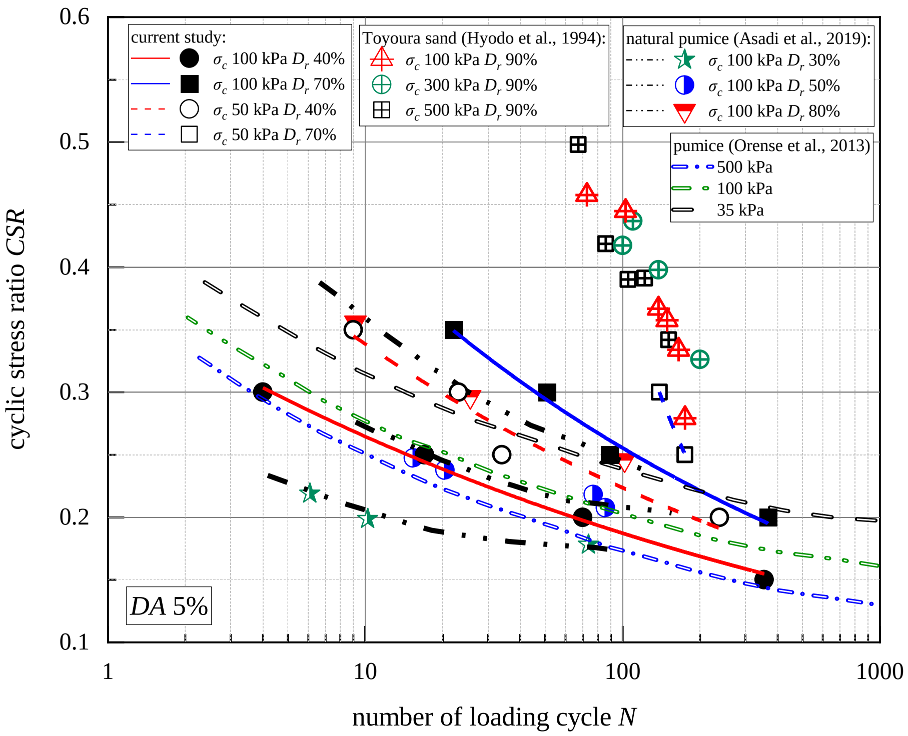

Figure 6.20 Comparison of liquefaction resistance with other studies (Basoka et al., 2024)

(4) Particle Size Evolution

In order to assess the extent of the particle crushability of pumice resulting from the cyclic load, the particle size distribution after completing the cyclic undrained triaxial test was conducted, as shown in Figure 6.21. It is noted that the test result is for the sample with a *CSR* of 0.30. Based on the test result of the one-dimensional consolidation test in Chapter 5, it was found that the pumice needs a yield stress of approximately 0.72 MPa to 1.05 MPa for relative density from 50% to 80% to undergo particle crushability. However, for *CSR* of 0.30, the maximum axial stress is only 0.03 MPa and the confining pressure is only 0.10 MPa. These two stresses have not reached the minimum yield stress, leading to minimal particle size changes.

A magnification section was created at the particle size distribution change location to facilitate observation in Figure 6.21. Comparing the two positions, it is evident that the lower D_r exhibited greater crushability at the same confining pressure, as demonstrated by the decrease in values of D_{30} and D_{60}. Additionally, under the same density conditions, increasing confinement produces finer particles, indicating a higher degree of crushability. While the trend of gradation changes aligns with previous study findings (Fangwei, 2018; Gupta, 2016; Hyodo et al., 2016), additional experimentation is required to examine the behavior of pumice at high confining pressure above its yield stress for a better understanding of the crushability effect.

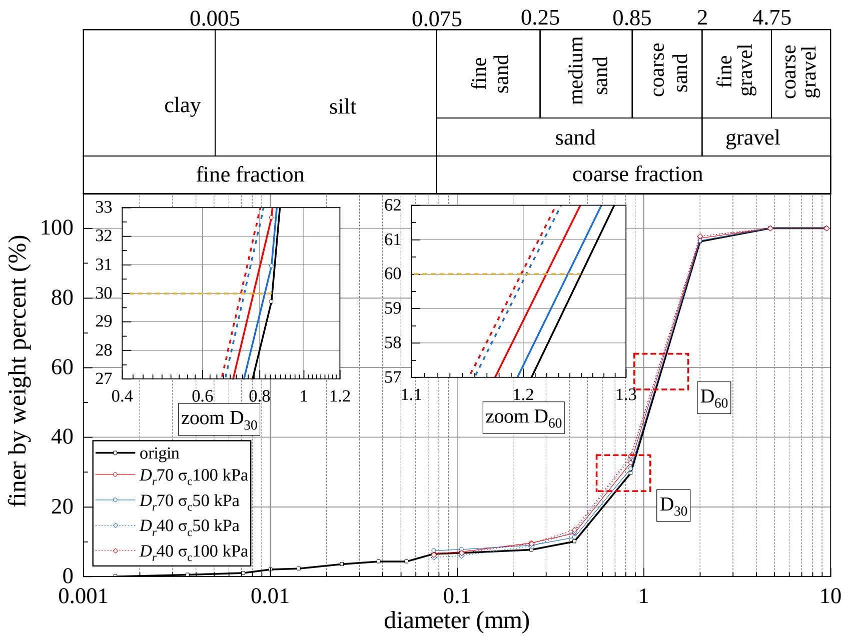

Figure 6.21 Particle size evolution after cyclic undrained triaxial test

6.3.4 Shear Modulus

The shear modulus (G) is one of the important dynamic parameters in cyclic undrained triaxial testing. The shear modulus value for each sample is obtained using this calculation from Young's modulus (E), as the results are shown in Table 6.4. Figure 6.22 to Figure 6.25 illustrate the relationship between Young's and shear modulus with confining pressure and density. Figure 6.22 and Figure 6.24 demonstrate that, when subjected to identical confining pressure conditions, an increase in relative density leads to higher values of Young's and shear modulus. Conversely, Figure 6.23 and Figure 6.25 illustrate that an increase in confining pressure results in elevated values of Young's and shear modulus at the same relative density.

Table 6.4 Young's modulus and shear modulus

Specimen	σ_c	*CSR*	D_r (%)	Young's modulus E (kPa)	Shear modulus G (kPa)
1	50 kPa	0.2	43.24	30481.82	10160.61
2		0.25	41.36	24433.33	8144.44
3		0.3	40.89	12902.44	4300.813
4		0.35	42.37	9695.83	3231.94
5		0.25	73.89	26270.00	8756.67
6		0.3	71.1	22814.29	7604.76
7	100 kPa	0.15	40.99	39180.00	13060.00
8		0.2	44.37	-	-
9		0.25	40.9	30785.29	10261.76
10		0.3	42.38	14687.21	4895.74
11		0.2	70.13	53025.00	17675.00
12		0.25	71.34	41312.50	13770.83
13		0.3	71.47	39006.45	13002.15
14		0.35	74.57	19894.03	6631.34

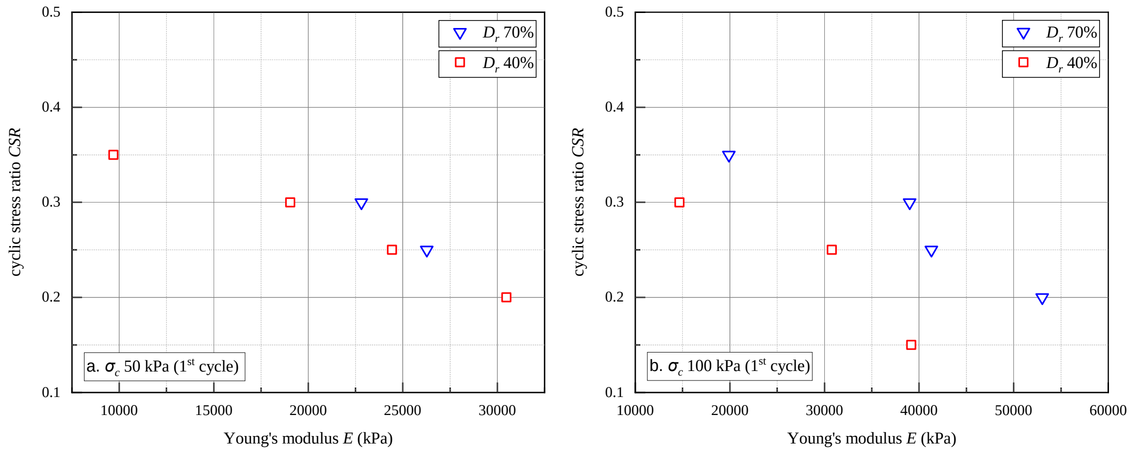

Figure 6.22 Young’s modulus behavior based on confining pressure

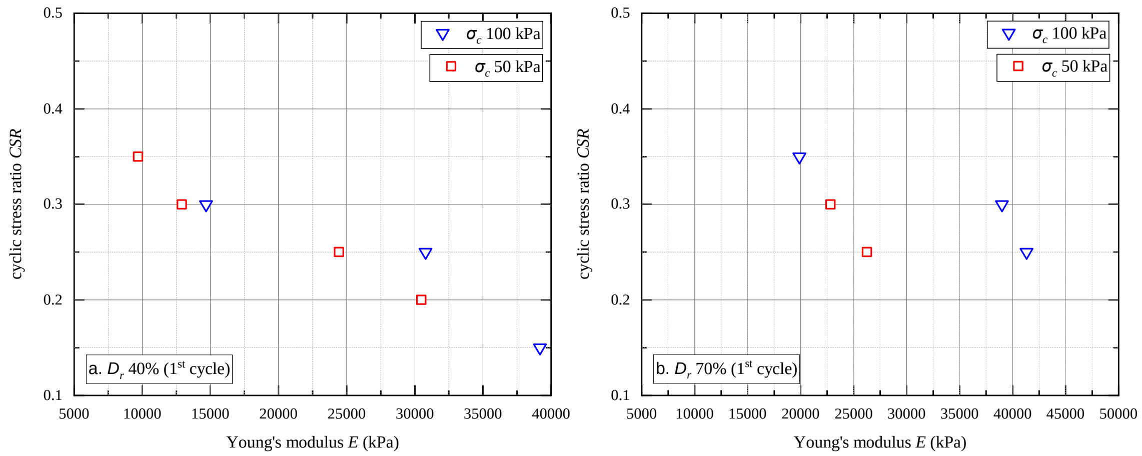

Figure 6.23 Young’s modulus behavior based on relative density

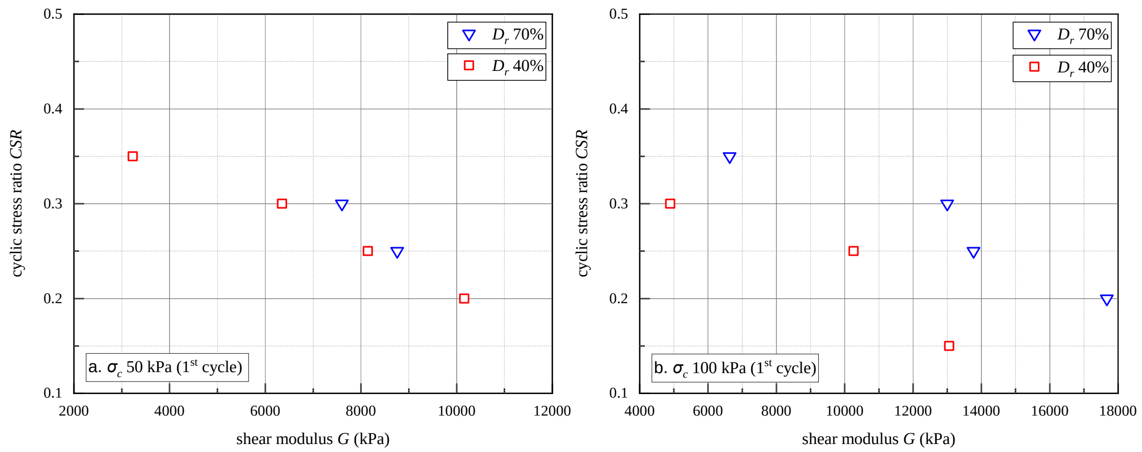

Figure 6.24 Shear modulus behavior based on confining pressure

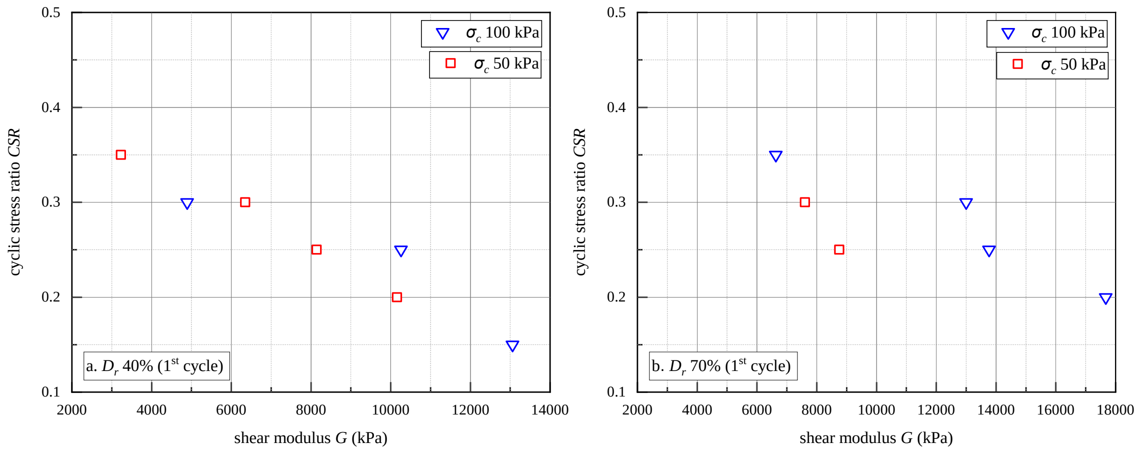

Figure 6.25 Shear modulus behavior based on relative density

6.3.5 Bayesian Approach

Based on previous results, the data we obtained was relatively small. For example, only two data were obtained for the testing condition with a confining pressure of 50 kPa and a D_r value of 70%. This limited test number poses challenges in making projections, especially when the samples are subjected to varying loads and cycle conditions. The cyclic resistance ratio (*CRR*) is commonly derived from the *CSR* value at the 20th cycle condition (Ishihara, 1993; Rahman & Sitharam, 2020; Seed & Idriss, 1971). Figure 6.19 employs conventional statistical methods but there is a testing condition with limited observations (confining pressure of 50 kPa and a D_r value of 70%). In order to overcome the disadvantage of limited data, a Bayesian approach, as employed in Chapter 4, was utilized further to examine the cyclic behavior of the pumice. Ueda, K. (2022) endeavored to employ a Bayesian approach for liquefaction evaluation. This analysis demonstrated that a hierarchical Bayesian approach can comprehensively understand the variation and interaction among different test groups.

(1) Input for Bayesian Approach

This analysis identifies three primary components: the prior function, the likelihood function, and the posterior function. Our initial step was to ascertain the likelihood or model we will examine. In the case of liquefaction evaluation, the cyclic stress resistance curve was typically expressed by Eq. 6.6 following normal distribution as Eq. 6.7 (Ueda, 2022).

$$CSR = a\,N^{\,b} \qquad \text{Eq. 6.6}$$

where CSR is the cyclic stress ratio, N is the number of cycles needed to achieve liquefaction for DA 5%, a and b are the parameters whose values will be predicted, and in this study parameters a and b are assumed to be normally distributed as Eq. 6.8 and Eq. 6.9.

$$f(CSR_i|\mu_{CSR},\sigma_{CSR}) = \frac{1}{\sqrt{2\pi\sigma_{CSR}}} exp\left[-\frac{(CSR_i-\mu_{CSR})^2}{2\sigma_{CSR}^2}\right](i = 1,2,\dots,N) \quad \text{Eq. 6.7}$$

$$f(a_i|\mu_a,\sigma_a) = \frac{1}{\sqrt{2\pi\sigma_a}} exp\left[-\frac{(a_i-\mu_a)^2}{2\sigma_a^2}\right](i = 1,2,\dots,N) \quad \text{Eq. 6.8}$$

$$f(b_i|\mu_b,\sigma_b) = \frac{1}{\sqrt{2\pi\sigma_b}} exp\left[-\frac{(b_i-\mu_b)^2}{2\sigma_b^2}\right](i = 1,2,\dots,N) \quad \text{Eq. 6.9}$$

After assessing the probability function, proceed to establish the prior for parameters a and b, as followed by Ueda, K. (2022). The value of parameter a is confined to the range of 0 to 0.5 and parameter b ranges from 0 to -0.5. Based on this information, the prior function was considered to be established in the following manner: μ_a 0.25, σ_a 0.1, $\mu_b - 0.25$, σ_b 0.1. The posterior function was analyzed using Markov Chain Monte Carlo (MCMC) with 5,000 draw samples and 2,000 tune samples. The analysis was performed using 4 chains, resulting in a total of 28,000 samples. The posterior calculation was furthered using the PyMC module in the Python programming language. The analysis will utilize two distinct approaches: the conventional/nonhierarchical Bayesian approach, which is represented by the schema model in Figure 6.26, and the hierarchical Bayesian approach, which is represented by the schema model in Figure 6.27.

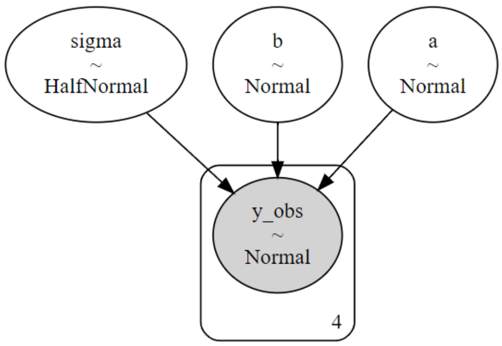

Figure 6.26 Nonhierarchical Bayesian approach scheme

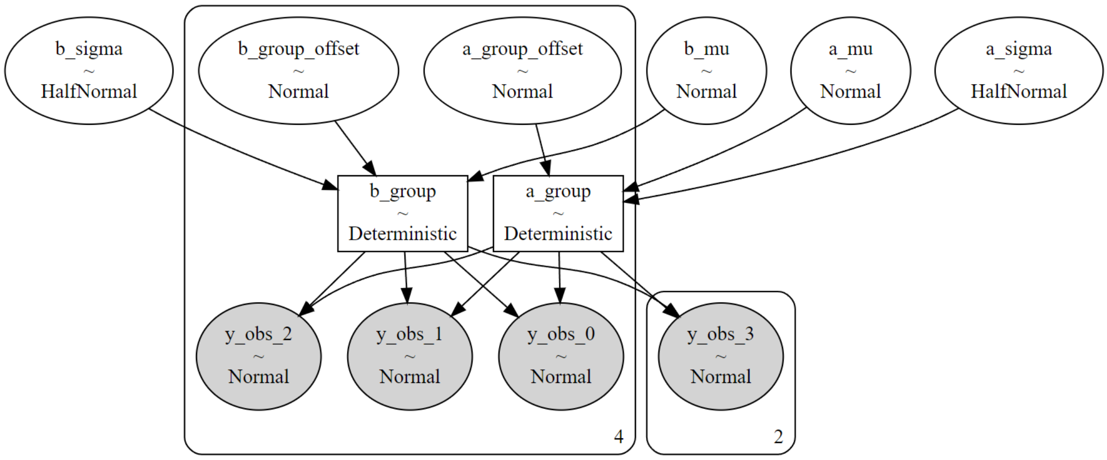

Figure 6.27 Hierarchical Bayesian approach scheme

(2) Bayesian Estimation Results

Figure 6.28 (a) is the distribution of parameter *a* estimated from the nonhierarchical Bayesian approach. Figure 6.28 (b) is the distribution of parameter *b* estimated from the nonhierarchical Bayesian approach. Figure 6.28 (c) is the distribution of parameter *a* estimated from the hierarchical Bayesian approach. Figure 6.28 (d) is the distribution of parameter *b* estimated from the hierarchical Bayesian approach. The analysis utilizing nonhierarchical and hierarchical approaches yields different results, which will be further examined in Figure 6.29 and Figure 6.30.

Figure 6.29 (a) shows the parameter *a* under the condition of σ_c = 100 kPa D_r = 40%. The figure presents the results of the conventional frequentist approach, nonhierarchical Bayesian approach, hierarchical Bayesian approach, and prior distribution. Figure 6.29 (a) shows that there are minimal differences between nonhierarchical Bayesian approach, hierarchical Bayesian approach, and conventional frequentist approach. However, the prior distribution assigned to parameter *a* is slightly distant. In Figure 6.29 (b) for the condition with σ_c 50 kPa and D_r 40%, the distribution from nonhierarchical Bayesian approach gradually converges towards the prior distribution, while that of hierarchical approach also shows a little movement towards the prior distribution in comparison to that from the conventional frequentist approach. In Figure 6.29 (c) for condition σ_c 100 kPa and D_r 70%, the distribution from nonhierarchical approach is more similar to prior distribution. In addition, the probability distribution reveals that the parameter *a* value is becoming more dispersed, leading to increased variability in this value. Lastly in Figure 6.29 (d) for condition with σ_c 50 kPa and D_r 70%, it is observed that there are limitations of the conventional frequentist approach, parameter a obtained from the conventional frequentist approach deviate significantly due to the limited amount of data. On the other hand, both the nonhierarchical Bayesian and hierarchical Bayesian approaches attempt to align with the prior distribution, with the hierarchical Bayesian approach considering the overall nature of the data.

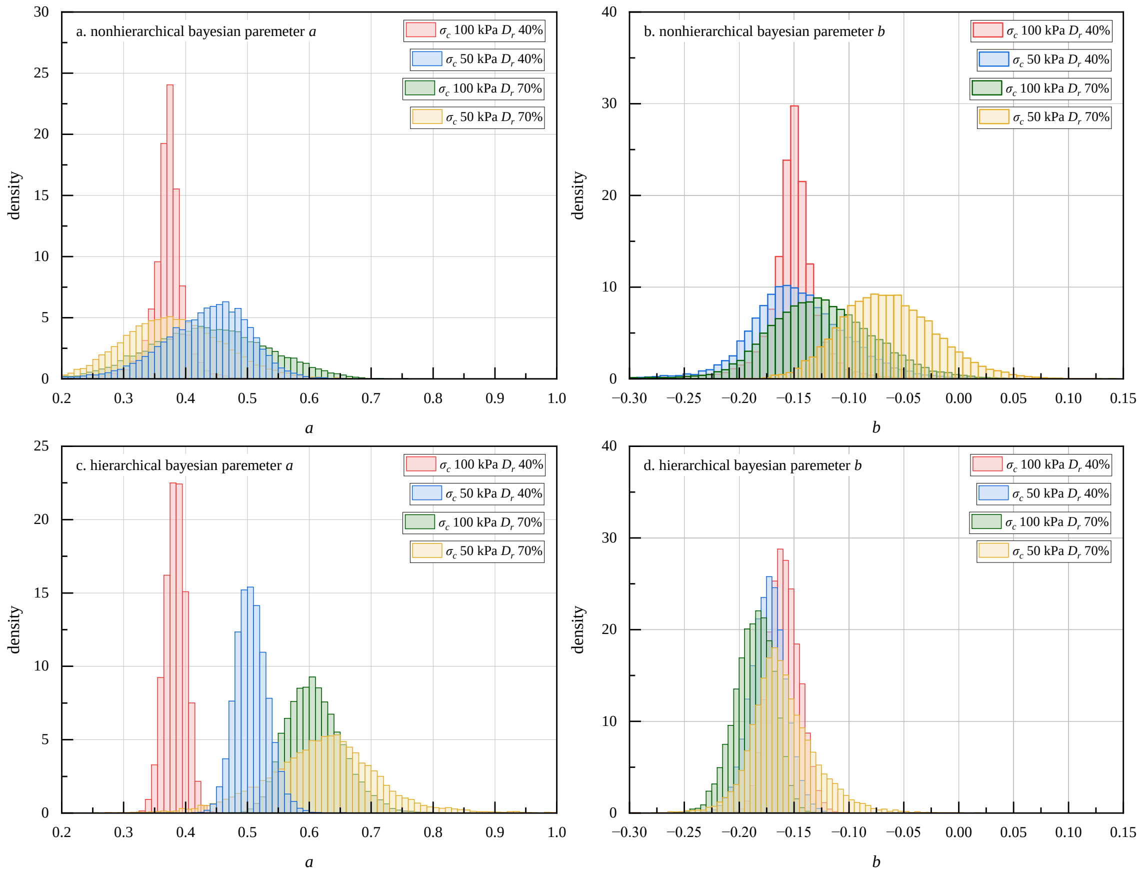

Figure 6.28 Parameters a and b distribution

In order to discuss the distribution of parameter b, Figure 6.30 (a) shows the results obtained from the nonhierarchical Bayesian approach, hierarchical Bayesian approach, and conventional frequentist approach. It can be seen that the results yield nearly identical results. In Figure 6.30 (b), the distributions from the nonhierarchical and hierarchical Bayesian approach deviate significantly from the provided prior distribution. Upon closer examination of Figure 6.30 (c), we find a similar phenomenon occurring where nonhierarchical Bayesian and hierarchical Bayesian approaches progressively diverge from the prior distribution. In Figure 6.30 (d), the distribution from nonhierarchical Bayesian and hierarchical Bayesian approaches diverge from the prior distribution, while the estimated value from conventional frequentist approach is already beyond the target range due to insufficient data. The Bayesian approach aims to approach the actual value, meaning that the prior distribution for parameter *b* is not suitable for the given conditions. The current test result is used to calculate the distribution of parameter *b* using MCMC. In this process, the Bayesian approach causes the distribution of parameter *b* to deviate from the prior distribution and align with the observed data.

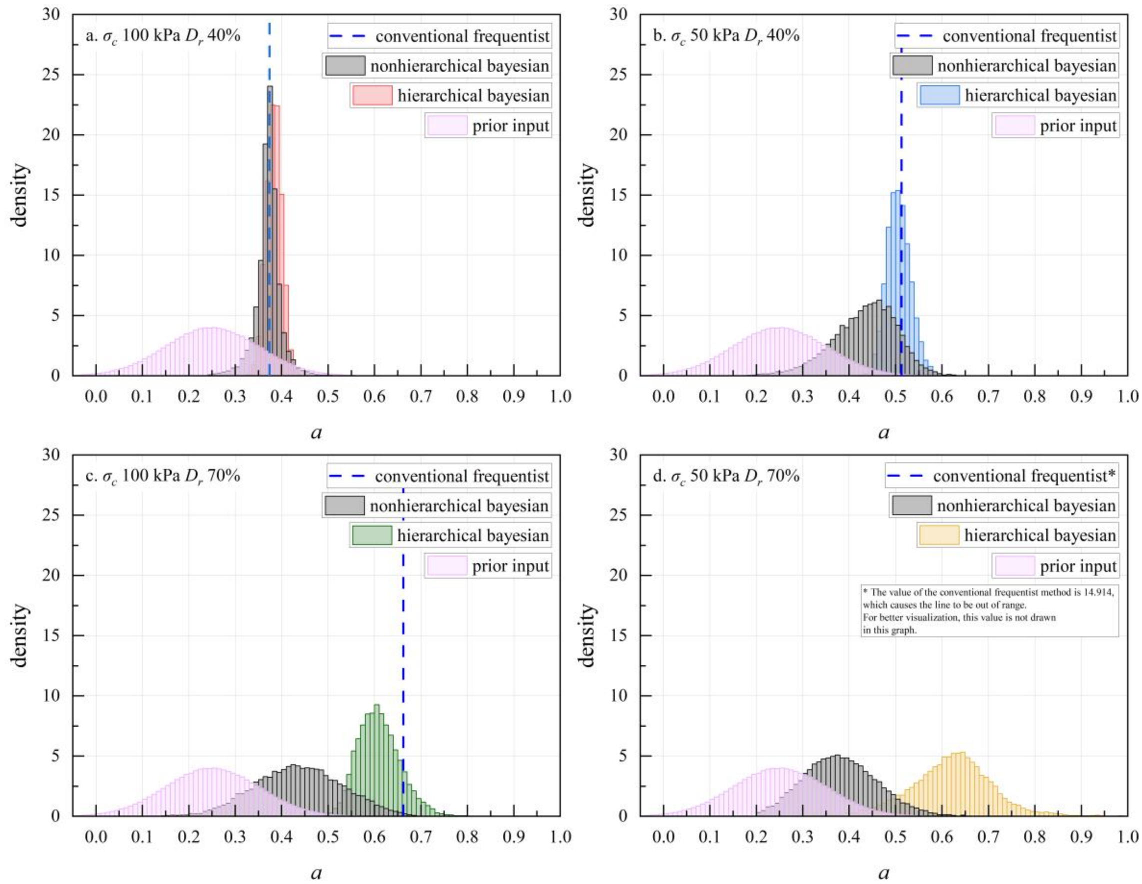

Figure 6.29 Comparison of parameter *a* for hierarchical and nonhierarchical Bayesian approach

Referring to Figure 6.29 and Figure 6.30, multiple advantages of employing the Bayesian approach, especially the hierarchical Bayesian approach can be observed. One advantage is possible to gain a more comprehensive understanding of estimated parameters by using distribution curves. Hierarchical Bayesian approach allows us to see the full extent of the distribution for each parameter. In contrast, conventional frequentist approach only provides a single parameter value, which does not provide insight into the overall distribution of the parameters as in the hierarchical Bayesian approach. In this hierarchical Bayesian approach, we can input prior distribution or starting parameter estimates as a point of reference, which can be derived from expert opinion or experience. Prior distribution can enhance the manageability of parameter values in the future, as we possess an intuitive understanding of the expected parameter values. The hierarchical Bayesian approach is handy when working with limited data, as demonstrated by Figure 6.29 (d) and Figure 6.30 (d) compared to results from other groups, the hierarchical Bayesian approach could be more accurate. Additionally, when comparing nonhierarchical and hierarchical approaches, the hierarchical Bayesian approach considers prior information, observed group data, and the entire dataset, making it a more comprehensive approach.

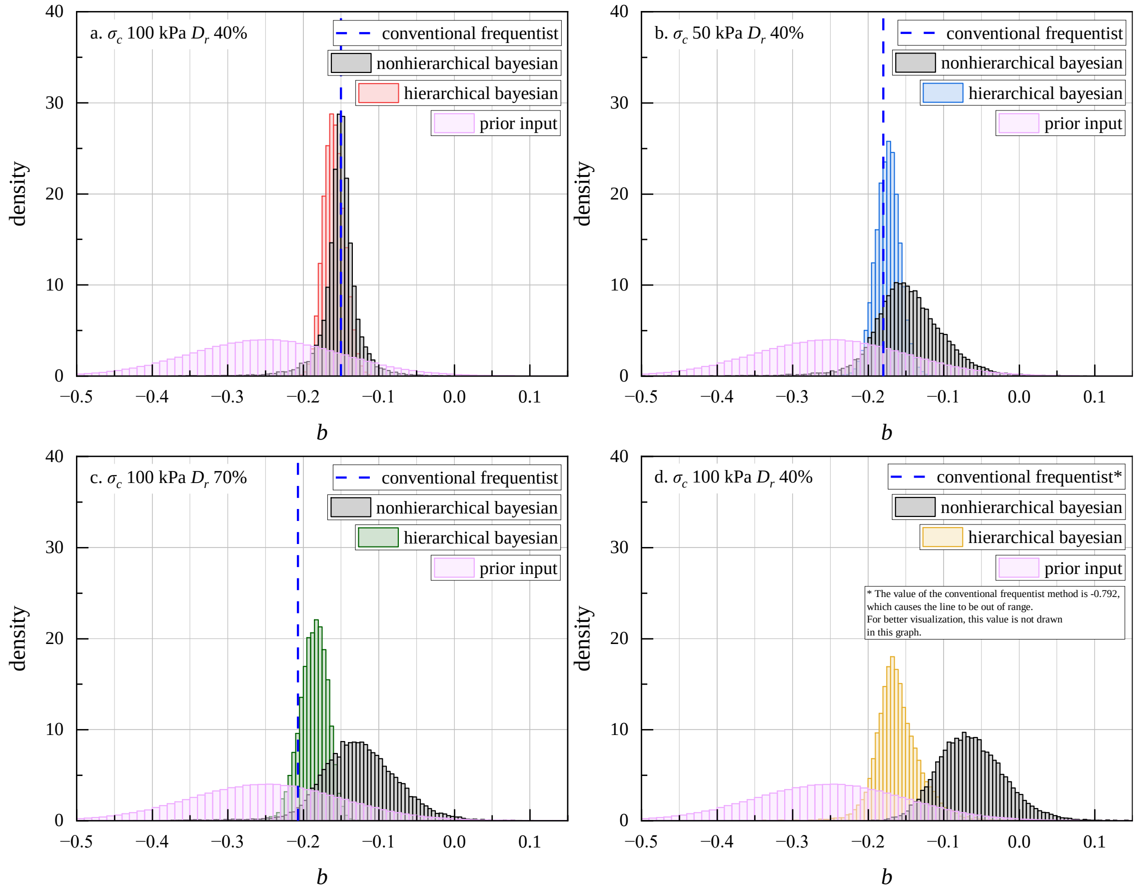

Figure 6.30 Comparison of parameter *b* for hierarchical and nonhierarchical Bayesian approach

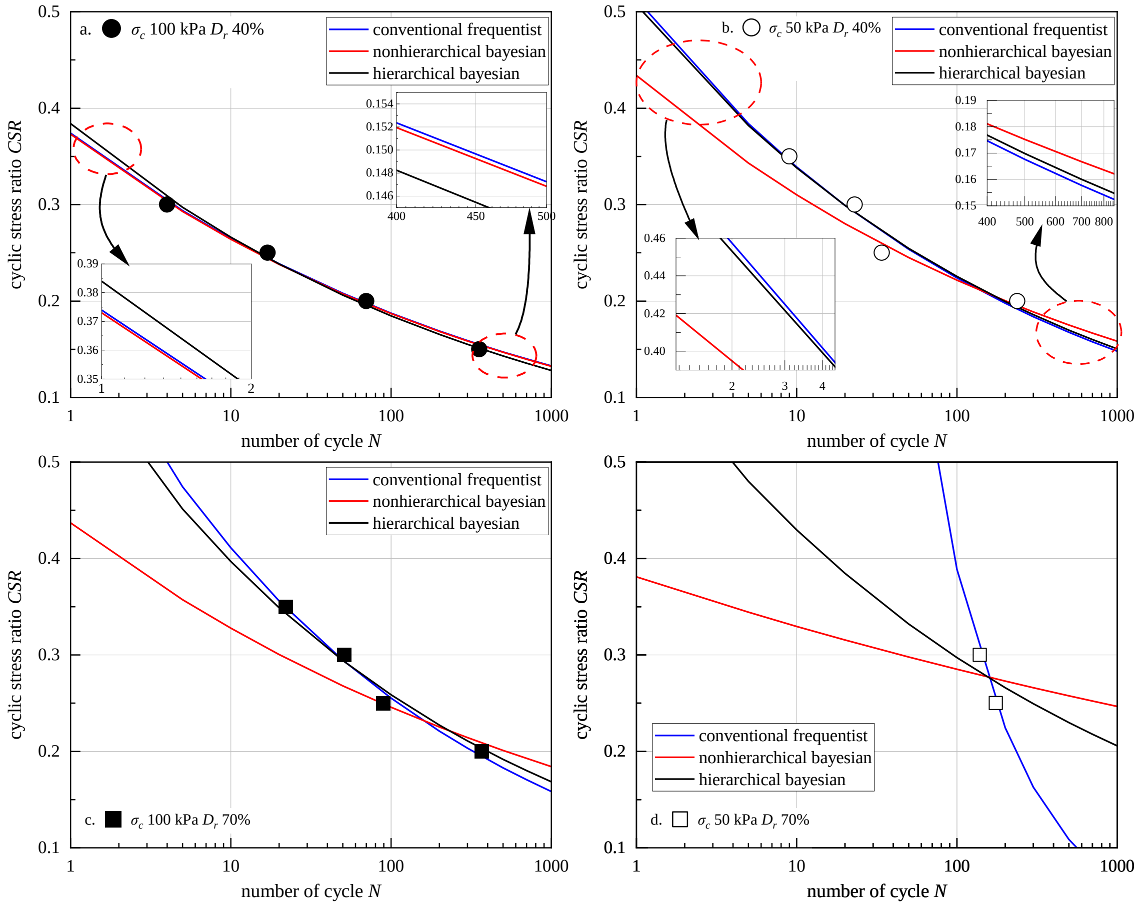

Figure 6.31 Comparison regression line for each approach

Figure 6.31 shows a regression line for conventional frequentist approach, nonhierarchical Bayesian approach, and hierarchical Bayesian approach. The regression lines for the three models are closely aligned. In addition, given the situations depicted in Figure 6.31 (a), (b), and (c), the nonhierarchical Bayesian approach diverges from the data due to the model focuses exclusively on a single group and considers only the provided prior information without considering the complete dataset. In Figure 6.31 (d), the estimated value from conventional frequentist approach exhibits significant deviation from normalcy due to insufficient data in that particular group. On the other hand, both nonhierarchical Bayesian and hierarchical Bayesian approaches demonstrate superior outcomes, with hierarchical Bayesian approach showing favorable results.

Figure 6.32 and Figure 6.33 demonstrate the distinction between nonhierarchical Bayesian and nonhierarchical methods. The gray area in Figure 6.32, which shows the nonhierarchical Bayesian results, is the 97% highest density interval (HDI), which shows a possible place where the predicted data could be. Figure 6.33, which displays the hierarchical Bayesian results, also shows the 97% HDI as a gray zone. We can observe that the hierarchical Bayesian approach in Figure 6.33 reduces the HDI zone, while the nonhierarchical Bayesian approach in Figure 6.32 has a larger size. The hierarchical Bayesian approach, with a reduced HDI zone, suggests that the model improves data prediction accuracy by reducing uncertainty. Lastly, in Figure 6.34 a regression line is plotted based on the results of hierarchical Bayesian approach, allowing us to observe the relationship between the four data groups.

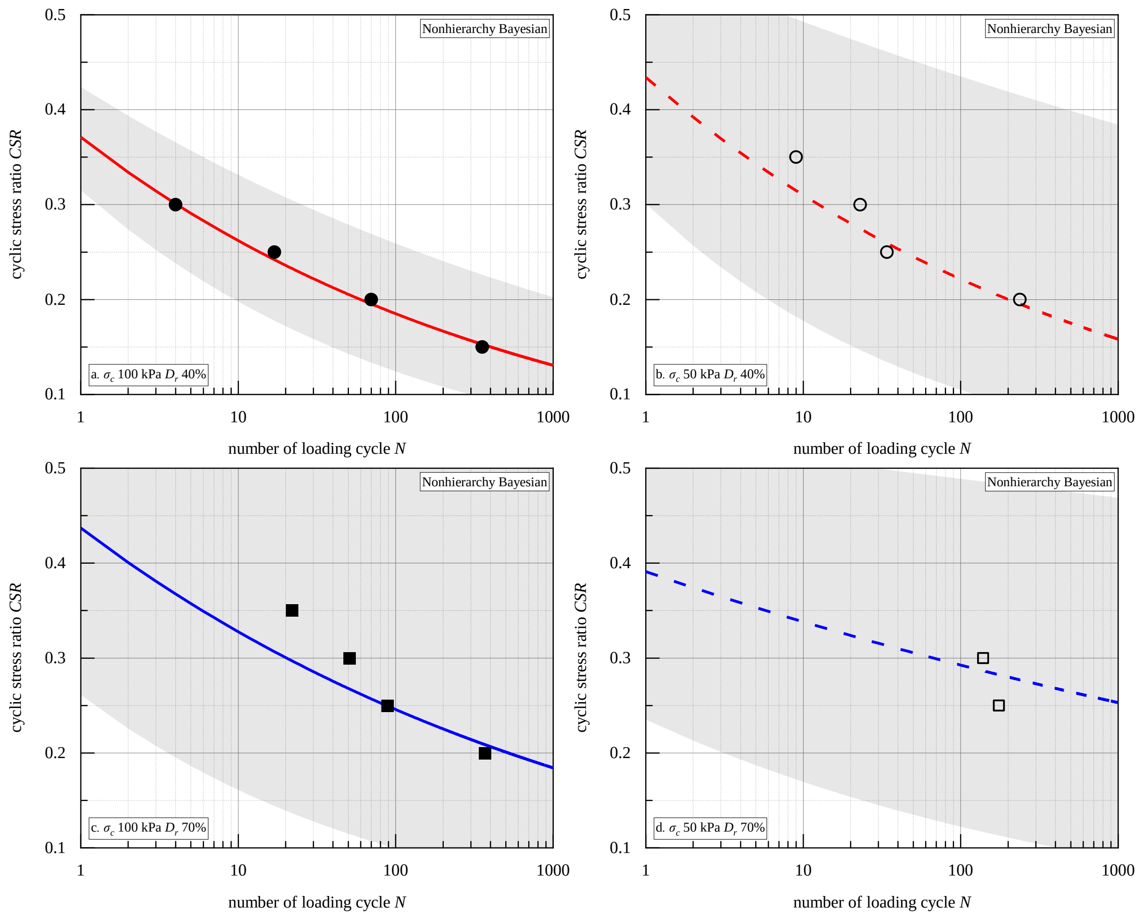

Figure 6.32 Nonhierarchical Bayesian regression model.

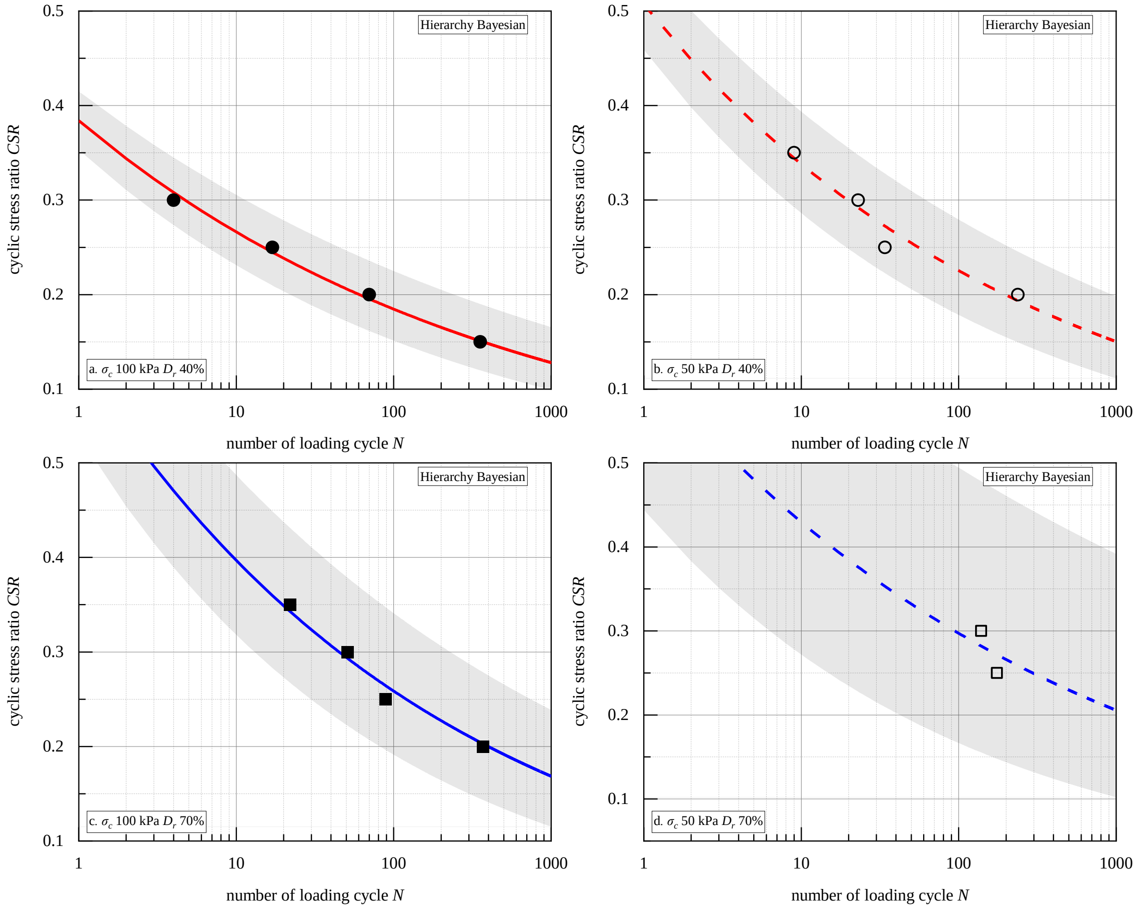

Figure 6.33 Hierarchical Bayesian regression model.

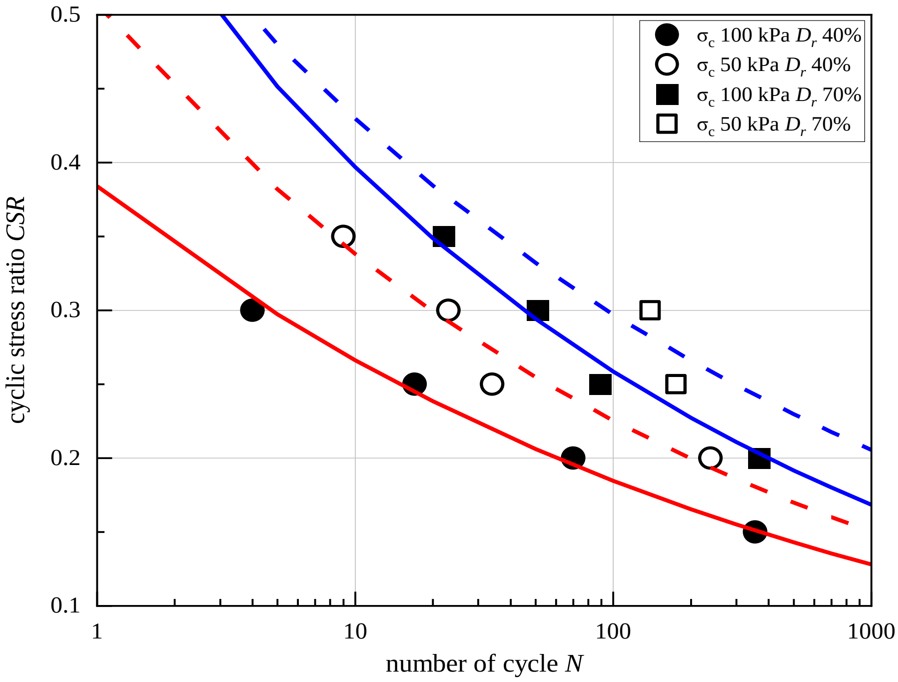

Figure 6.34 Regression line based on hierarchical Bayesian approach

6.3.6 Liquefaction Strength Behavior

Based on the regression line presented in Figure 6.34, liquefaction strength, the *CRR* value at the 20th cycle is shown in Figure 6.35. Figure 6.36 shows the relationship between the liquefaction strength of the pumice with relative density and confining pressure. Figure 6.36 demonstrates that an increase in relative density leads to a corresponding rise in liquefaction strength can be seen from CRR_{20} increases from 0.300 to 0.384 for confining pressure 50 kPa and CRR_{20} increases from 0.238 to 0.349 for confining pressure 100 kPa. This observation aligns with previous studies on the influence of relative density on the sand in general (M. Asadi et al., 2021; M. B. Asadi et al., 2022; Hyodo et al., 2016; Hyodo, Yasufuku, et al., 1994; Orense RP & Pender MJ, 2013). The increase in liquefaction strength results from an increase in relative density caused by enhanced bonding between the pumice, and this can be observed through a decrease in the void ratio, indicating a reduction in space within the specimen. As a result, the pore water pressure buildup is slowing down, which is the underlying cause of liquefaction is slowed down. In addition, higher density enhances the interlocking of particles, decreasing the compressibility of the sample. The decline in compressibility can be detected by the decrease in fine particles when the relative density is 70%. At the same time, an increase in fine particles is noted at a relative density of 40%.

According to specific literature on liquefaction resistance, increasing the quantity of fine content will enhance the resistance to liquefaction (M. S. Asadi et al., 2019; Goudarzy et al., 2022; Huang et al., 2023). However, despite more fine particles at a relative density of 40%, the liquefaction resistance is still lower compared to a relative density of 70%. Multiple factors contribute to this phenomenon. Initially, the fine material produced during the liquefaction process was not there. Therefore, the impact of fine particles on increasing liquefaction strength has not been observed. Furthermore, the impact of crushability on this particular sample remains inconspicuous as the applied confining pressure and axial stress have not surpassed the yield stress of the pumice.

Typically, the effect of confining pressure on liquefaction strength in sandy materials is not substantial (Hyodo, Tanimizu, et al., 1994). Therefore, a standard confining pressure of 100 kPa is commonly used, pumice exhibits liquefaction strength dependency on confining pressure. Figure 6.36 shows the decrease in confining pressure enhances the liquefaction strength can be seen in CRR_{20} reduces from 0.300 to 0.238 for a relative density 40% and CRR_{20} reduces from 0.384 to 0.349 for a relative density 70%. The test results do not show a noticeable influence of confining pressure on crushable behavior, as demonstrated by the changes in particle size shown in Figure 6.36. However, a more comprehensive explanation for this behavior can be found in the analysis of the test sand samples (National Academies of Science, 2021; Yoshimine & Ishihara, 1998), which indicates that reducing confining pressure can enhance the strength of liquefaction, and this pertains to the steady state line in the undrained triaxial test and the consolidation line. The investigation revealed that the slope of the steady state line is generally steeper than the consolidation line.

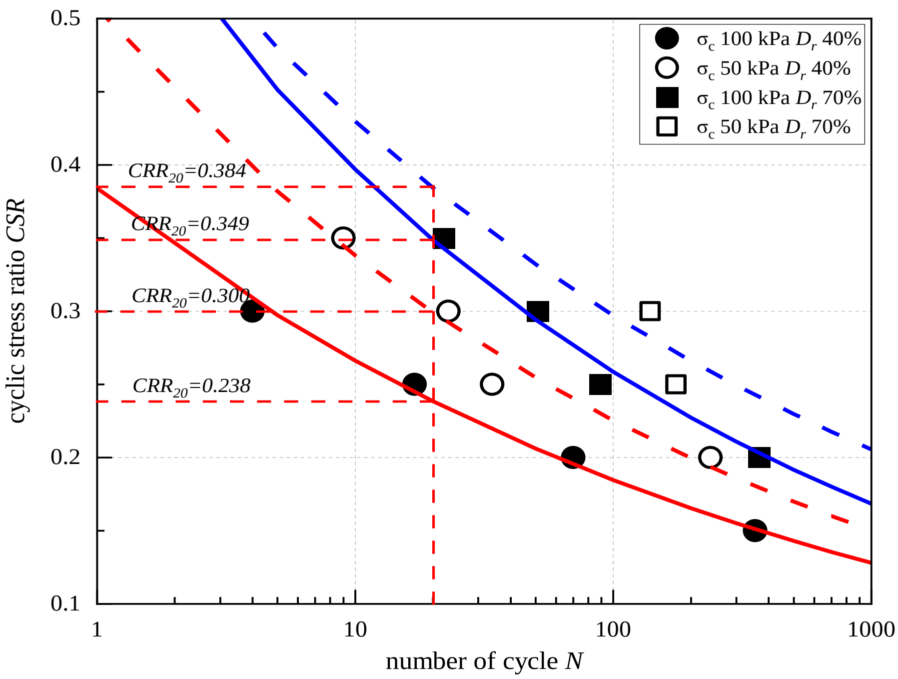

Figure 6.35 Cyclic resistance ratio at 20 cycles

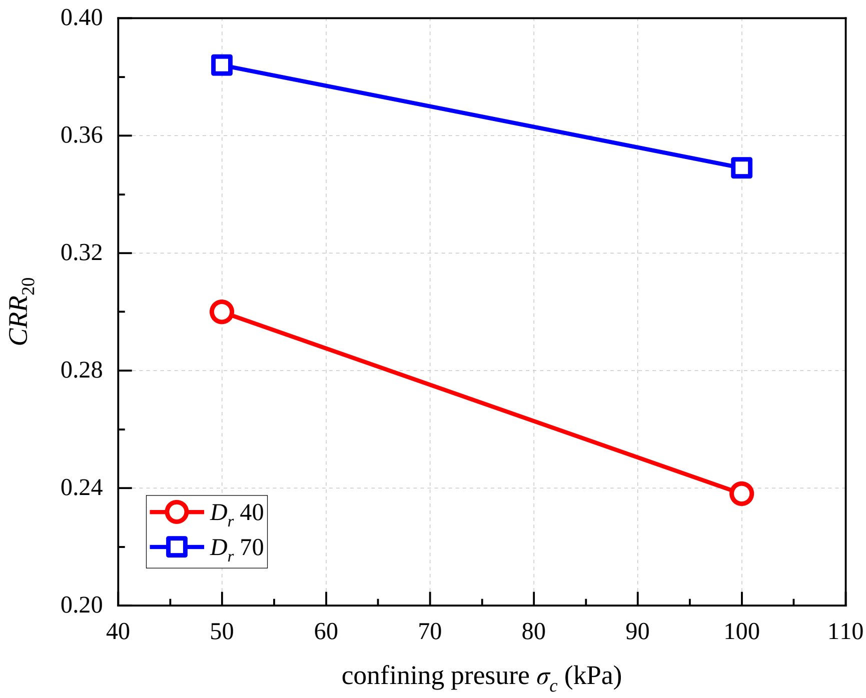

Figure 6.36 Effect of confining pressure at different relative densities on cyclic resistance ratio

6.4 Summary

This chapter examines the mechanical behavior of the pumice under static and cyclic undrained triaxial tests to assess the liquefaction susceptibility. The effects of changes in relative density and confining pressure on the pumice are also investigated. Additionally, the hierarchical Bayesian approach is introduced to evaluate the liquefaction curve for the purpose of comprehensive statistical data interpretation as well as overcoming the limitation of data number and testing error.

1. Static triaxial compression test under undrained conditions reveals that pumice exhibits strain-hardening behavior with a cohesion value of 25.9 kN/m^2 and a friction angle of 51.1 °.
2. Based on the test result of the static triaxial compression test under the drained condition, pumice exhibits strain-softening behavior. This behavior results from the particle crushability of pumice in the drained condition, which reduces shear strength. The cohesion value for the drained condition is 12.0 kN/m^2, and the friction angle is 35.9 °.
3. The cyclic undrained triaxial compression test demonstrates that liquefaction resistance of pumice increases as the relative density increases can be seen from CRR_{20} increase from 0.300 to 0.384 for confining pressure 50 kPa and CRR_{20} increase from 0.238 to 0.349 for confining pressure 100 kPa, that behavior is similar to general quartz sand such as Toyoura sand. On the other hand, the liquefaction resistance reduces when the confining pressure increases can be seen in CRR_{20} reduces from 0.300 to 0.238 for a relative density 40% and CRR_{20} reduces from 0.384 to 0.349 for a relative density 70%.
4. The hierarchical Bayesian approach, with a smaller HDI zone compared to nonhierarchical Bayesian approach, suggests that the model improves data prediction accuracy by reducing uncertainty. The hierarchical Bayesian approach also yields favorable estimation even for a very small dataset and provides a comprehensive evaluation of liquefaction strength from the statistical point of view.

References

Asadi, M. B., Orense, R. P., Asadi, M. S., & Pender, M. J. (2022). A unified approach to link small-strain shear modulus and liquefaction resistance of pumiceous sand. Soils and Foundations, 62(1). https://doi.org/10.1016/j.sandf.2021.101098

Asadi, M., Orense, R. P., Asadi, M., & Pender, M. J. (2021, November). Laboratory-based method to quantify pumice contents of volcanic deposits. 6th Int. Conf. Geotechnical and Geophysical Site Characterization.

Asadi, M. S., Orense, R. P., Asadi, M. B., & Pender, M. J. (2019). Maximum dry density test to quantify pumice content in natural soils. Soils and Foundations, 59(2), 532–543. https://doi.org/10.1016/j.sandf.2019.01.002

Basoka, I. W. A., Kasama, K., Furukawa, Z., Yasufuku, N., & Rifa'i, A. (2024, May). Pumice sand behavior on undrained cyclic loading. 8th International Conference on Earthquake Geotechnical Engineering., Osaka, Japan.

Chiaro, G., Kiyota, T., Umar, M., & Cappellaro, C. (2022). Earthquake-Induced Flow-Type Slope Failure in Weathered Volcanic Deposits—A Case Study: The 16 April 2016 Takanodai Landslide, Japan. Geosciences, 12(11), 1–22. https://doi.org/10.3390/geosciences12110394

Crosta, G. B., Imposimato, S., Roddeman, D., Chiesa, S., & Moia, F. (2005). Small fast-moving flow-like landslides in volcanic deposits: The 2001 Las Colinas Landslide (El Salvador). Engineering Geology, 79(3–4), 185–214. https://doi.org/10.1016/j.enggeo.2005.01.014

Fangwei, Y. (2018). Particle Breakage and the Undrained Shear Behavior of Sands. International Journal of Geomechanics, 18(7), 04018079. https://doi.org/10.1061/(ASCE)GM.1943-5622.0001203

Faris, F., & Fawu, W. (2014). Investigation of the initiation mechanism of an earthquake-induced landslide during rainfall: a case study of the Tandikat landslide, West Sumatra, Indonesia. Geoenvironmental Disasters, 1(4).

Goudarzy, M., Sarkar, D., Lieske, W., & Wichtmann, T. (2022). Influence of plastic fines content on the liquefaction susceptibility of sands: monotonic loading. Acta Geotechnica, 17(5), 1719–1737. https://doi.org/10.1007/s11440-021-01283-w

Gupta, A. K. (2016). Effects of particle size and confining pressure on breakage factor of rockfill materials using medium triaxial test. Journal of Rock Mechanics and Geotechnical Engineering, 8(3), 378–388. https://doi.org/https://doi.org/10.1016/j.jrmge.2015.12.005

Hosobuchi, M. N., Chigira, M., Lim, C., & Komoo, I. (2021). Geological history controlling the debris avalanches of pyroclastic fall deposits induced by the 2009 Padang earthquake, Indonesia: The sequential influences of pumice fall, weathering, and slope undercut. Engineering Geology, 287. https://doi.org/10.1016/j.enggeo.2021.106104

Huang, C., Xu, S., Shen, Z., Zhang, L., Wang, L., & Liu, C. (2023). Effects of non-plastic fines on liquefaction properties of saturated silt using discrete element modeling. Engineering Geology, 317, 107091. https://doi.org/https://doi.org/10.1016/j.enggeo.2023.107091

Hyodo, M., Tanimizu, H., Yasufuku, N., & Murata, H. (1994). Undrained cyclic and monotonic triaxial behaviour of saturated loose sand. Soils and Foundations, 34(1), 19–32.

Hyodo, M., Wu, Y., Aramaki, N., & Nakata, Y. (2016). Undrained monotonic and cyclic shear response and particle crushing of silica sand at low and high pressures. Canadian Geotechnical Journal, 54(2), 207–218. https://doi.org/10.1139/cgj-2016-0212

Hyodo, M., Yasufuku, N., Murata, M., Hyde, A. F. L., & Okobayashi, T. (1994). Undrained cyclic shear strength and deformation of crushable soil. International Symposium on Pre-Failure Deformation Characteristics of Geomaterials, 87–94.

Ishihara, K. (1993). Liquefaction and flow failure during earthquakes. Géotechnique, 43(3), 351–451. https://doi.org/10.1680/geot.1993.43.3.351

Ishihara, K., Tatsuoka, F., & Yasuda, S. (1975). Undrained Deformation and Liquefaction of Sand Under Cyclic Stresses. Soils and Foundations, 15(1), 29–44. https://doi.org/https://doi.org/10.3208/sandf1972.15.29

Kang, X., Xia, Z., Chen, R., Ge, L., & Liu, X. (2019). The critical state and steady state of sand: A literature review. Marine Georesources & Geotechnology, 37, 1–14. https://doi.org/10.1080/1064119X.2018.1534294

Kasama, K., Furukawa, Z., & Yasufuku, N. (2021). Cyclic shear property and seismic runout analysis for pumice fall deposit. Soil Dynamics and Earthquake Engineering, 143, 1–11. https://doi.org/10.1016/j.soildyn.2021.106588

National Academies of Science, E. and M. (2021). State of the Art and Practice in the Assessment of Earthquake-Induced Soil Liquefaction and Its Consequences. The National Academies Press. https://doi.org/10.17226/23474

Orense RP, & Pender MJ. (2013). Liquefaction characteristics of crushable pumice sand. Proceedings of the 18th International Conference on Soil Mechanics and Geotechnical Engineering, 1559–1562.

Rahman, Md. M., & Sitharam, T. G. (2020). Cyclic liquefaction screening of sand with non-plastic fines: Critical state approach. Geoscience Frontiers, 11(2), 429–438. https://doi.org/https://doi.org/10.1016/j.gsf.2018.09.009

Seed, H. B., & Idriss, I. M. (1971). Simplified Procedure for Evaluating Soil Liquefaction Potential. Journal of the Soil Mechanics and Foundations Division, 97(9), 1249–1273. https://doi.org/10.1061/JSFEAQ.0001662

Siebe, C., Salinas, S., Arana-Salinas, L., Macías, J. L., Gardner, J., & Bonasia, R. (2017). The ~23,500 y 14C BP White Pumice Plinian eruption and associated debris avalanche and Tochimilco lava flow of Popocatépetl volcano, México. Journal of Volcanology and Geothermal Research, 333–334, 66–95. https://doi.org/10.1016/j.jvolgeores.2017.01.011

Ueda, K. (2022). Hierarchical Bayesian approach to estimating variability of liquefaction resistance of sandy soils considering individual differences in laboratory tests. Journal of Geotechnical and Geoenvironmental Engineering, 148(2). https://doi.org/10.1061 /(asce)gt.1943-5606.0002749

Umar, M., Chiaro, G., Kiyota, T., & Miyamoto, H. (2018). Monotonic and Cyclic Undrained Behavior of Kumamoto-Aso Pumice by Triaxial And Torsional Shear Test. 16th European Conference on Earthquake Engineering.

Umar, M., Kiyota, T., Chiaro, G., & Antoine, D. (2019). Undrained Monotonic Behavior Of Sand In Large Strain Torsional Shear Apparatus (pp. 52: 1-9).

Yoshimine, M., & Ishihara, K. (1998). Flow Potential of Sand During Liquefaction. *Soils and Foundations*, *38*(3), 189–198. https://doi.org/https://doi.org/10.3208/sandf.38.3_189

CHAPTER VII
CONCLUSIONS AND FUTURE WORKS

This dissertation is focused on investigating the behavior of pumice under static and dynamic loads to acquire a deeper understanding of its role in geotechnical failures. In order to accomplish this, there are multiple goals in this study:

1. To identify the geological, chemical, and microstructural characteristics of pumice.
2. To explore the relationship between pore characteristics and the mechanical behavior of pumice particles.
3. To compare the particle characteristics and soil matrix characteristics of pumice using a one-dimensional consolidation test.
4. To analyze the liquefaction resistance of pumice under various confining pressures and density variations
5. To evaluate the effectiveness of the Bayesian approach in explaining pumice behavior

In order to address those objectives, various investigations were conducted to examine pumice, starting from geological, chemical, and microstructural characteristics, which were achieved using XRF, EDS, XRD, and SEM testing. Subsequently, a single-particle strength test and a one-dimensional consolidation test using a constant rate of strain loading test were used to assess the mechanical properties of a single pumice particle and its interaction with the pumice soil matrix. These tests involved subjecting the pumice to a constant rate of strain loading in order to determine its crushability behavior. Afterward, static and cyclic undrained triaxial tests were conducted to ascertain the behavior of pumice under both static and dynamic conditions. Lastly, the Bayesian approach was utilized to assess the laboratory test outcomes.

7.1 Conclusions

Based on the objectives of this dissertation and the conducted tests, we have reached the following conclusions:

1. This study examines pumice, a poorly graded sand (*SP*) from the Ito pyroclastic

flow under the Osumi pumice fall, from the Late Pleistocene period. The pumice possesses pores that may result in the formation of crushable particles and particle size distribution shows pumice has the potential to liquefy. The chemical composition of pumice consists of silica (21.7%), aluminum (7.40%), oxygen (61.13%), and the rest is other chemical components. The mineral component consists of quartz (66.70%), and cristobalite-alpha (33.30%), the minerals that can potentially have crushable behavior.

2. It was found that the strength of the pumice decreases when the size of the particle is increased. In the last test using 135 samples, we can obtain most of the shape parameter (α) parameter result < 1, which means the sample is "decreasing failure rate," or, in other words, single-particle strength is decreased with increasing particle size. The explication of the scale parameter (β) parameter describes how distributed the data is; the higher the scale parameter value, the more spread the shape of the Weibull curve. The relationship between particle shape (aspect ratio and roundness coefficient) and particle strength does not correlate significantly. The aspect ratio and roundness coefficient exhibit a positive correlation. An increase in aspect ratio with an increasing roundness coefficient is similar to that of typical crushable soils. There is a reduction in the pore area in the pumice particles, while the number of pores increases due to the particle crushing after the pumice particle is tested by a single-particle strength test.
3. The findings indicate that the yield stress of pumice is laid between Toyoura sand and clay (clay 0.05 MPa, pumice 0.724 MPa – 1.048 MPa, and sand 10 MPa), where the void ratio value of pumice is closer to the void ratio of clay. This study also discovered that pumice has greater crushability if we compare it to other materials based on yield stress pumice around 0.724 MPa – 1.048 MPa with a relative density of 40% to 80%. For the compression index of pumice, we obtained 0.569 to 0.936 with a relative density of 40% to 80%. The results show a significant correlation between the single-particle strength and the yield stress obtained from the one-dimensional consolidation test with the constant rate of strain loading influenced by the relative density value, with higher relative density values indicating closer results between the tests.
4. From this study, we can find the important behavior of pumice under static triaxial

compression test under undrained conditions, revealing that pumice exhibits strain-hardening behavior with a cohesion value of 25.9 kN/m^2 and a friction angle of 51.1 °. On the other hand, in a static triaxial compression test under drained conditions, pumice exhibits strain-softening behavior. This behavior results from the particle crushability of pumice in the drained condition, which reduces shear strength. The cohesion value for the drained condition is 12.0 kN/m^2, and the friction angle is 35.9 °. The cyclic undrained triaxial compression test discovered that the liquefaction resistance of pumice increases as the relative density increases, and this can be seen from CRR_{20} increase from 0.300 to 0.384 for a confining pressure of 50 kPa and CRR_{20} increase from 0.238 to 0.349 for a confining pressure of 100 kPa. That behavior is similar to general quartz sand, such as Toyoura sand. On the other hand, the liquefaction resistance reduces when the confining pressure increases, as can be seen in CRR_{20}, which reduces from 0.300 to 0.238 for a relative density of 40%, and CRR_{20} reduces from 0.384 to 0.349 for a relative density of 70%.

5. The significance of the study lies in applying the hierarchical Bayesian approach. We can observe and describe the strength behavior based on linear fitting using the hierarchical Bayesian approach, which yields excellent results when the data set is small (15 data). In contrast, the prediction error is obtained using the conventional frequentist approach on a small sample size, and this situation is further confirmed when a large data set (135 data) is used. The hierarchical Bayesian approach consistently outperforms the frequentist approach in terms of prediction accuracy for the linear fitting to predict particle strength based on diameter. The Weibull distribution parameters yield slightly similar outcomes to those obtained through the linear fitting approach. The conventional frequentist and Bayesian approaches yield unsatisfactory results when the sample size is small, precisely 15. However, when the sample size increases to 45, the Bayesian approach is a more balanced point between the conventional frequentist and Bayesian approach. Finally, when the sample size reaches 90, conventional frequentist and Bayesian approaches exhibit a similar trend. It is evident that in specific situations, it is necessary to use a minimum number of samples to obtain accurate values. In addition, applying the hierarchical Bayesian approach has demonstrated its effectiveness in evaluating liquefaction in pumice.

This approach provides a more comprehensive understanding, mainly when dealing with small sample sizes where conventional frequentist approaches fail to describe each parameter's behavior accurately. The hierarchical Bayesian approach also has a smaller highest density interval (HDI) zone compared to nonhierarchical Bayesian approach, showing that the hierarchical Bayesian approach improves data prediction accuracy by reducing uncertainty. In addition, employing a hierarchical Bayesian approach alongside Markov Chain Monte Carlo (MCMC) sampling enhances the robustness of the sample, as evidenced by the heightened density observed in the histogram of each dataset.

7.2 Future Works

From the previously mentioned outcomes, it is evident that this study successfully tackles the objectives formulated by the background and research problems identified in the previous chapter. However, this study has certain limitations, and further studies are needed to explore, listed as follows:

1. To accurately analyze the fundamental characteristics of pumice, it is advisable to compare them with undisturbed samples collected directly from the field, which allows for a comprehensive comparison of the behavior between disturbed and undisturbed samples.
2. When doing the single-particle strength test, it is crucial to carefully observe and record any crack formation in the individual pumice particle. Additional size variations must be incorporated to enhance comprehension of individual particle robustness.
3. In one-dimensional consolidation testing, it is important to observe any changes in distribution that occur after testing, which can be done by terminating the test after the sample surpasses its yield stress. By doing so, we can gain insights into the alterations in size distribution.
4. When conducting triaxial testing, whether static or cyclic, it is important to choose the confining pressure carefully. The confining pressure should be selected in between its yield stress, and this allows for better observation of changes in particle size distribution. The irregular cyclic loading can offer insight into the actual earthquake that took place.

5. The Bayesian approach requires a more thorough consideration of prior selection and model changes.